UNIVERSITY OF CALIFORNIA SAN DIEGO

Thermal Transport and Transformation in Micro-Structured Materials

A dissertation submitted in partial satisfaction of the requirements for the degree

Doctor of Philosophy

in

Engineering Sciences (Mechanical Engineering)

by

Shuang Cui

Committee in Charge:

Professor Renkun Chen, Chair
Professor Shengqiang Cai
Professor Ping Liu
Professor Jeffrey Dennis Rinehart
Professor George Robert Tynan

2018

The Dissertation of Shuang Cui is approved, and it is acceptable in quality and form for publication on microfilm and electronically:

_____

_____

_____

_____

_____

Chair

University of California San Diego

2018

DEDICATION

Dedicated to my sweet and loving parents

who encourage and support me to go on every adventure

especially this one

TABLE OF CONTENTS

LIST OF FIGURES

LIST OF TABLES

ACKNOWLEDGEMENTS

As I approach this pinnacle of academic achievement, I would like to acknowledge and thank those who have helped me reach this goal. First and foremost, I would like to express my sincere appreciation and gratitude to my advisor, Prof. Renkun Chen, for his great support and guidance. His innovative thoughts and thorough understanding to complex scientific studies always inspire me. I would like to thank him for his invaluable advice through my Ph.D. study on scientific research and career path, as well as how to become a better scientist/researcher with curiosity, enthusiasm and self-motivation.

I appreciate my committee members. I thank Prof. Shengqiang Cai for his great collaboration on tough hydrogels for building cooling and generously sharing the lab space with me. I thank Prof. George R. Tynan for his insightful advice and great support on the collaboration of studying thermal properties of plasma facing materials. I also would like to thank Prof. Ping Liu for his insightful suggestions on the thermo-responsive adsorbent materials as well as my future career path. I thank Prof. Jeffrey D. Rinehart for taking time to serve as my committee out of his busy schedule.

I also would like to thank Dr. Russ. P. Doerner (UCSD) for performing the helium plasma damage on tungsten, Prof. Engang Fu (PKU) and Dr. Yongqiang Wang (LANL) for performing the ion irradiation on tungsten, and Prof. Feng Ren (Wuhan Univ.) for bringing me the tungsten thin film samples. Larry Grissom, Dr. Xuekun Lu, and Ian L. Richardson are also gratefully acknowledged for their great assistance.

Additionally, I would like to thank my coworkers, Chi Hyung, Ahn, Dr. Joseph L. Barton, Wenjing Qin, especially Michael J. Simmonds for his insightful and valuable

discussion. I also appreciate the support from the group members in Thermal, Energy, Materials and Physics (TEMP) Lab, Elizabeth Rubin (Caldwell), Sahngki, Hong, Dr. Jeongmin Kim, Dr. Soonshin Kwon, Dr. Jaeyun Moon, Yang Shi, Sunmi Shin, Qingyang Wang, Dr. Matthew C. Wingert, Dr. Jianlin Zheng, and especially Patrick Charles, Dr. Edward Dechaumphai, and Jian Zeng, whom I worked with closely on 3-omega measurement and thermo-responsive adsorbents.

I also would like to greatly thank my parents and my boyfriend for their unconditional support and love always. I appreciate the accompany and friendship from my roommate, Peng Chen, for sharing both the happiness and sadness during my Ph.D. life. Special thanks are also given to Prof. Xuejiao Hu, for his encouragement of pursuing Ph.D..

Chapter 2, in part, is a reprint of the material as it appears in Journal of Nuclear Materials, 2017. Shuang Cui, Michael J. Simmonds, Wenjing Qin, Feng Ren, George R. Tynan, Russell P. Doerner, Renkun Chen. The dissertation author was the primary investigator of this paper. Also, it, in part, is in a manuscript under revision by Journal of Nuclear Materials, Shuang Cui, Russ P. Doerner, Michael J. Simmonds, Chuan Xu, Yongqiang Wang, Edward Dechaumphai, Engang Fu, George R. Tynan, Renkun Chen. The dissertation author was the primary investigator and the first author of this paper.

Chapter 3, in part, is a reprint of the material as it appears in Journal of Nuclear Materials, 2017. Shuang Cui, Michael J. Simmonds, Wenjing Qin, Feng Ren, George R. Tynan, Russell P. Doerner, Renkun Chen. The dissertation author was the primary investigator of this paper.

Chapter 4, is a reprint of the material as it appears in Applied Energy, 2016. Shuang Cui, Chihyung Ahn, David Leung, Matthew C. Wingert, Shengqiang Cai, and Renkun Chen. The dissertation author was the first author of this paper.

Chapter 5, in part, is in a manuscript in preparation, 2018. Shuang Cui, Jian Zeng, Patrick Charles, Evan Muller, and Renkun Chen. The dissertation author was the first author of this paper.

VITA

2011 Bachelor of Engineering, Wuhan University, Wuhan, China

2013 Master of Engineering, Wuhan University, Wuhan, China

2018 Doctor of Philosophy, University of California San Diego, USA

PUBLICATIONS

JOURNALS

1. **S Cui,** J Zeng, P Charles, E Muller, R Chen. "Super-absorbing Porous Thermo-responsive Hydrogel Composite Desiccants with Low Regeneration Temperature", To be submitted, 2018
2. J Zeng, **S Cui**, Y Shi, R Chen. "Temperature-responsive Janus micro-gels with high ionic strength and fast regeneration process for energy-efficient desalination". To be submitted, 2018.
3. **S Cui,** R P. Doerner, M J. Simmonds, C Xu, Y Wang, E Dechaumphai, E Fu, G R. Tynan, R Chen. "Thermal Conductivity Degradation and Recovery in Ion beam Damaged Tungsten at Different Temperature", In Revision, 2018
4. J Zeng, **S Cui**, Q Wang, R Chen. "Multi-layer Temperature-responsive Hydrogel for Forward-osmosis Desalination with High Permeable Flux and Fast Water Release", Submitted, 2018
5. E Zheng*, **S Cui***, N Kempf, Q Xing, T Chasapis, H Zhu, Z Li, J Bahk, G Snyder, Y Zhang, R Chen, Y Wu. "Inhomogeneity in Spark Plasma Sintered Bismuth Antimony Telluride Nanoplate Composite", Submitted, 2018

   * These authors contribute equally to this work.

6. B Lee, **S Cui**, X Xing, H Liu, X Yue, H Lim, R Chen, P Liu. "Dendrite Suppression Membranes for Rechargeable Zinc Batteries", Submitted, 2018.
7. **S Cui**, M J. Simmonds, W Qin, F Ren, G R. Tynan, R P. Doerner, R Chen. "Thermal Conductivity Reduction of Tungsten Plasma Facing Material due to Helium Plasma Irradiation in PISCES Using the Improved 3-Omega Method", Journal of Nuclear Materials, 486, 267-273, 2017
8. G R. Tynan, R P. Doerner, J L. Barton, R Chen, **S Cui**, Y Wang, J S. Weaver, N Mara, S Pathak. "Deuterium Retention and Thermal Conductivity in Ion-beam Displacement-Damaged Tungsten", Nuclear Materials and Energy, 12, 164-168, 2017
9. S Kwon*, J Zheng*, M C. Wingert, **S Cui**, R Chen. "Unusually High and Anisotropic Thermal Conductivity in Amorphous Silicon Nanostructures", ACS Nano, 11, 2470-2476, 2017
10. S Shin, R Kumar, J Roh, D Ko, H Kim, S Kim L Yin, S M. Schlossberg, **S Cui**, J You, S Kwon, J Zheng, J Wang, R Chen. "High-Performance Screen-Printed Thermoelectric Films on Fabrics", Scientific Report, 7, 7317, 2017
11. **S Cui**, C Ahn, D Leung, M C. Wingert, S Cai, R Chen. "Bio-inspired Effective and Regenerable Building Cooling Using Tough Hydrogels", Applied Energy, 168, 332-339, 2016
12. **S Cui**, Y Hu, Z Huang, C Ma, L Yu, X Hu. "Cooling Performance of Bio-mimic Perspiration from Temperature-Sensitive Hydrogel", International Journal of Thermal Science, 79, 276-282, 2014
13. K Liu, **S Cui**, W Kan, X Qi, C Chen, X Hu. "Giant Thermal Transport Phase Lagging in CNT Aggregates", Nanoscale and Microscale Thermophysical Engineering, 17,

236-244, 2013.

14. K Liu, M Li, **S Cui**, X Hu. “Large Thermal Transport Phase Lagging Improves Thermoelectric Efficiency”, Applied Physics A, 111, 477-481, 2013.
15. Y Hu, X Zhang, **S Cui**, W Ren, L Yu, X Hu. “Bio-mimic Transpiration Cooling Using Temperature-Sensitive Hydrogel”, CIESC Journal, 63, 2025-2032, 2012.

PATENTS

1. X Hu, Y Hu, **S Cui**, “Multi-purpose Hydrating Device for Ultra Mobile Electronic Equipment”, CN 20120172041.5

ABSTRACT OF THE DISSERTATION

Thermal Transport and Transformation in Micro-Structured Materials

by

Shuang Cui

Doctor of Philosophy in Engineering Sciences (Mechanical Engineering)

University of California San Diego, 2018

Professor Renkun Chen, Chair

Environmentally sustainable forms of energy will be required to meet the aspirations of a growing world population. By 2050, an expected rise in global population from seven billion to ten billion and better living standards could lead to a two to threefold increase in energy consumption. No single technology will fulfill this demand. Therefore, the developments of sustainable power sources and energy-efficient technologies are of great importance to meet the challenges of world's growing energy need. In this dissertation, thermal transport and transformation in micro-structured

materials for applications in long-term source of power supply by nuclear fusion, as well as in energy-efficient thermal management for buildings are discussed.

Tungsten (W) has been chosen as one of the most promising plasma facing materials (PFMs) because of its high melting temperature, high thermal conductivity, high sputtering threshold energy, and low sputtering erosion yield. However, it is suffered from bombardment of neutrons, energetic ions, helium (He) plasma as well as hydrogen isotopes (H, D, T) plasmas. As a result, exposed surfaces exhibit nanostructured surface morphology change that in turn modify thermo-mechanical properties of materials and ultimately impact the performance of PFMs such as the surface temperature and erosion yield. A differential method, 3 ω method, with improved measurement sensitivity was used to study the impact of heavy ions (as a surrogate of neutrons) and He plasma on the thermal conductivity of W. The results show a significant gradual reduction in thermal conductivity for W irradiated at room temperature, spanned from 10^{-3} to 0.6 dpa for Cu ions with increasing Cu ion damage level due to defects introduction, such as dislocation loops, self-interstitials (SIAs) and vacancies during irradiation, which scatters the electrons, the dominant heat carriers in W. When the Cu ion irradiation was performed at 1000 K, the reduced thermal conductivity for 0.2 dpa sample gets recovered to around 80% of the pristine value, attributing to the thermal annealing and annihilation of the irradiation induced defects, i.e. through vacancy/SIAs recombination. Meanwhile, at least ~80% reduction in thermal conductivity happens to W bulk and thin film irradiated by helium (He) plasma compared to that of undamaged W. This large reduction in thermal conductivity also comes from defects introduced during He-plasma irradiation. Those studies on thermal

conductivity of PFMs under fusion relevant irradiation conditions need to be taken into consideration in the thermal design of future nuclear fusion reactors.

Residential and commercial buildings are one of the highest energy consumption sectors and over 40% of energy consumption and greenhouse gas emission are related to building temperature regulation. The second thrust of the dissertation is focused on the development and application of polymeric materials for thermal management in buildings to reduce the energy consumption. For the first time, the application of highly stretchable and tough double network hydrogels (DN-Gels) was proposed as durable and reusable 'sweating skins' for cooling buildings. These DN-Gels demonstrate outstanding cooling performance, reducing the top roof surface temperature of wooden house models by 25—30°C for up to 7 hours after only a single water hydration charge. DN-Gels also exhibit extraordinary toughness and cyclability due to their interpenetrated ionically and covalently cross-linked networks, as demonstrated by constant cooling performance over more than 50 cycles. Our results suggest that bio-inspired sweat cooling, specifically using tough DN-Gel coatings, represents a promising energy-efficient technology for cooling buildings with reduction of ~290 kWh of annual electricity consumption for air conditioning and 160 kg of CO_2 emission.

Besides, a thermo-responsive hydrogel composite (TRHC) desiccant is also synthesized by impregnating hygroscopic salt into porous thermo-responsive polymer matrix, for desiccant assisted air conditioning. Unlike traditional solid desiccant that has a tradeoff between its adsorption and desorption due to its fixed affinity to vapor, TRHC desiccant has drastically different affinities to water upon phase transition thanks to its thermo-responsive matrix. It achieves faster desorption at low-temperature (50°C) as

well as high adsorption capacity. With the attractive performance of TRHC desiccants, the COP of desiccant assisted air conditioning could be improved compared to that with silica gels, which consumes higher temperature/energy for reactivation under similar operating conditions.

1 Chapter 1 Introduction

Nowadays, 80% of the developed world's energy comes from fossil fuels. Environmental problems—the greenhouse effect and the effects of acidic pollution—and diminishing fuel supplies mean that reliance on coal, gas and oil will have to be severely constrained. Nuclear fission will continue to make a major contribution to electricity generation, but its growth could be curtailed by issues of public and political acceptability, especially after Fukushima nuclear disaster in Japan in 2011. Supplies from renewable sources are reliant on environmental conditions, and therefore not guaranteed to be constant. They are also subject to technology challenges of energy storage. To provide constant baseload electricity, predictable and non-varying sources of energy are needed. Nuclear fusion offers a secure and environmental friendly power supply with no production of greenhouse gases, no long-lived radioactive waste, and almost unlimited fuel supplies. Therefore, fusion energy could have a key role to play in the energy market of the future, with the potential to produce at least 20% of the world's electricity by 2100. But strict safety standards are required for the thermomechanical properties of the in-vessel components that are exposed to severe irradiation and heat fluxes. Therefore, it is of great importance to study the thermal properties of plasma facing materials (PFMs) under fusion relevant radiation conditions.

To alleviating the energy crisis, the sustainability challenges concerning energy saving and environment protection also require major changes[1-3] not only in the way that energy is supplied, but also in the way that it is consumed. A special focus should be given to the building sector because it is considered as the biggest single contributor to world energy consumption and greenhouse gas emissions.[4-5] Currently, building energy use

accounts for over 40% of total primary energy consumption in the U.S. and E.U..[6] Nevertheless, significant energy savings can be achieved in buildings if they are properly designed, constructed and operated.

1.1 Overview of plasma facing materials in nuclear fusion reactors

1.1.1. History and applications of plasma facing materials

Fusion materials research started in the early 1970s following the observation of the degradation of irradiated materials used in the first commercial fission reactor. The technological challenges of fusion energy are intimately linked with the availability of suitable materials capable of reliably withstanding the extremely severe operational conditions of fusion reactors.[7] Today, the nuclear fusion of a deuteron (^{2}H) and a triton (^{3}H) is considered to be the most promising reaction for a commercial fusion power plan: $^2H + {}^3H \rightarrow {}^3He\ (3.5\ MeV) + n\ (14.1\ MeV)$. To overcome the Coulomb repulsion between the deuteron and the triton, plasma temperatures of about 20 keV (~2×10^8 K) are required, a challenge not only for plasma physicists but also for material scientists dealing with plasma-wall interactions and the lifetime of plasma-near in-vessel components.

Neutrons have about the same mass as protons; however, unlike protons, they can strongly interact with atoms at very low energies. Degradation of materials under neutron irradiation was already anticipated in 1946 by Eugene Wigner, who argued that neutrons could displace atoms through irradiation, thus permitting the artificial formation of displacements in definite numbers.[8] The associated effects are the changes on thermal and electrical conductivity, tensile strength, and ductility, etc. The integration of the flux in a

certain period of time—the fluence—and the absorbed dose are two parameters typically used to characterize the exposure of plasma facing materials (PFMs). Under neutron irradiation, in the first stage after collision, a primary knock-on atom (PKA) is generated: the primary atom that recoils after being impacted by the neutron. Figure 1.1 illustrates the pathways of irradiation damage. Following the first impact, if no excited state is generated, the PKA recoils quasi-elastically and dissipates its initial kinetic energy by exciting the electrons of the medium and by elastic collisions with surrounding atoms of the impacted material. The total kinetic energy of the atoms involved in the recoiling is nearly conserved. The sum of the energies of the colliding and the collided secondary atom after scattering is basically the same as that of the incident PKA, giving or taking the relatively small individual electron excitation energies. Each PKA is capable of displacing a large number of secondary atoms, the number of which is determined by the combination of the total amount of energy available and the energy required to displace an atom.[9-11] Thus, if the secondary atoms impacted by the PKA acquire enough kinetic energy to be displaced from their lattice sites, a cascade of successive collisions might take place, typically with a tree-structure shape. This scenario occurs in the materials exposed to fusion neutrons of 14.1 MeV. Such collisions knocking out atoms would produce a distortion in the lattice by leaving behind a vacancy by the recoiling atom which, in turn, would become an interstitial being lodged in a nearby location.

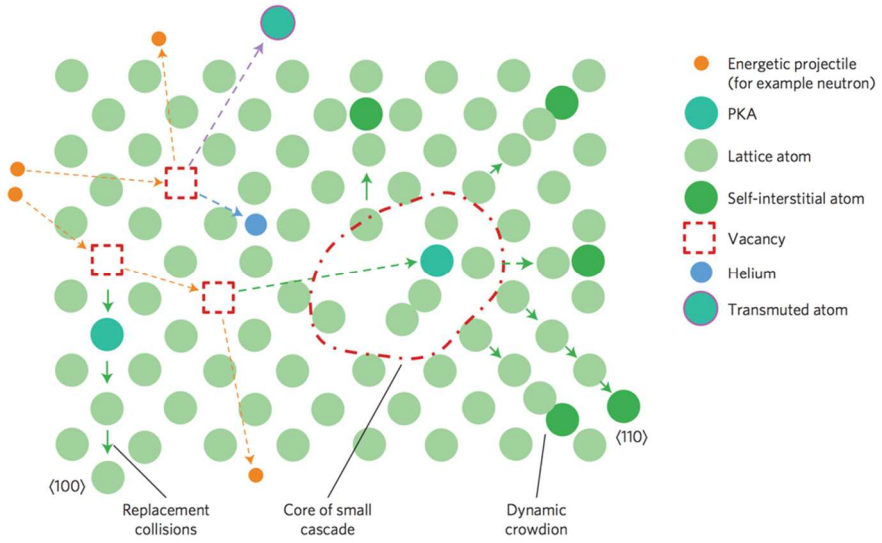

Figure 1.1. Schematic illustration of irradiation damage.[7]

The recoiling primary atom will mainly slow down owing to electronic inelastic interactions or elastic collisions with nearby atoms. The ratio of electronic versus nuclear stopping power and the rate at which energetic recoils lose kinetic energy are well understood in terms of Lindhard's theory.[12] The related Stopping and Range of Ions in Matter (SRIM) code has become a worldwide standard for the calculation of the stopping power and range of ions while propagating through matter.[13]

Besides, substantial gaseous (H and He) are also produced during nuclear fusion reactions, which substantially speed up the embrittlement of nuclear fusion material. As a result, thermodynamically unstable microstructures evolve swiftly into more stable configurations. In turn, the remaining defects tend to agglomerate into clusters that are strongly dependent on the temperature of the irradiated materials and the defect concentration,[14-15] often leading to a severe degradation of materials properties. This is why

research on materials considering radiation resistance or radiation tolerance, are still one of the highest priorities within the international fusion communities.

1.1.2. The influence of nuclear fusion relevant damage on thermal conductivity of plasma facing materials

Tungsten (W) is considered as a promising plasma facing materials (PFMs) for ITER because of its high thermal conductivity, high sputtering threshold energy, and low sputtering erosion yield.[16] During nuclear fusion reactions, the surface of PFMs is well known to experience damages as discussed earlier[17-20] in section 1.1.1 because of being subjected to the very high fluxes of plasma, energetic ions, and neutrons bombardment. Those damages will alter the surface material properties, such as morphology and could lead to reduced thermal conductivity, which may also result in a higher surface temperature inducing larger thermal stresses in the near-surface regime of PFMs, especially in the case of large transient heat loads (up to 10 GW/m^2 for short durations of a few ms during plasma disruptions and ~0.5 ms for edge localized modes).[21-22]

In the case of transient heat loads (Q_t) with a short duration of 0.5 to a few ms, the thermal penetration depth (L_p) can be significantly shorter than the overall thickness of PFMs. According to one-dimensional heat diffusion equations,[23] L_p is defined as

$$L_p \approx \sqrt{2\alpha t} = \sqrt{\frac{2t\kappa}{\rho C}} \quad (1.1)$$

Where α is the thermal diffusivity, ρ is the density, C is the specific heat of the PFMs, and t is the duration of the transient heat load. Based on the thermophysical properties of W, for $t = 0.5-2$ ms, L_p ranges from 200 to 400 μm, the near-surface regime

of PFMs, despite its small thickness, would play an important role in dictating surface temperature (T_s) and consequently the thermo-mechanical behaviors.

To illustrate the important effect of near-surface thermal conductivity on the temperature distribution in PFMs when subjected to transient heat loads, the surface temperature evolution of a hypothetical PFM made of W with a thin near-surface regime of 10 μm thick was modeled,[24] as shown in Figure 1.2(a). The transient heat load Q_t is 2 GW/m^2 with a duration of 0.5 ms, typical for localized edge modes.[21-22] In this model, the substrate of the PFM has the thermophysical properties of bulk W (including temperature dependent thermal conductivity κ_{bulk} and specific heat C_{bulk}), while thermal conductivity of the near surface regime (κ_{film}) varied from 10% to 100% of κ_{bulk}. A time-dependent finite element code was used to compute the evolution of the temperature for different cases. Figure 1.2(b) plots the cross-sectional temperature distribution in the PFM at the end of the transient heat flux (t = 0.5 ms), for the case of κ_{film}: κ_{bulk} = 1:2. It clearly shows that the majority of the temperature gradient occurs within the top 200 μm thick regime in the PFMs, meaning that the transient heat load only penetrates into the PFMs by about 200 μm, which is consistent with the result obtained from Equation (1.1). The inset in Figure 1.2(b) also shows that there is a significant temperature gradient within the 10 μm thick near surface regime because of its lower κ.

The time evolution of the surface temperature for various values of κ_{film} is shown in Figure 1.3. T_s is getting higher as κ_{film} is further reduced, but the maximum T_s occurs at t = 0.5 ms for all the cases. The inset in Figure 1.3 plots the maximum T_s vs. κ_{film}, further demonstrating increased T_s as a result of lower κ_{film}. For instance, if κ_{film} was somehow

reduced to 10% of bulk W, T_s would be as high as ~ 4000 K, which would exceed the melting point of W (the model did not take phase change phenomenon into account).

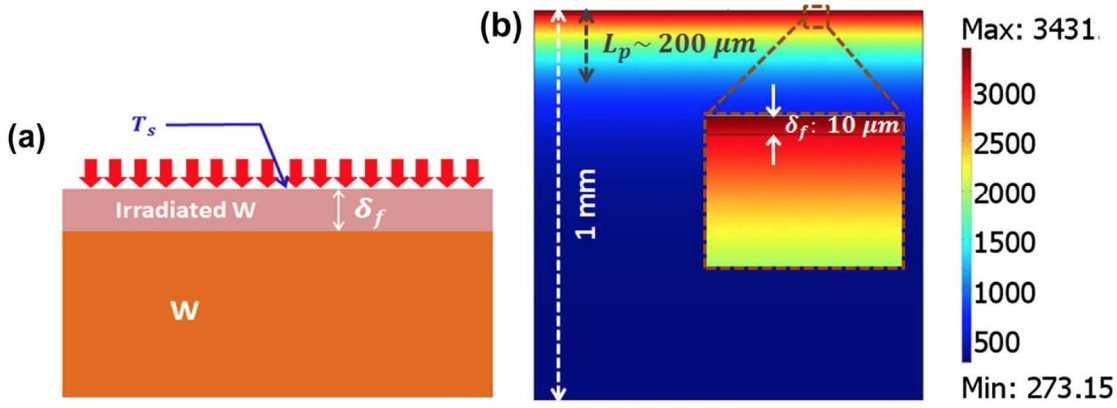

Figure 1.2. (a) A schematic of tungsten (W) with irradiation thickness of $\boldsymbol{\delta_f}$. T_s represents the surface temperature and the red arrow indicate the heat load. (b) Simulated cross-sectional temperature profile of W under transient thermal loading (Q_t = 2 GW/m^2) at the end of the heat load duration (t = 0.5 ms) when thermal conductivity of the top irradiated layer ($\boldsymbol{\delta_f}$ = 10 $\boldsymbol{\mu}$m) is half of the W substrate ($\boldsymbol{\kappa_{film}}$: $\boldsymbol{\kappa_{bulk}}$ = 1:2). The color represents the temperature in accordance to the color scale on the right. Inset: zoom-in temperature profile near the surface, which shows large temperature gradient across the film.[24]

The modeling result shown highlights the importance of the near-surface thermophysical properties of PFMs on the surface temperature, especially in the case with large transient heat loads. The higher surface temperature may pose severe challenges for the operation of fusion reactors. It may exceed the melting point of W and directly cause the failure of the PFMs. The associated large thermal stress in the near-surface regime consequently leads to failure of PFMs via delamination or cracking. Therefore, understanding the thermal properties of this thin damaged regime is vital in consequently the thermo-mechanical behaviors.

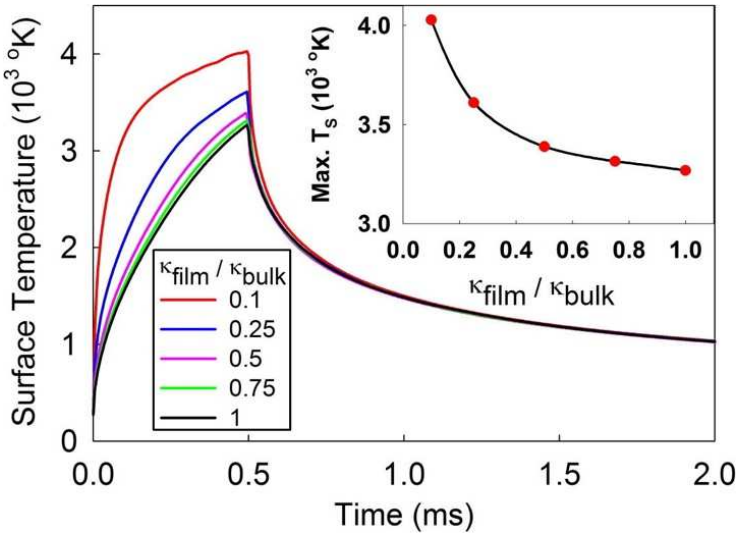

Figure 1.3. Time evolution of surface temperature T_s under an applied transient heat flux (Q_t = 2 GW/m^2 and t = 0.5 ms) for samples with various $\boldsymbol{\kappa_{film}}$ values. Inset: Maximum T_s vs. $\boldsymbol{\kappa_{film}}$ values, showing increasing T_s with lower $\boldsymbol{\kappa_{film}}$.[24]

1.1.3. Thermal measurement technique for plasma facing materials

Laser flash techniques[25-27] and electrical resistivity measurements[28] are used to study the thermal transport in bulk PFMs before. However, as the damaged regime is only nanometers to microns thick, conventional steady state thermal conductivity measurement techniques are not applicable. Therefore, the thermal transport properties of ion-damaged layer are as yet largely unexplored due to the lack of suitable experimental techniques. Recently, thermal reflectance measurements,[29-30] non-contact laser-induced transient grating (TG) technique,[31-32] and 3ω technique[24] have been proposed to quantify thermal transport in thin, ion-irradiated surface layers.

The widely used time domain thermoreflectance (TDTR) technique has good potential for thermal measurement of thin ion-irradiated W because the modulation frequency of the excitation source can be conveniently adjusted to confine the thermal

wave to a thin layer at the surface of the material.[33] A thin metallic layer deposition is required by TDTR, measuring the ps to ns time evolution of surface temperature by thermoreflectance. With TDTR, a reduced thermal conductivity is found in both high temperature proton irradiated single crystal silicon,[29] UO_2 upon irradiation with 3.9 MeV of He ions,[30] as well as He ion-implanted W.[34] However, the film introduces a number of unknown parameters, such as film thickness and interface thermal resistance, adding difficulty to the signal analysis required to extract the thermal properties of the substrate.

Recently, a non-contact laser-induced transient grating (TG) technique is applied to measure the thermal transport properties of He-implanted W.[32] It uses two shot excitation laser pulses that are overlapped on the sample with a well-defined crossing angle (Figure 1.4(a)). Interference of the pulses produces a spatially sinusoidal intensity grating with a fringe spacing λ.[35] Absorption of the light leads to a temperature grating with period λ. Rapid thermal expansion also launches two counter-propagating surface acoustic waves (SAWs).[36] Both the thermal grating and the SAWs cause displacements of the sample surface. These are detected by diffraction of a quasi-continuous probe beam, heterodyned with a reflected reference beam (Figure 1.4(b)). Figure 1.4(c) presents the signal measured from a pure W sample showing a number of oscillations, due to the propagating SAWs, superimposed on a background due to the decaying temperature grating. On the surface of bulk samples thermal transport occurs both in-plane from peaks to troughs of the thermal grating, and into the depth of the sample. The surface profile due to the thermal grating follows a non-exponential decay.[35]

$$\frac{\partial u_z}{\partial x} \propto erfc(q\sqrt{at}) \quad (1.2)$$

Here $q = 2\pi/\lambda$, t is time and α is the isotropic thermal diffusivity, $\alpha = \kappa/C$, where κ is thermal conductivity and C is the volumetric heat capacity. Thermal diffusivity is determined by fitting Equation 1.2 to the experimental data, also taking into account the sinusoidal variation due to SAWs. Figure 1.4(c) shows the fitting to pure W data. The accuracy of TG measurement is intrinsically high since the technique does not rely on measuring a temperature difference or heat flux. It also has the advantage over TDTR measurement without sample coating when a well-polished sample surface allows specular reflection of the probe and reference beam is sufficient. However, the surface of damaged sample might be rough under specific severe ion/plasma damage, which is not flat enough for TG measurement.

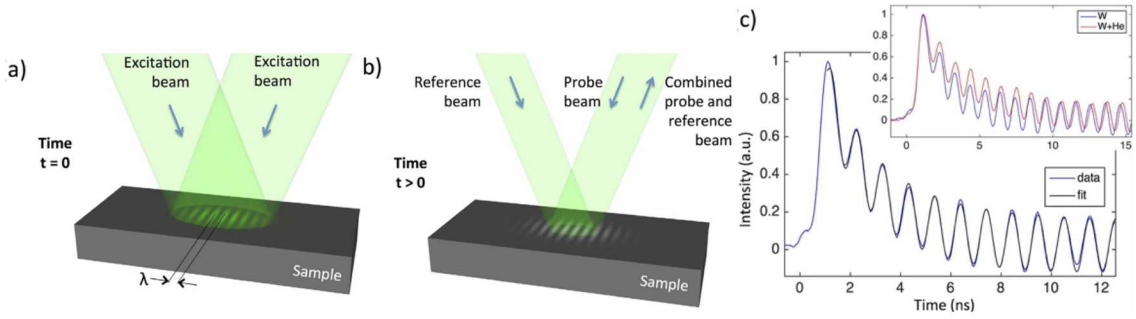

Figure 1.4. Transient grating thermal transport measurement.[32] (a) Schematic of the measurement setup, showing the excitation beams (at time t = 0) that form the periodic transient grating light pattern (shown schematically in green) on the sample. (b) At time t > 0, the temperature grating the counter-propagating surface acoustic waves at the sample surface (both shown schematically in light grey) are probed. For heterodyne detection the scattered probe beam is combined with a reflected reference beam. (c) Experimentally recorded time trace of scattered probe intensity for the pure W sample at 296 K. Also shown a fit to the experimental data. Inset are time traces recorded for pure W and W implanted with 3100 appm of He, both at 296 K. Thermal grating decays in the implanted sample is visibly slower.

Recently, a frequency domain method, 3ω method,[37] was employed to measure the thermal conductivity of the micro-sized near-surface damaged regime of PFMs, a 1 μm thick damaged W layer by Cu^{2+} ion irradiation.[24] The penetration depth (δ_p) of a periodic heat fluxes with frequency ω_q is defined as,

$$\delta_p = \sqrt{\frac{2\alpha}{\omega_q}} = \sqrt{\frac{2\kappa}{\rho C \omega_q}} \quad (1.3)$$

where α is the thermal diffusivity, κ is the thermal conductivity, ρ is the density, and C is the heat capacity. In a typical 3ω measurement, a narrow metal strip functions as both a heater for applying a periodic heat flux and a thermometer for measuring the surface temperature, as shown in Figure 1.5.

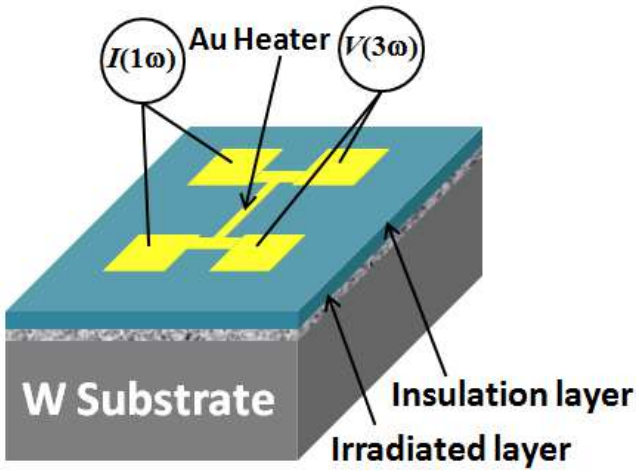

Figure 1.5. Schematic diagram of a device for 3**ω** measurement for the ion damaged layer (~1 **μ**m thick) in W. An insulation layer of Al_2O_3 is deposited using Atomic Layer Deposition (ALD) to prevent electrical leakage between the Au heater and the W sample.

By applying an AC current modulated with angular modulation frequency ω, I_ω, through the metal strip, the periodic heating will give rise to heat flux oscillating at 2ω, expressed as,

$$\mathrm{P} = [I\sin(\omega t)]^2 R = \frac{I^2 R}{2} - \frac{I^2 R}{2}\cos(2\omega t) \text{ (1.4)}$$

which includes a DC component and a 2ω component. The latter term leads to a temperature rise oscillating also at 2ω with a phase shift ϕ. Sine the resistance change of the metal strip is proportional to the temperature change, the resistance will also oscillate at 2ω, which leads to a third harmonic voltage

$$V_{3\omega} = I_{\omega} R_{2\omega} \text{ (1.5)}$$

depending on the AC temperature rise ($T_{2\omega}$) of the heater,

$$V_{3\omega} = \frac{I}{2}\frac{dR}{dT} T_{2\omega}\sin(3\omega t + \phi) \text{(1.6)}$$

where $T_{2\omega}$ is the 2nd harmonic component of the temperature rise, which depends on the thermal conductivity of the materials, as shown in the heat conduction model below. Therefore, by extracting $T_{2\omega}$ from the measured $V_{3\omega}$ signal according to Equation 1.6, one can obtain the thermal conductivity of the sample, hence the term "3ω method".

Based on the specific geometry and the thermal properties of the W samples and the thin damaged layers, a generalized 2D heat conduction analysis for the 3 ω measurements to establish the relationship between material thermal conductivity and the measured surface temperature was built. By assuming a uniform heat distribution between the heater and the top film (i.e., no thermal contact resistance in between) and considering 2D heat conduction from the heater strip to the underlying materials, the temperature rise on the metal strip is written as:[38]

$$T_{\text{rise}} = \frac{-p}{\pi l \kappa_{y_1}} \int_0^{\infty} \frac{1}{A_1 B_1} \frac{\sin^2(b\lambda)}{b^2\lambda^2} d\lambda \text{ (1.7)}$$

where

$$A_{i-1} = \frac{A_i \frac{\kappa_{y_i} B_i}{\kappa_{y_{i-1}} B_{i-1}} - \tanh(B_{i-1} d_{i-1})}{1 - A_i \frac{\kappa_{y_i} B_i}{\kappa_{y_{i-1}} B_{i-1}} - \tanh(B_{i-1} d_{i-1})}, \; i = 2 \ldots \text{n} \quad (1.8)$$

$$\mathrm{B}_i = \left(\frac{\kappa_{x_i}}{\kappa_{y_i}} \lambda^2 + \frac{i2\omega}{\alpha_{y_i}}\right) \quad (1.9)$$

where T_{rise} is the temperature rise, p is the power dissipated in the heater, l is the heater's length, b is the heater's half width, d is the layer thickness, n is the total number of layers, κ_x and κ_y are in-plane and cross-plane thermal conductivity, respectively, λ is the variable of integration, and i is the i^{th} layer of the measured sample with $i = 1$ being the substrate.

1.2 Overview of thermal regulation for buildings

1.2.1 Introduction of energy consumption in buildings

More than half of the world's population lives in an urban environment and this number is expected to further increase to 70% by 2050.[39] The cohabitation of many people on a small space creates new challenges in waste management and fresh water supply but also a high demand in energy. The ratio of building energy consumption to total energy consumption increased from 33.7% to 41.1% between 1980 and 2010 in the U.S..[6] The Energy Information Administration (EIA) predicted that this growth would resume steady growth through 2035. The main contributors of the energy consumed in building utilities can be tracked back to cooling and heating because most people currently spend 90% of their daily lives indoors and relying on mechanical heating and air conditioning for thermal comfort. This demand for AC load is estimated to be increased by 6.2% annually.[40] Therefore, it is appealing to develop alternative cooling technologies to assist or even substitute the conventional vapor compression (VC) cooling systems, which consume

excess electricity during operation and have limitation in dealing with high latent heat load for hot and humid climate.[41]

1.2.2 State-of-art thermal regulation technologies for buildings

Novel sustainable concepts for alternative building thermal regulation technologies, especially for building cooling, have been proposed in the past decades.[42-44] Most promising solutions are based on passive systems (i.e., no electricity needed) directly integrated in the roof or the façade of buildings. For instance, porous materials have been used to store and release water, provoking evaporative cooling;[45] night-time ventilation has been employed in moderate or cold climate to promote convection;[46-47] and high IR reflective coating to reduce the energy uptake as a result of solar irradiance.[48-49] Nevertheless, no current passive cooling technologies used in buildings possess ideal characteristics such as high cooling efficiency under a variety of weather conditions, high durability including resistance to thermal cycling and UV irradiation, and low cost. For example, Phase changing materials (PCMs) are less effective under high solar intensity fluctuations due to their low latent heat (~hundreds of kJ/kg).

Besides passive cooling, active cooling, such as vapor compression (VC) air conditioning also attract lots of attention in efficiency improvement and environmental friendly requirement. Desiccant assisted air conditioning is one of the most promising technologies to supply or even substitute VC air conditioning because it can separately treat latent and sensible heat loads by pre-dehumidifying the moist air with desiccants, applicable to lots of hot and humid environment.[50] Moreover, Desiccant assisted air conditioning is environmental friendly as water is usually used as refrigerant instead of

chlorofluorocarbon (CFC) refrigerants in VC air conditioning systems.[51] It is also compatible with low-grade thermal energy, e.g., solar or waste heat,[52-54] for desiccant regeneration, thus having a large energy saving potential. Desiccant assisted air conditioning system can be classified into liquid desiccant cooling (LDC) system and solid desiccant cooling (SDC) system.[55] And its performance is determined by the geometry of the systems and the characteristics of the applied desiccants, most notably the adsorption/absorption rate, adsorption/absorption capacity, and the regeneration temperature.[56] LDC system has slightly higher COP by using liquid desiccants such as LiCl or $CaCl_2$ with high absorption capacity over solid desiccants such as silica gel, zeolite, and activated carbon.[57] But it involves lots of expansion valves due to pressure difference and induces corrosion due to deliquescence after absorbing moisture during operation.[58] In comparison, SDC system is more user friendly and spontaneously adsorbing/desorbing moisture through rotating desiccant wheels.[59-61] However, its performance is hindered by characteristics of solid desiccants. Therefore, more efficient and durable solid desiccant materials are desired for high coefficient of performance (COP) of sustainable air conditioning for building cooling.

1.3 Thesis structure

Chapter 1 provided a brief introduction to thermal measurement on plasma facing material under nuclear fusion relevant radiation and emerging thermal regulation techniques for building cooling.

Chapter 2 discussed the thermal conductivity of room-temperature irradiated W by copper (Cu) ions and tungsten (W) ions. One set of W damaged by Cu ions with increasing

damage level (quantified by displacement per atom, dpa) were first utilized to study the influence of damaged level on the thermal conductivity of plasma facing materials (PFMs). The other set of room-temperature and high-temperature irradiated W by Cu ions at the same damage level (0.2 dpa) were used to study the effect of irradiation temperature on the thermal conductivity. At last, a comparable study of the irradiation ion species' influence on the thermal conductivity was conducted by replacing the Cu ions with W ions at 0.2 dpa. To get a better measurement sensitivity for thermal measurement of this thin irradiated W layer, an improved 3ω technique was demonstrated with higher measurement sensitivity through novel nanofabrication.

Chapter 3 studied the He plasma damage effect on the thermal conductivity in both bulk and thin film, W through improved 3 ω technique and electrical resistivity measurement. ~80% thermal conductivity reduction was observed in both He-plasma irradiated bulk and thin film W.

Chapter 4 demonstrated a bio-inspired regenerable 'sweating skin' for building cooling, by mimicking the transpiration of plants and animals to autonomously adaptive to the increases in environmental temperature. This sweating skin, made of a highly stretchable and tough double network hydrogels (DN-Gels), has been demonstrated an excellent evaporative cooling performance as well as extraordinary toughness and cyclability over 50 cycles on a minimized house model.

Chapter 5 developed a thermo-responsive hydrogel composite (TRHC) desiccant for desiccant assisted air conditioning with high coefficient of performance (COP) to assist or even substitute the conventional vapor compression (VC) cooling systems, which

consumes excess electricity during operation and has limitation in dealing with high latent load for hot and humid environment.

Chapter 6 summarized the dissertation and described potential future directions.

2 Chapter 2 Thermal Transport in heavy ion irradiated tungsten

2.1 Introduction

Tungsten (W) has been chosen as the armor material for the divertor in ITER,[62] and it is a leading candidate for the first wall in future demonstration fusion power reactors (DEMO) because of its high melting point, high thermal conductivity (κ), low sputtering yield, and low hydrogen permeability.[62-64] During the operation, the armor will experience high steady-state heat load up to 10 MW/m^2 and even higher transient heat flux, as well as neutron irradiation and helium bombardment, inducing a damage cascade within the material. During the lifetime of a fusion reactor, the damage level is expected to build up to several hundred displacements per atom (dpa),[65] resulting in multiple types of defects such as self-interstitial atoms (SIAs), vacancy clusters, dislocation loops, and voids.[66] These forms of damage lead to changes in microstructure, which in turn could degrade the thermal and mechanical properties of the material.[67] The degradation in κ of various materials used in fusion reactor has been reported, including W,[32, 34] tungsten-rhenium alloys,[25] and silicon carbide.[68] The combined effect of reduced thermal conductivity and radiation embrittlement leads to cracking in W as a result of the thermal cycling, which in turn poses serious concerns on the system performance and safety. However, direct study on thermal transport properties of neutron damaged W is still largely unexplored due to challenges associated with the preparation and handling of those activated samples and also the lack of high flux neutron sources to produce a fusion-relevant fluence in a short period of time.[69] Thus, heavy ion irradiation is used as a surrogate for high-energy neutrons to simulate the effect of neutron irradiation on metals[70-73] for multiple reasons: [i] separate

effects due to direct displacement damage caused by neutrons and by transmutation products such as gas evolution; [ii] accelerate materials testing to extremely high dpa levels within a short time; [iii] avoid the additional cost and difficulty of handling neutron activated materials. One drawback with the heavy irradiation, however, is the shallow damaged region (only a few microns) into the material. Although the microstructural characterization (e.g., by transmission electron microscopy (TEM)[74-75] and grazing angle X-ray Diffraction (XRD)[76]) and deuterium retention (e.g., by thermal desorption spectroscopy (TDS)[77] and nuclear reaction analysis (NRA)[78]) have been routinely carried out on the shallow irradiated regions in W, the thermal conductivity measurement of such a shallow region is substantially more challenging.[79] Recently, two new approaches, the 3ω technique[24, 80-81] and optical thermo-reflectance measurement[29-30] have been employed to characterize κ in the thin, ion irradiated surface layers. These measurements showed significant κ reduction in the surface layer of W when exposed to irradiation (i.e., proton, helium and Cu ions) at high fluence and at room temperature. The suppressed κ is thought to mainly originate from the point defects produced during the displacement damage, which act as scattering sites for heat carriers, primarily electrons in W. However, these measurements have only investigated one or a narrow range of dpa levels[24, 34] on W samples irradiated near room temperature only. The high-temperature annealing effects have been observed from the deuterium retention and TEM analysis,[82-85] which showed that the annealing could largely annihilate the irradiation-induced defects. Such annealing should also impact κ; thus a systematic study on the dependence of κ on the damage level, and more importantly, on the irradiation temperature, is of great interest since the operation temperature for W armor is estimated to be between 373 K and 1273 K.[85] Therefore, in this

work, we seek to understand how this defect recovery impacts the κ of W irradiated at an elevated temperature that is relevant to the operation conditions of fusion reactors. Additionally, thermal conductivity measurement could serve as a sensitive and convenient interrogation tool to probe the point defects in the material, as κ is sensitive to scattering of both electrons and phonons. Here, we systematically measured κ of W irradiated by Cu ions with dosage level from 10^{-3} to 0.6 dpa using an improvement to the 3ω technique previously developed. We then used the same technique to measure κ of W irradiated by Cu or W ions at both room temperature and 1000 K, with a damage level of 0.2 dpa, in order to study the effect of irradiation temperature and ion species.

2.2 Preparation of heavy ion irradiated W

W samples were prepared for irradiation with energetic heavy ions (either Cu or W ions). A polycrystalline W rod with 99.95% purity (Midwest Tungsten) was cut into small disks, 6 mm in diameter and 1.5 mm thick. The surfaces to be exposed to radiation were mechanically polished down to 3 μm grit, then ultrasonically cleaned in acetone and ethanol. Afterwards, the specimens were annealed in a vacuum furnace below 10^{-4} Pa for 1 hour at 1173 K to further relieve the mechanical stress built up during polishing and to reduce intrinsic defects and dislocation. Then the disks were electrochemically polished to a mirror-like surface finish using an electrolyte of 1% NaOH aqueous solution at 8V for 1 minute.

Homogeneous ion implantations were performed in Ion Beam Materials Laboratory (IBML) at Los Alamos National Laboratory (LANL) and at Peking University (PKU). The depth profile is calculated by the Stopping and Range of Ions in Matter－2012 (SRIM-

2012) code using the "Quick calculation of Damage" mode with the Kinchin and Pease model following the "energy damage" method introduced by Stoller *et al*.[86] The displacement threshold was set to 90 eV. One set of 3 polished W samples were irradiated by a tandem ion accelerator with Cu ions at room temperature at LANL, producing an estimated damage level of 10^{-3}, 10^{-2}, and 0.6 dpa to study the effect of damage level on thermal conductivity. The other set of 4 polished W samples were irradiated at PKU at room temperature and at 1000 K by either Cu or W ions with an estimated damage level of 0.2 dpa to study the influence of irradiation temperature and ion species on thermal conductivity. The details of the specimen conditions used in this work are summarized in Table 2.1.

Table 2.1. Experimental parameters for W samples, including irradiated ion type, temperature during irradiation, and dpa.

Ion type	**DPA & Temperature**					**Provider**
	10^{-3}	10^{-2}	0.2		0.6	
Cu	300 K	300 K	-		300 K	LANL
Cu			300 K	1000 K		PKU
W			300 K	1000 K		

The multi-energy ion irradiation conditions defined in Table 2.2 were calculated by SRIM to produce uniform damage profile in W. A relatively flat defect concentration region extended up to 0.9 μm produced by Cu ions with sequential irradiation using three energies (700 keV, 2 MeV, and 5 MeV) each with a specific fluence (Figure 2.1(a)). Similarly, two energies (2.2 MeV and 7MeV) of W ions produced a uniform damage profile in W up to 0.45 μm, as shown in Figure 2.1(b). The damage depth of W ion

implantation is shallower (Figure 2.1(c)) compared to that of Cu ion implantation since Cu ions are lighter and can penetrate deeper into W with comparable energies. Note that the dpa scales linearly with the ion fluencies quoted in Figure 2.1.

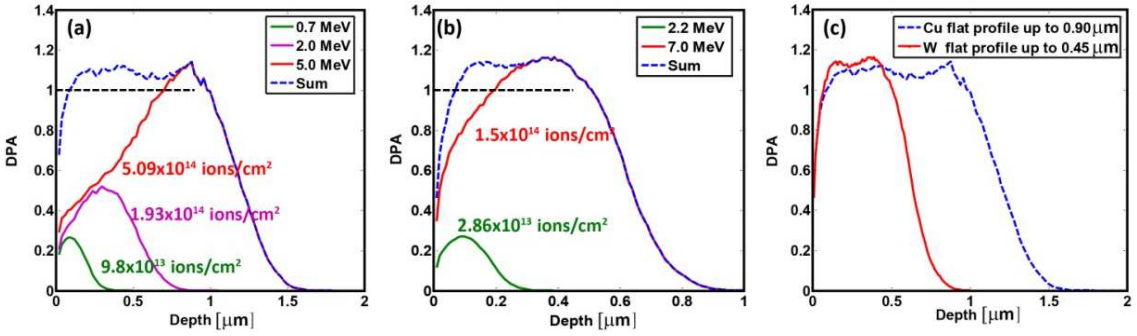

Figure 2.1. Estimated depth profile of displacement damage and implanted ion range distribution in W samples irradiated by Cu^{2+} or W^{4+} ions calculated for 1 dpa using the SRIM code. Different implanted ion range distribution can be normalized with proportionate fluence of 1 dpa profile. (a) Three irradiations by Cu^{2+} ions with different energy and fluence levels were used to produce a nearly flat dpa profile (blue dashed line) within the 0.9 **μ**m depth. (b) Two irradiations by W^{4+} ions with different energy and fluence levels were used to produce a nearly flat dpa profile (blue dashed line) within the 0.45 **μ**m depth. (c) Comparison of the flat dpa profile between Cu^{2+} ions and W^{4+} ions, showing a thicker implantation thickness with the Cu^{2+} ions.

Before room temperature ion implantation, the sample was mounted to the sample holder, which has a heating element and cooling air pathway embedded inside. To ensure damage uniformity, the ion irradiation was then performed by raster scanning across an area larger than the sample with the frequency 517 Hz in horizontal direction and 64 Hz in vertical direction at both LANL and PKU. These rastering rates are believed to minimize swelling and other microstructural evolution except ion implantation.[87-91] Prior to reaching the sample, the ion beam was masked to allow the center of the scan to reach the sample while indirectly measuring the current by Faraday cups at four corners every thirty minutes to guarantee the same beam current both at LANL and at PKU. Once the desired ion dosage

was reached, the beam was turned off. Before high temperature ion irradiation, the sample holder was heated to and held at the desired temperature (1000 K). Samples were concurrently irradiated with heavy ions to dynamically anneal defects during their production, referred as dynamic annealing here, while keeping other steps the same as room temperature ion implantation. The sample holder was then actively cooled with pressurized air passing through the sample holder to decrease the temperature within minutes, limiting additional post-irradiation annealing of the defects. During the ion irradiation and cooling down processes, the sample was always kept in vacuum to avoid oxidation. Details of irradiation parameters are summarized in Table 2.2.

Table 2.2. Cu and W ion irradiation parameters at 300 K and 1000 K used to produce a uniform 0.2 dpa damage profile up to 0.9 and 0.45 **μ**m, respectively.

Ion type	Energy (MeV)	Charge	Current (nA)		Time (s)		Fluence (ions/cm^2)
			300 K	1000 K	300 K	1000 K	
Cu	5	2	~36	~40	2796	2647	1.02×10^{14}
	2	1	~5.5	~20	1988	840	3.86×10^{13}
	0.7	1	~15	~22	501	407	1.96×10^{13}
W	7	4	~13	~15	2956	2872	3.00×10^{13}
	2.2	2	~17	~10	252	417	5.72×10^{12}

2.3 Improved 3ω method for thermal measurement

2.3.1 Measurement sensitivity of 3ω method

In the case of thin films measured using the differential 3ω technique, the thermal conductivity is calculated using

$$\kappa_{\mathrm{f}} = \frac{Pt_{\mathrm{f}}}{Lw(\Delta T_{\mathrm{total}} - \Delta T_{\mathrm{ref}})} \quad (2.1)$$

Then considering uncertainties in the calibration of the two samples, $(\mathrm{d}T/\mathrm{d}R)_{\mathrm{total}}$ and

$(\mathrm{d}T/\mathrm{d}R)_{\mathrm{ref}}$, and the geometry it can be shown

$$\frac{\delta\kappa_{\mathrm{f}}}{\kappa_{\mathrm{f}}} = \sqrt{\left(\frac{\delta t_{\mathrm{f}}}{t_{\mathrm{f}}}\right)^2 + \left(\frac{\delta w}{w}\right)^2 + \left[\left(\frac{\Delta T_{\mathrm{ref}}}{\Delta T_{\mathrm{f}}}\right)\left(\frac{\delta\left(\frac{dT}{dR}\right)_{\mathrm{ref}}}{\left(\frac{dT}{dR}\right)_{\mathrm{ref}}}\right)\right]^2 + \left[\left(\frac{\Delta T_{\mathrm{total}}}{\Delta T_{\mathrm{f}}}\right)\left(\frac{\delta\left(\frac{dT}{dR}\right)_{\mathrm{total}}}{\left(\frac{dT}{dR}\right)_{\mathrm{total}}}\right)\right]^2} \quad (2.2)$$

Since $\Delta T_{\mathrm{total}} > \Delta T_{\mathrm{f}}$, the pre-factor for the final term is always greater than one, which indicates that the relative uncertainty of the thermal conductivity always exceeds the uncertainty in the heater calibration. If the temperature drop in the reference sample exceeds that of the film, ($\Delta T_{\mathrm{ref}} > \Delta T_{\mathrm{f}}$), then the background signal is large with the consequence that the second-to-last pre-factor is also greater than one, which exacerbates the issue. If the temperature drop across the film is much larger than the background, $\Delta T_{\mathrm{ref}} << \Delta T_{\mathrm{f}}$, then uncertainties in the calibration of the reference sample become negligibly small. It is clear that the uncertainty in thermal conductivity of thin films will vary depending on the material system under investigation, and therefore no single error estimate can encompass all experiments.

To appreciate the importance good experimental design for the 3ω method, it is instructive to further study the role of the heater calibration. Assuming the relative uncertainty in calibrations is similar from experiment-to-experiment and temporarily neglecting other uncertainties

$$\frac{\delta\kappa_{\mathrm{f}}}{\kappa_{\mathrm{f}}} = \sqrt{\left(\frac{\Delta T_{\mathrm{ref}}}{\Delta T_{\mathrm{f}}}\right)^2 + \left(\frac{\Delta T_{\mathrm{total}}}{\Delta T_{\mathrm{f}}}\right)^2}\,\frac{\delta\left(\frac{dT}{dR}\right)}{dT/dR} \quad (2.3)$$

The prefactor $\chi \equiv \sqrt{\left(\frac{\Delta T_{\mathrm{ref}}}{\Delta T_{\mathrm{f}}}\right)^2 + \left(\frac{\Delta T_{\mathrm{total}}}{\Delta T_{\mathrm{f}}}\right)^2}$ quantifies the sensitivity of κ to the heater calibration. If the contribution of the background signal is ΔT_{ref} / ΔT_{f}, then it can be shown that

$$\chi \equiv \sqrt{1 + 2\alpha + 2\alpha^2} \quad (2.4)$$

This function is plotted in Figure 2.2 for clarity. When the background is large, the sensitivity of the results to the calibration is large,

$$\frac{\delta\kappa_{\mathrm{f}}}{\kappa_{\mathrm{f}}} = \sqrt{2}\frac{\Delta T_{\mathrm{ref}}}{\Delta T_{\mathrm{film}}}\frac{\delta(\frac{dT}{dR})}{dT/dR} \quad (2.5)$$

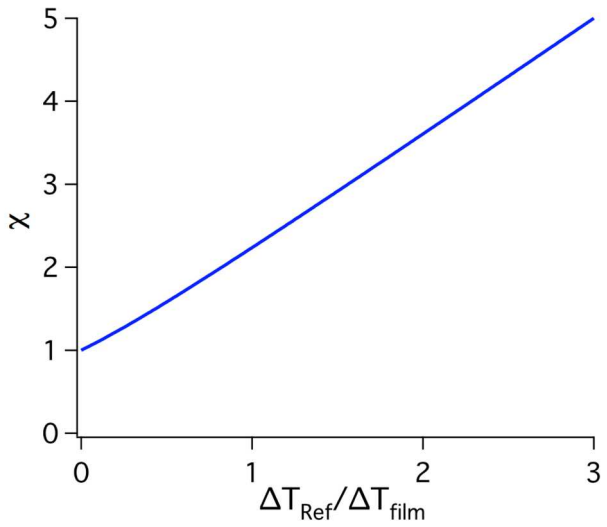

Figure 2.2. Plot of $\boldsymbol{\chi}$ vs. $\boldsymbol{\alpha}$, equation 2.4.

While it is important to achieve a very high quality of calibration, it is equally important to design experiments to reduce the background signal, ΔT_{ref}, to acceptable values. To a good approximation, the ratio ΔT_{ref} / ΔT_{f} is given by

$$\alpha = \frac{\frac{b}{\kappa_{\mathrm{s}}}+\frac{t_{\mathrm{d}}}{\kappa_{\mathrm{d}}}+\frac{t_{\mathrm{s}}}{\kappa_{\mathrm{b}}}}{\frac{t_{\mathrm{f}}}{\kappa_{\mathrm{f}}}} = \frac{b}{t_{\mathrm{f}}}\frac{\kappa_{\mathrm{f}}}{\kappa_{\mathrm{s}}} + \frac{t_{\mathrm{d}}}{t_{\mathrm{f}}}\frac{\kappa_{\mathrm{f}}}{\kappa_{\mathrm{d}}} + \frac{t_{\mathrm{b}}}{t_{\mathrm{f}}}\frac{\kappa_{\mathrm{f}}}{\kappa_{\mathrm{b}}} \quad (2.6)$$

where the subscripts d and b stand for the dielectric layer and buffer layers, respectively. This equation suggests several methods for reducing the uncertainty: (i) choose a high thermal conductivity substrate when possible ($\kappa_{\mathrm{f}} << \kappa_{\mathrm{s}}$); (ii) use the smallest linewidth possible to reduce the substrate contribution; (iii) use a thick sample film when possible; (iv) for all other layers, use the smallest thickness possible. If a value of ~5% for

the calibration uncertainty can be obtained, then according to Equation 2.6, with a value of α less than 3, the experiment can achieve accuracy better than 25%. The current estimate of the calibration uncertainty is based on a statistical analysis and thus is expected to be more realistic.

2.3.2 Higher measurement sensitivity of 3ω method with novel nanofabrication

Compared to the ion irradiated W samples measured with 3ω method previously,[24] the heavy ion irradiated W at high temperature (1000 K) or with low level of damage (10^{-2} and 10^{-3} dpa) have less damage within the damaged layer, which results in less mismatch of κ between the substrate and the ion damaged layer. We modified the sample structure for the 3ω measurement by utilizing additional nanofabrication steps to decrease the thickness of insulation layer to improve the measurement sensitivity (strategy iv discussed in section 2.3.1) since the geometry and the material of the samples are fixed.

As shown schematically in Figure 2.3(a), a 30 nm thick Al_2O_3 layer and a 600 nm thick Parylene layer were first deposited onto the sample surface using the atomic layer deposition (ALD) and a Parylene coater, respectively. Then a narrow groove was patterned on the Parylene layer followed by photolithography and oxygen plasma etching. This allows the 3ω heater line to be deposited directly onto the thin Al_2O_3 layer that lies within the trench formed in the Parylene layer, while the large electrode pads for wire-bonding were deposited on top of the thick Parylene layer, as shown in Figure 2.3(b). The thick Parylene layer underneath the large electrodes prevented the electrical leakage from the electrodes to the W substrate. To avoid thermal measurement signals to be dominated by an insulation layer between W and the heater line, a thin (30 nm) insulating Al_2O_3 film

ensures a temperature drop across an insulating film is relatively small in comparison to a temperature drop across the irradiated W layer (0.45 or 0.9 μm), thus improving the measurement sensitivity and reducing the measurement uncertainties.[92]

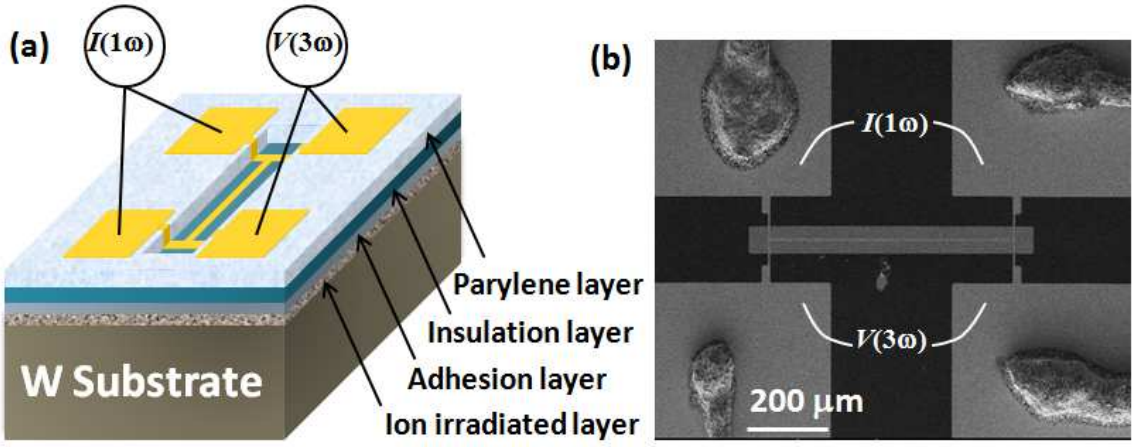

Figure 2.3. (a) Schematic of 3**ω** device for thermal conductivity measurement of thin ion-irradiated W layer. Al_2O_3 and Parylene insulation layers are deposited between heater and W surfaces to prevent current leakage. Electrodes are deposited on a thick Parylene layer to avoid electrical leakage caused by wire bonding processes, enabling a thinner insulation layer (30 nm Al_2O_3) underneath the heater line required for reliable thermal measurements. (b) SEM image (top view) of the device. During the 3**ω** measurements, a current ($I(\boldsymbol{\omega})$) is applied across two electrodes while the 3rd harmonic voltage ($V(3\boldsymbol{\omega})$) is measured between the other two electrodes.

2.3.3 Measurement and data analysis

Thermal measurements using the 3ω technique are carried out on both pristine (reference) and ion damaged W in the temperature range of 300－370 K. The sample surfaces were first carefully and gently ultrasonic cleaned sequentially with acetone bath, isopropyl alcohol (IPA) bath and then DI water bath. Afterwards, any polymeric residue is removed with a mild oxygen plasma process.[93] To minimize the heat loss due to thermal convection, the improved 3ω measurements were conducted in a vacuum chamber. To accurately detect $V_{3\omega}$ (typically orders of magnitude smaller than $V_{1\omega}$), one matching

resistor with the same resistance was connected in series with the 3ω heater to cancel the $V_{1\omega}$ and other parasitic signals. We used a differential method to measure the thermal conductivity of the thin damaged layer: one on pristine W sample (hereafter named as 'reference') and the other with the heavy ion irradiation. The generalized 2D analysis[94] mentioned earlier was also applied to model the heat conduction process and extract the thermal conductivity from the measured data.[38, 95]

The measured T_{rise} as a function of the modulated frequency in the reference sample, as well as the fitting result, is shown in Figure 2.4. The measured κ of the reference substrate and the Al_2O_3 film were 182.0 ± 8.3 W/m·K and 1.2 W/m·K, respectively, at 300 K, which is consistent with prior measurements,[96-98] as well as published data from NIST,[96] consolidating the reference samples we used here has negligible intrinsic defects that might induce extra influence on thermal conductivity of ion implanted samples. The uncertainties in 3ω measurement,[94] mainly comes from temperature measurement and the determination of the temperature coefficient of resistance (TCR) of the heaters. The uncertainty from the damaged layer thickness is not included. The fitted κ of the reference substrate and the Al_2O_3 film were then used in the same 2D model to fit the measured T_{rise} from the irradiated sample, with the κ of the ion damaged layer as the only fitting parameter (Figure 2.4).

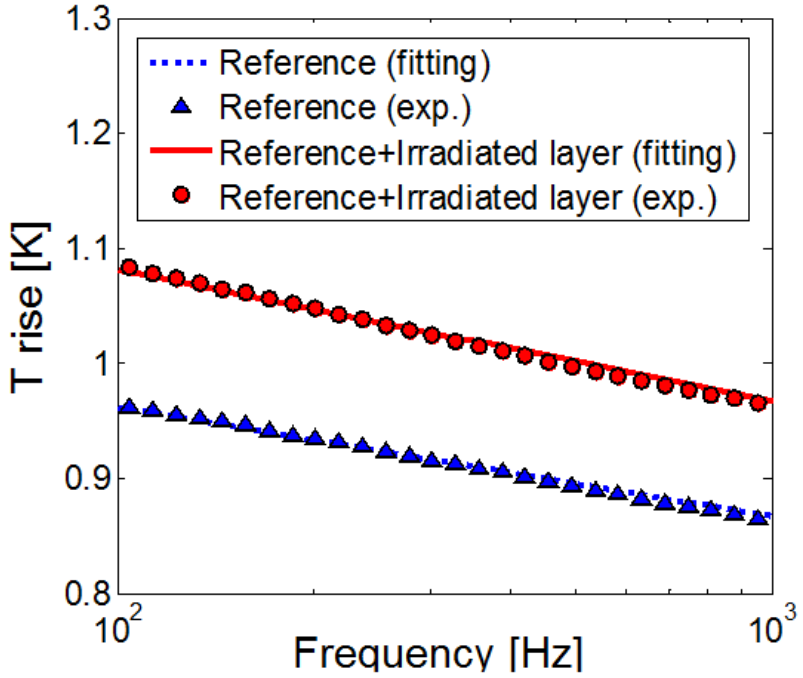

Figure 2.4. Measured temperature rise (T_{rise}) with fitting results from a 2D heat conduction model of the pristine W sample (reference) and the W sample irradiated by Cu^{2+} ions (0.6 dpa) at 300 K.

2.4 Surface morphology of heavy ion irradiated W

The scanning electron microscopy (SEM) image on the top surface of the heavy-ion damaged W and the reference sample were shown in Figure 2.5. No obvious micro-structure change at micrometer level, including the grain size, was observed in both room temperature irradiated W from 10^{-3} to 0.6 dpa and high-temperature irradiated W at 0.2 dpa. This indicates that any changes in thermal conductivity we might observe in the irradiated samples could be attributed to atomic and nanoscale defects, rather than damages at larger length scale. Indeed, it was shown that the dislocation loops and voids formed during the ion implantation are nanometers in size, which are extremely challenging to directly observe.[99] Thermal conductivity characterization, however, provides an indirect and yet

sensitive probe to gauge these atomic and nanometer scale defects,[100-101] as both types of heat carriers (electrons and phonons) are sensitive to scattering by defects.

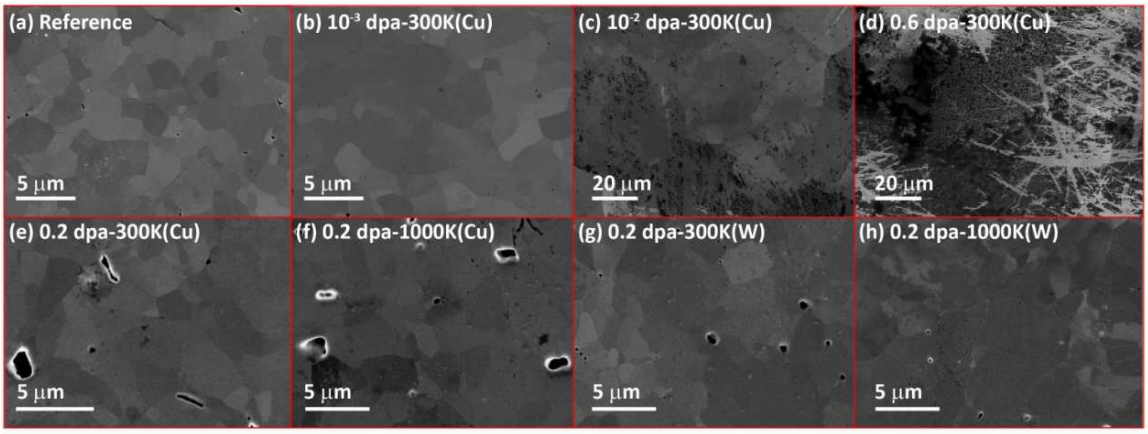

Figure 2.5. The top surface SEM of non-damaged W (reference) and heavy ion (Cu or W ion) damaged W from 10^{-3}, 10^{-2}, 0.2 and 0.6 dpa (300 K) and 0.2 dpa (1000 K).

2.5 Thermal conductivity of heavy ion irradiated W

2.5.1 The effect of damage level on thermal conductivity

We first examine the impact of dosage on κ of samples irradiated by Cu ions at room temperature. Figure 2.6 shows the measured room temperature κ values as a function of Cu ion dosage. A low κ, 123 ± 47.9 W/m·K, is observed even at 10^{-3} dpa, which corresponds to the fine vacancy clusters formation observed at low fluence room temperature radiation.[102] As the irradiation dosage increases, κ continues decreasing, reaching values of 82 ± 33.3 W/m·K at 10^{-2} dpa, 61 ± 14.7 W/m·K at 0.2 dpa, and 52 ± 13.6 W/m·K at 0.6 dpa. The κ of the W irradiated at room temperature likely saturates at around 60 W/m·K at 0.2 dpa, considering the relative large measurement uncertainty and the previously inferred defect saturation seen in deuterium retention studies.[103] The significant reduction in κ is likely a result of defects, such as SIAs, vacancies and voids,[104]

produced during heavy ion irradiation,[105] that have been observed under similar ion implantation conditions directly by Hassanein *et al*.[106] using TEM, as well as indirectly by Barton *et al*.[107] based on increased deuterium retention. These displacements damage products act as scattering sites to heat carriers, primarily electrons and with a small contribution from phonons,[108] thus reducing the κ. Those studies show substantial defect densities in W irradiated at room temperature at similar irradiation dosage. Saturation of the deuterium retention in ion beam damaged W has also been observed at a similar level of damage,[103] which corresponds to the saturation of thermal conductivity reduction at 0.2 dpa.

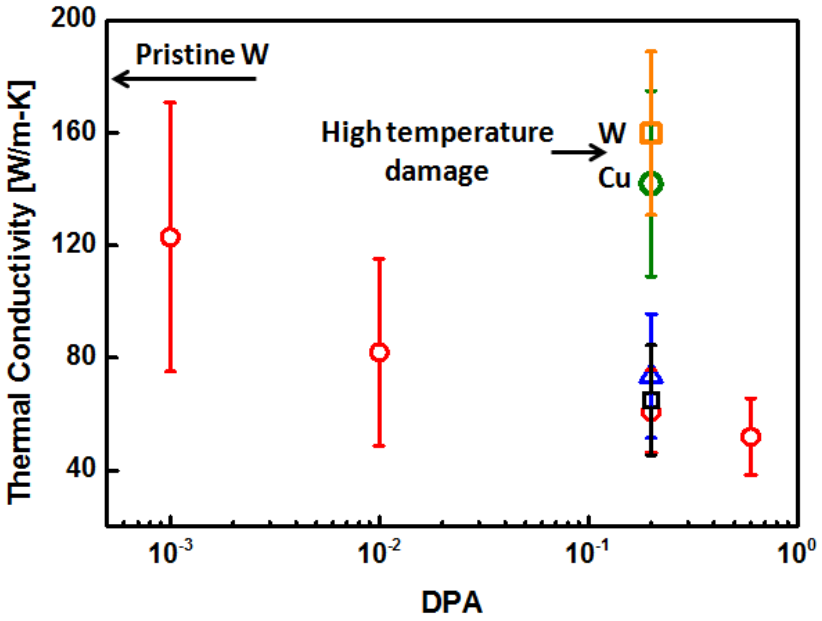

Figure 2.6. Thermal conductivity of damaged zone in W as measured by 3**ω** technique at room temperature. Red hollow circles represent Cu ion irradiated W samples at room temperature and green hollow circles represent Cu ion irradiated W sample at 1000 K. Black hollow square and orange hollow square represent W ion irradiated W samples at room temperature and 1000 K, respectively. The blue triangle is from Ref. [24] (Cu ion, irradiated at 0.2 dpa). The arrow shows the pristine W value (182 W/m·K). The error bar represents uncertainties in the measurements, mainly coming from temperature measurement and the determination of the temperature coefficient of resistance (TCR) of the heaters. The uncertainty from the damaged layer thickness is not included.

2.5.2 The effect of damage temperature and ion species on thermal conductivity

We then study the impact of elevated temperature on κ of irradiated W by damaging samples at 1000 K (concurrent heavy ion irradiation at elevated temperature, referred as dynamic annealing here) followed by thermal conductivity measurements. As shown in Figure 2.6, at the sample damage level of 0.2 dpa, dynamic annealing of the irradiated W shows a higher κ compared to the samples irradiated at room temperature. This indicates that κ is significantly recovered by this dynamic annealing, reaching values of up to 80% of the pristine W value. This recovery in κ is due to the reduction in remaining irradiation defect, such as dislocation loops, SIAs and vacancies, concentration discussed in Ref. [66], after high temperature dynamic annealing. The remaining 20% reduction in κ during dynamic annealing comes from the left-over defects that cannot be completely removed at 1000 K but might get fully removed away at 1673 K.[66] We also observed no difference in the κ behavior between samples irradiated by W or Cu ions, in neither the original κ reduction in the room-temperature samples nor the κ recovery in the annealed samples within the measurement uncertainty. This suggests that it is the defects induced by the ion irradiation (e.g., vacancy and vacancy clusters), not the implanted ion species themselves, that contribute to the original κ reduction. This observation is also consistent with a deuterium retention study on dynamically annealed and irradiated W, which shows a similar annihilation of deuterium trapping defects, and consequently a low deuterium retention level in samples irradiated at elevated temperature (573－1243 K) comparable to that in pristine W.[85] This recovery phenomenon can be understood from the SIA mobility, which is thermally activated with an activation energy of 0.1 eV.[109] At elevated temperature

(1000 K corresponds to an energy of ~90 meV), mobile SIA will have a higher probability to recombine with vacancies or free surface. Neglecting transmutation, our results show that a significant amount of displacement damage from neutrons may be annealed out provided the wall/divertor armor is held at a sufficiently high temperature.

Figure 2.7 shows the κ of the ion irradiated W layers as a function of measurement temperature of the sample, as well as the reference (non-irradiated W). The κ of reference sample agrees well with the published data from NIST within the measurement range. In pristine W, as electrons are the main heat carriers, the thermal conductivity can be approximated from the Wiedemann－Franz law,

$$\kappa_{\mathrm{e}} = L\sigma T \quad (2.7)$$

where L is the Lorentz number and σ is electrical conductivity.[110] Therefore, as temperature increases in pristine W, electron-phonon scattering rate also increases, which led to a decreasing κ with temperature. However, the temperature dependence of κ of damaged W is altered as defects are introduced during the displacement damage. The κ of the room-temperature irradiated W samples with large displacement damage (0.2 dpa and 0.6 dpa) increase from 300 to 370 K, which suggests impurity scattering mechanism starts to dominate phonon scattering because defect scattering is mainly influenced by the size, mass, and density of defects/impurities, but not temperature. On the other hand, for the room-temperature irradiated W samples with low irradiation dosage (10^{-3} dpa and 10^{-2} dpa), κ of the damaged layer is relatively constant or slightly decreased with increased sample temperature because the phonon scattering is still more dominant than the impurity scattering due to the lower defect concentration. For the W samples irradiated at high temperature (1000 K), the temperature dependence is more similar to that of the low dosage

samples irradiated at room temperature. This observation further confirms the lower impurity concentration in the annealed samples at 1000 K due to the annihilation of the defects.

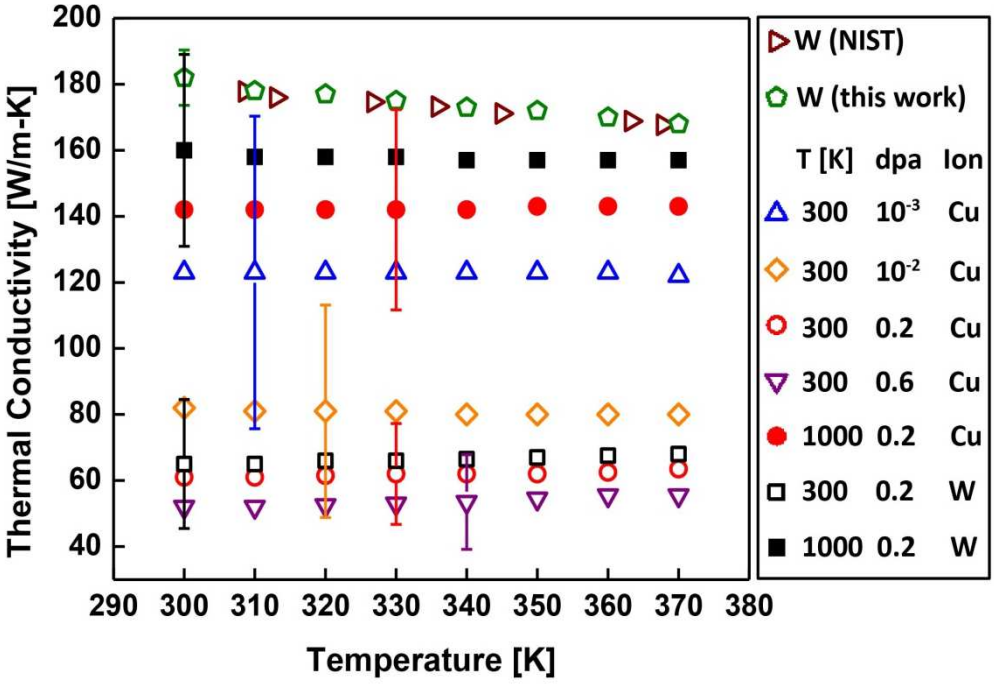

Figure 2.7. Thermal conductivity of pristine W and ion damaged W layer from 300 K to 370 K, along with the standard value of W published by NIST. Hollow symbols represent the reference sample, NIST data, and the ion irradiated W at 300 K. Filled symbols represent ion irradiated W at 1000 K. The error bars are determined as in Figure 2.6. For each sample, the error bars are similar within the entire measurement temperature range, and only one representative error bar for each condition is shown.

2.6 Conclusions

In summary, we study the impact of heavy ion implantation dosage and temperature on thermal conductivity of W through thermal characterization using the improved 3ω technique. A decreasing thermal conductivity with increasing ion implantation dosage was observed for samples irradiated at room temperature, which can be attributed to the defects,

such as SIAs, vacancies and voids, induced by the ion irradiation. This thermal conductivity is saturated at approximately 60 W/m·K, or about 30% of the pristine W value, when the damage level is above 0.2 dpa. Samples irradiated at an elevated temperature (1000 K) show a recovery of thermal conductivity to approximately 80% of the pristine W value. This strong recovery suggests the annihilation of the irradiation induced defects, such as SIAs and vacancies through recombination, by the high temperature annealing. Our studies suggest that there may be an optimal temperature window that limits the damage induced by irradiation on the thermal and deuterium retention properties of W.

Chapter 2, in part, is a reprint of the material as it appears in Journal of Nuclear Materials, 2017. Shuang Cui, Michael J. Simmonds, Wenjing Qin, Feng Ren, George R. Tynan, Russell P. Doerner, Renkun Chen. The dissertation author was the primary investigator of this paper. Also, it, in part, is in a manuscript under revision by Journal of Nuclear Materials. Shuang Cui, Russ P. Doerner, Michael J. Simmonds, Chuan Xu, Yongqiang Wang, Edward Dechaumphai, Engang Fu, George R. Tynan, Renkun Chen. The dissertation author was the primary investigator and the first author of these papers.

3 Chapter 3 Thermal Transport in He-plasma irradiated tungsten

3.1 Introduction

Tungsten (W) is considered a promising plasma facing material (PFM) for ITER because of its high melting temperature, high thermal conductivity, high sputtering threshold energy, and low sputtering erosion yield.[16] The near-surface region of PFM is exposed to both steady and transient heat loads, suffering from bombardment of large flux (10^{22}－10^{24} $m^{-2}\cdot s^{-1}$)[111-112] and low-energy (tens of eV to hundreds of eV) of helium (He) plasma as well as hydrogen isotopes (H,D,T) plasmas.[113-115] As a result, exposed surfaces exhibit nanostructured surface morphology under certain irradiation conditions.[116-118] He holes/bubbles,[119-121] fibreform,[116-117] and fuzz nanostructures[115, 122-124] induced by the particle bombardment could in turn modify thermo-mechanical properties of the material such as the thermal conductivity and mechanical strength, and ultimately impact the performance of PFM such as the surface temperature and erosion yield. It has been pointed out that the plasma-induced damage may cause a drastic decrease in optical reflectivity[125] and several orders of magnitude reduction in thermal conductivity based on indirect measurement combined with a heat transfer model.[126] The reduced thermal conductivity of the near surface region could lead to a larger surface temperature rise on the PFM under heat loads, especially the transient loads to be expected in ITER, such as edge localized modes (ELMs)[21-22] (0.2–2.0 MJ/m^2 with a duration of 0.1－1 ms[127]) and disruption (several tens of MJ/m^2 with ~10 ms period[126]). In fact, we have shown in our prior publication[24] that the temperature rise across a thicker (~10 μm) damaged layer would be significant

even with a moderate thermal conductivity reduction. In addition to the direct temperature rise caused by the reduced thermal conductivity in the damaged layer, the lower thermal conductivity also leads to a larger temperature gradient in the near surface regime of PFMs, resulting in larger thermal stress that could cause the material failure via delamination or cracking, as discussed in Ref. [17-19], which also needs to be taken into account in the thermal design of future plasma-facing components (PFCs). Therefore, it is of great interest to directly quantify the thermal conductivity of the near-surface damaged layer upon He-plasma exposure for a better understanding of the impact of plasma irradiation on structures and thermal conductivity.

One of the challenges associated with the direct thermal conductivity measurements on the near-surface damaged region lies in the extremely shallow damaged layers due to He-plasma irradiation (usually about tens of nanometer thick). In this work, we developed independent techniques for bulk and thin film W to tackle this measurement challenge. First, to measure the thermal conductivity of the near-surface damaged layers in bulk W, we improved the measurement sensitivity of the established 3ω technique by employing novel fabrication techniques. Second, we directly used W thin films fabricated by magnetron sputtering and studied the effect on thermal conductivity of He-plasma irradiation.

3.2 Preparation of He-plasma irradiated W

3.2.1 He-plasma irradiated bulk W prepared in PISCES-A

ITER grade W[128] disks of 6 mm in diameter and 2 mm in thickness were used as the model material for PFM. Discs were electropolished to a mirror finish, cleaned in acetone, followed by ultrasonic cleaning in an ethanol bath, and finally annealed at 1273

K for 1 hour to reduce the amounts of intrinsic defects. The samples were then exposed to pure He plasma in the PISCES-A linear-divertor-plasma simulator at UCSD.[129] During the plasma exposure, sample temperature was monitored with a thermocouple attached firmly against the back surface of the sample. Plasma conditions were measured using a reciprocating Langmuir probe. The duration of the plasma exposure was 2000 s. The plasma conditions were T_e ~7 eV, n_e ~6×10^{18} m^{-3}, for a total fluence of 1×10^{26} m^{-2}. The incident ion energy of 60 eV was achieved by applying a negative bias to the sample manipulator. The sample temperature of 773 K was maintained throughout the exposure by adjusting the air cooling rate to the sample manipulator. The surface morphology of W disk was examined using a scanning electron microscope (SEM) before and after He plasma exposure, as shown in Figure 3.1.

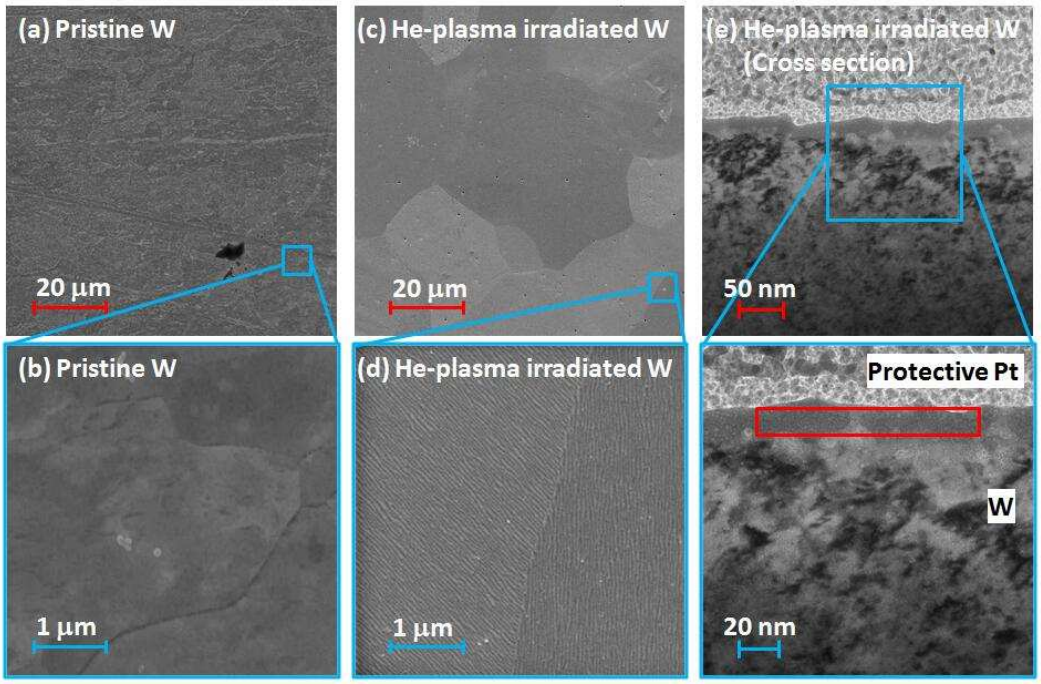

Figure 3.1. (a, b) SEM images of W targets before exposure to He plasma. (c, d) SEM images of W targets after exposure to He plasma at 773 K for exposure time of 2000 s. (e) Cross sectional TEM of exposed W target. The thickness of altered morphology layer is ~20 nm between the protective Pt layer and bulk W substrate.

3.2.2 He-plasma irradiated W thin film prepared in PISCES-E

A W thin film with a thickness of 50 nm was deposited onto a glass substrate 2.54 cm in diameter using a sputtering system (ULVAC, ACS-4000-C4) from a 99.95% pure W target with the power of 150 W at 873 K. The base pressure of the chamber prior to deposition was 6.9×10^{-6} Pa, which has already been applied to obtain W thin film with low resistivity (about twice of the bulk value).[130] The sputtering gas was 99.999% pure Ar gas. The sputtering pressure was 5.1 Pa and the Ar flow rate was 20 sccm. By measuring the thickness and the total deposition time, the deposition rate was calculated to be 0.12 nm/s. The density of W thin film was measured to be 17.46 g/cm^3, ~9% lower than that of bulk W. The W film was then exposed to He plasma utilizing a 13.6 MHz RF source with a flux of ~3.6×10^{20} m^{-2}·s^{-1} up to a fluence of 2×10^{24} m^{-2} in the PISCES-E plasma simulator[131] at UCSD. During the exposure, the target was biased to -60 eV to facilitate energetic ion bombardment and reached a peak temperature of ~438 K as measured via a thermocouple. Similarly, the surface morphology of W thin film was examined by SEM before and after the He plasma exposure, as shown in Figure 3.2.

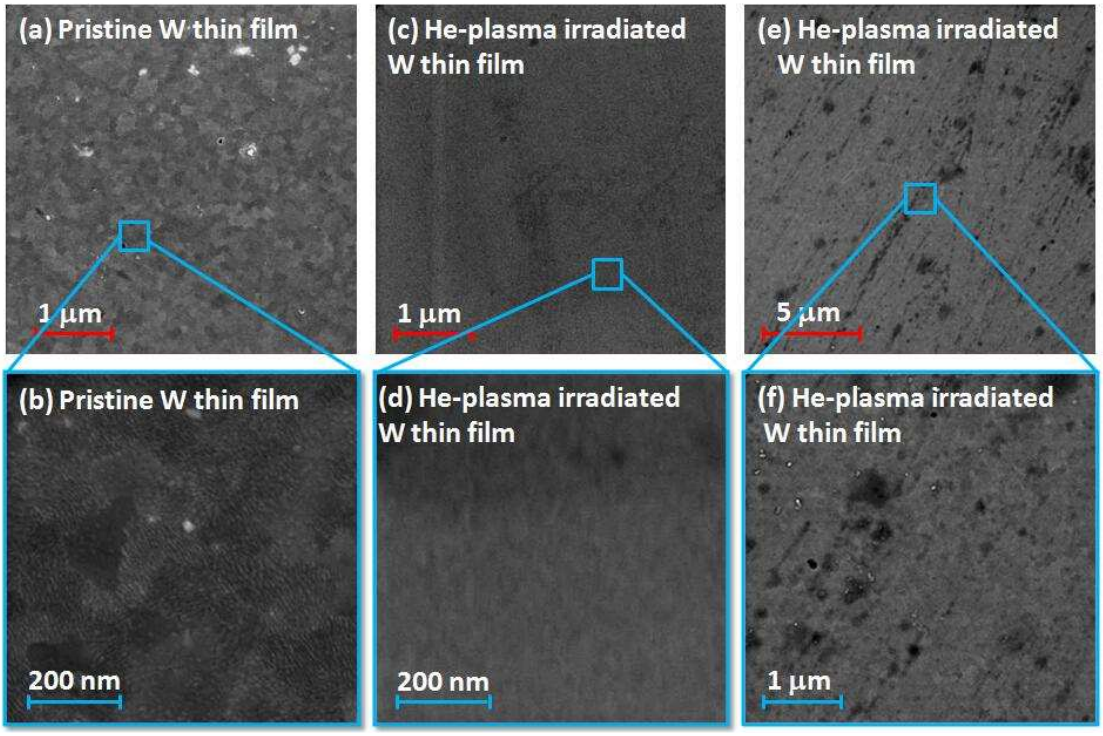

Figure 3.2. (a, b) SEM images of W thin film (~ 50 nm) before He plasma exposure. (c, d) SEM images of the same W thin film after exposed to He plasma utilizing a 13.6 MHz RF source. (e, f) Edges of the exposed W thin film covered with a mask during the He-exposure (hence was not exposed to He). No obvious morphology change was observed.

3.3 Surface morphology of He-plasma irradiated W

3.3.1 Surface morphology of bulk W after He-plasma irradiation

The surface morphology of bulk W was examined using a scanning electron microscope (SEM) before and after He plasma exposure, as shown in Figure 3.1(a) and (b) and Figure 3.1(c) and (d), respectively. The thickness of the altered structure layer was measured to be ~20 nm using transmission electron microscopy (TEM) on the cross section of the bulk W exposed to He plasma at 773 K for 2000 s (Figure 3.1(e)). The effect of the He plasma was found to induce a dramatic change in the surface morphology. The flat surface (Figure 3.1(b)) became rougher, featured with fringe patterns with distinct

orientations within each grain (Figure 3.1(d)). The mechanism leading to the W surface morphology change is presumably due to the near-surface He trapping at defect sites.[124] The formation mechanisms could consist of the following processes: (i) penetration of incident He atoms into W; (ii) diffusion of He atoms and their trapping at thermal vacancies; and (iii) formation and aggregation of He bubbles.[118, 132] Wave-like microstructures and nano-fuzz or voids have been observed when the incident He ion energy was higher than ~30 eV and the surface temperature ranged from 1000 to 2000 K.[38, 118] While a rough structure appeared on the surface (Figure 3.1(d)), neither pinhole nor fibrous structure were observed on the surface when the surface temperature was lower than 1000 K[118] (our exposure temperature was 773 K).

3.3.2 Surface morphology of thin film W after He-plasma irradiation

The surface morphology of the 50 nm thick W thin film was also altered after exposure to He plasma in PISCES-E with a surface temperature of 438 K for 5560 s. During the experiment, the edge of the W thin film was covered with a mask holder and hence was not exposed to the plasma. As expected, the unexposed edge of the W thin film after the exposure experiment exhibited a similar surface morphology (Figures 3.2(e) and (f)) as before the plasma exposure (Figures 3.2(a) and (b)). However, for the inner area of the sample that was exposed to the He plasma, the surface showed a drastically different morphology after plasma exposure, as evidenced by a flatter and feature-less surface (Figures 3.2(c) and (d)). This morphology change in the irradiated W thin film might also originate from the penetration of the He atom into the film, as in the case of the W bulk samples discussed earlier. The different morphologies of W bulk and thin film before

exposure to He plasma might come from the different crystalline forms and the grain sizes. W bulk usually has α-phase structure while W thin film has both metastable β-phase and α-phase structure owing to non-equilibrium synthesis or stabilization by impurities. Even the β-W could easily transforms to α-W thin films[133] under room temperature, both crystalline forms might coexist. Also, the smaller grain size in W thin film compared to W bulk[130] might also lead to a different morphology.

3.4 Thermal measurement of He-plasma irradiated W

3.4.1 Thermal measurement of bulk W

Compared to the ion irradiated W samples we measured previously,[24, 81] He-plasma irradiated layers prepared using PISCES-A are much thinner (measured to be ~20 nm in thickness, as shown in Figure 3.1(e)). We, therefore, utilize the 3ω measurement with higher measurement sensitivity by additional nanofabrication steps, as discussed in section 2.3.2. A thinner insulation layer of 30 nm thick Al_2O_3 was deposited on the sample surface. A defined and patterned narrow groves in the Parylene layer to allow the heater strips to be deposited directly on top of the thin Al_2O_3 layer (Figure 3.3(b)), while the four large contact pads was deposited to the 600 nm thick Parylene layer to further ensure electrical insulation between the contact pads and the W substrates. Compared to the traditional design of 3ω device in Figure 3.3(a), the measurement sensitivity is improved by thinning down the insulation layer thickness by half since with thicker Parylene layer to insulate larger area of contact pads (Figure 3.3(b)), which is the main source of electrical current leakage.

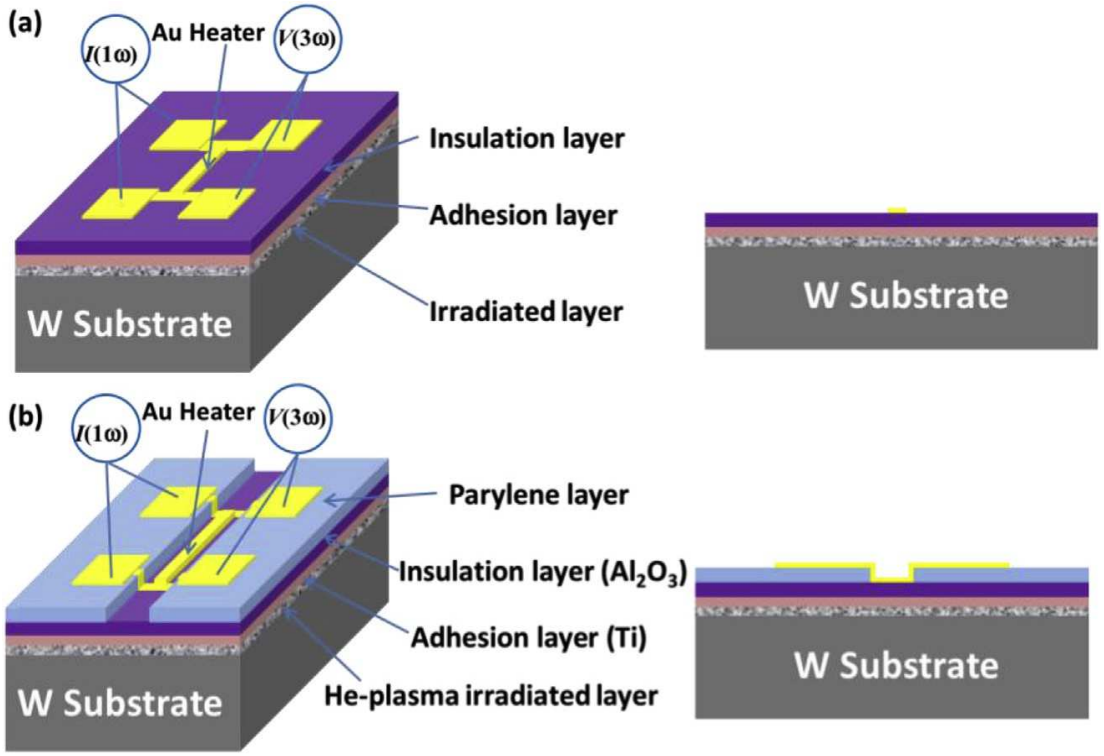

Figure 3.3. (a) Schematic diagram of a typical 3ω device for thermal measurement of damaged layer (1μm in thickness by Cu^{2+} ion irradiation in Ref. [24]). An insulation layer is deposited to prevent electrical leakage between the Au heater and the W sample. (b) Adopted 3ω device in this work with improved measurement sensitivity by involving one additional protective layer for large contact pads (600 nm thick Parylene) to decrease the thickness of the insulation layer underneath the 3ω heater line.

3.4.2 Thermal measurement of thin film W

We used the van der Pauw method, a well established method of determining the electrical conductivity of thin films, to measure electronic thermal conductivity of the sputtered W thin film before and after the He-plasma irradiation.[134-135] The measured electrical conductivity (σ) is then related to electronic thermal conductivity (κ_e) via the Wiedemann-Franz law (W-F law), which is the ratio of the electronic contribution of the thermal conductivity (κ) to the electrical conductivity (σ) of a metal, and is proportional to the temperature. This approach is valid because electronic thermal conductivity is the

dominant part of the total thermal conductivity in W (the lattice contribution is less than 16.3 W/m·K calculated in Ref. [136] in bulk W, ~10% of electron contribution). In order to carry out the van der Pauw measurements, the structure must be of negligible and uniform thickness (as compared to the lateral dimension of the structure), be homogenous in composition and be symmetrical. More importantly, the area of the contacts on the circumference of the structure must be sufficiently small compared to the area of the sample. Our sample geometry (Figure 3.4(a)) met all these criteria.

The electrical configuration of the traditional van der Pauw method is shown in Figure 3.4(a), with four contacts labelled 1, 2, 3 and 4 placed 2 mm away from the perimeter of the W thin film (2.54 cm in diameter) symmetrically. The measurements were done with a probe station using W needles for electrical contacts (Figure 3.4(b)), which ensured the small contact areas needed for the van der Pauw method. Resistance $R_{12,\,34} = V_{34} / I_{12}$, is defined where V_{34} is the potential difference between contacts 3 and 4 when a current I_{12} is passed through the contacts 1 and 2. Van der Pauw[134-135] derived the general relationship between the resistances measured when the voltage contacts and the current contacts are interchanged,

$$e^{-\pi R_{12,34}/R_s} + e^{-\pi R_{23,41}/R_s} = 1 \quad (3.1)$$

where R_s is the sheet resistance of the sample. The electrical resistivity (σ) could be determined as $\rho = R_s \times d$ where d is the W thin film thickness (~50 nm here). The electronic contribution to the thermal conductivity of W thin films was then calculated based on the W-F law,

$$\frac{\kappa_e}{\sigma} = LT \quad (3.2)$$

where κ_e is the electronic thermal conductivity, σ is the electrical conductivity of

the thin film, L is the Lorenz number, and T is the absolute temperature. Sommerfeld theory suggests that L should be constant for all metals at the same temperature, and leads to the well-known value, $L = \frac{\kappa}{\sigma T} = \frac{\pi^2}{3}\left(\frac{k_B}{e}\right)^2 = 2.44 \times 10^{-8}\, W\Omega/K^2$,[137] where e is the elementary charge and k_B is Boltzmann's constant.

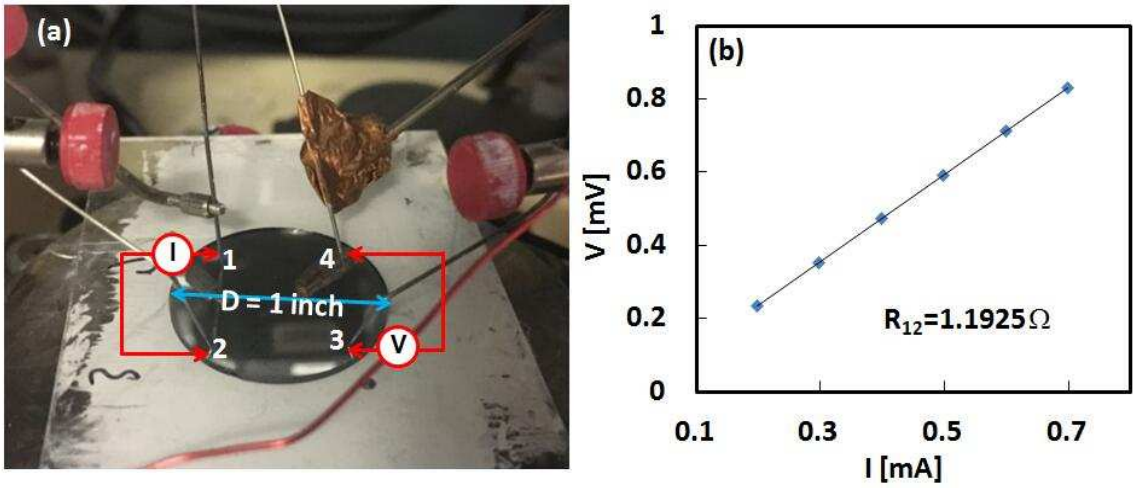

Figure 3.4. (a) The electrical configuration schematic of van der Pauw measurement with four contacts labelled 1, 2, 3 and 4 placed 2 mm away from the perimeter of the W thin film (1 inch in diameter, 50 nm in thickness). Sheet resistance was measured in W thin film before and after He-plasma irradiation in a probe station with W needles ensuring micron-sized contact areas. (b) Measured I-V curve used to determine sheet resistance using the van der Pauw method.

3.5 Thermal conductivity of He-plasma irradiated W

3.5.1 Thermal conductivity of bulk W after He-plasma irradiation

The reference sample was first measured to obtain the thermal conductivity of the W substrate and the Al_2O_3 insulation layer by fitting the measured T_{rise} to the 2D heat conduction model.[24] The measured T_{rise} vs. modulated frequency of the reference sample, as well as the fitting result, is shown in Figure 3.5. Two W references are measured here, and fitting results for the thermal conductivity of the W reference #1, W reference #2 and

Al_2O_3 insulation layer were 179 ± 3.2 W/m·K, 190 ± 3.2 W/m·K, and 1.2 W/m·K, respectively, at 300K. These parameters were then used in the same 2D model to fit the measured T_{rise} from the irradiated sample), with the only fitting parameter being the thermal conductivity of the thin He-plasma irradiated layer. The large uncertainty in determining the thermal conductivity by this method mainly originated from the small temperature drop (~0.09 K) across the much thinner irradiated layer between the reference and irradiated samples (~20 nm in thickness, Figure 3.1(e)).

The κ of the pristine W sample was measured by the improved 3ω method and the values agree very well with the published data from NIST within the measured temperature range,[138] thus validating the measurement technique. The κ of the He-plasma irradiated bulk W sample fitting to two different reference W sample 1 and sample 2, measured within the same temperature range as that of the reference W, are plotted in Figure 3.6. The large error in the He-plasma irradiated bulk W samples comes from extremely thin thickness of the irradiated region. The thermal conductivity of the He-plasma irradiated layer is reduced to below 20 W/m·K, or about one order of magnitude lower than that of pristine W (~179 ± 3.2 W/m·K at 300K). This large reduction in thermal conductivity can be attributed to the defects formed during He plasma bombardment, as discussed in Figures 3.1(c) and (d). Those defects serve as the scattering centers for electrons, the dominant heat carriers in W, thus reducing the thermal conductivity of the irradiated layer. Additionally, the relatively temperature independent thermal conductivity of the irradiated W layers (Figure 3.6) also suggests that the impurities scattering plays a significant role in thermal (and carrier) transport.

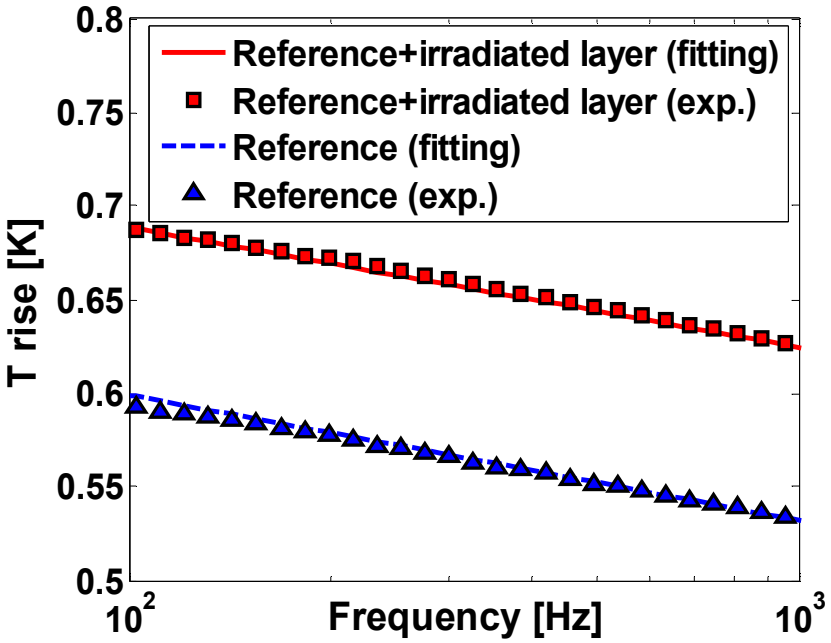

Figure 3.5. Experimental temperature rise with fitted results from a 2D heat conduction model of the pristine (Reference) and He-plasma irradiated bulk W. The blue triangles and dashed line represent the experimental T_{rise} and 2D fitting for the reference sample with the thermal conductivity values of the insulation layer and the W substrate applicable to model T_{rise} of the irradiated sample (red solid line) by fitting the measured data (red squares).

3.5.2 Thermal conductivity of thin film W after He-plasma irradiation

Similar to irradiated bulk W, a lower thermal conductivity was also observed in sputtered W thin films after He-plasma irradiation in Figure 3.6. The in-plane electrical resistivity of the 50 nm thick W thin film extracted before and after the He-plasma irradiation by Van der Pauw method was 0.29 ± 0.01 $\mu\Omega \cdot m$ and 1.35 ± 0.03 $\mu\Omega \cdot m$, respectively. The uncertainty was determined based on the distance between the four contacts and the edge of the sample (~2 mm), as in Ref. [135]. The possible reasons for the slightly higher resistivity of the W thin film compared to that of bulk W (0.053 $\mu\Omega \cdot m$ [41]) include: [i] the presence of β-W with bulk resistivity in the range of 1.5-3.5 $\mu\Omega \cdot m$; [ii] the incorporation of impurities from the source material or during the sputtering process; [iii]

the presence of surfaces and grain boundaries.

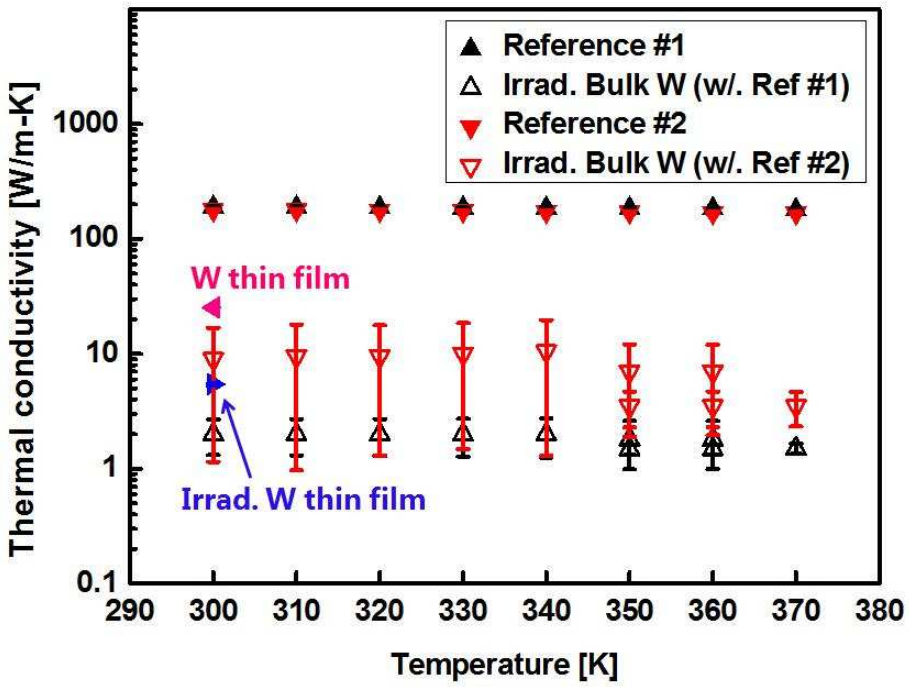

Figure 3.6. Thermal conductivity of pristine W and He plasma damaged W layer in bulk W, along with that of thin film before and after irradiation. The error bar represents uncertainties in the measurements, mainly coming from temperature measurement and the determination of the temperature coefficient of resistance (TCR) of the heaters. The uncertainty from the damaged layer thickness is not included. The thermal conductivity of the damaged film is at least one order of magnitude lower than that of pristine bulk W, and is nearly temperature independent, suggesting the effect of defects introduced during He plasma bombardment.

From the measured electrical resistivity of the W film before and after the He plasma exposure, the electronic thermal conductivity of the W thin film, as determined via the W-F law with Lorenz number of $2.44 \times 10^{-8}\ W\Omega/K^2$,[137] was reduced from 25.2 ± 0.13 W/m·K to 5.44 ± 0.14 W/m·K (~78% deduction) after the plasma exposure. Therefore, at least an ~80% reduction in thermal conductivity at room temperature was observed for both of bulk and thin film W, as shown in Table 3.1, even though the W thin film has a

higher initial defect concentration prior to He plasma exposure. This significantly suppressed thermal conductivity in W needs to be considered in the thermal design of future PFMs.

Table 3.1. Comparison between electronic thermal conductivity (Irrad. W thin film) converted from the W-F law with sheet resistance measured by the van der Pauw method and thermal conductivity (Irrad. bulk W) by 3**ω** measurement. At least an approximately 80% reduction in the thermal conductivity is obtained for the two types of samples.

	W bulk	**W thin film**
Equipment	PISCES-A	PISCES-E
Fluence	1×10^{26} m^{-2}	2×10^{24} m^{-2}
Temperature	500°C	165°C
Method	3ω	W-F law
Density	19.26 g/cm^3	17.46 g/cm^3
κ_before Irrad.	179 W/m·K	25.2 W/m·K
κ_after Irrad.	<20 W/m·K	5.4 W/m·K
Defects concentration before Irrad.	n_o	$7n_o$
κ reduction after Irrad.	88%	78%

3.6 Conclusions

In this work, we used an improved 3 ω method with increased measurement sensitivity to measure the thermal conductivity of the thin damaged region in W after He-plasma irradiation. The measured thermal conductivity of the ~20 nm thick irradiated layer shows at least one order of magnitude reduction compared to non-irradiated pristine W. Similarly, He plasma bombardment was also applied to a sputter-deposited W thin film, which caused an approximately 80% reduction in thermal conductivity of the film. The reduction in the near-surface thermal conductivity is believed to be contributed by defects induced in the irradiation process and may have impacts for thermal management of PFMs. Therefore, this work suggests that suppressed thermal conductivity and the effects on the

thermo-mechanical behaviours in PFMs needs to be considered in the thermal design of future nuclear fusion reactors.

Chapter 3, in part, is a reprint of the material as it appears in Journal of Nuclear Materials, 2017. Shuang Cui, Michael J. Simmonds, Wenjing Qin, Feng Ren, George R. Tynan, Russell P. Doerner, Renkun Chen. The dissertation author was the primary investigator of this paper.

4 Chapter 4 Superabsorbent and tough hydrogels for building cooling

4.1 Introduction

In most countries, residential and commercial buildings are one of the highest energy consumption sectors. In the United States in particular, over 40% of energy consumption and greenhouse gas emissions are related to building temperature regulation.[139] Notably, building energy consumption is still increasing at a rate of 0.5－5% annually in developed countries[140] and is expected to increase even more rapidly in developing countries. Therefore, alternative building thermal regulation technologies, based on passive systems, have been extensively studied over past decade,[141-143] such as night-time ventilation in moderate or cold climate,[46-47] high infrared (IR) reflective coatings for reducing energy uptake,[48-49] and phase change materials (PCMs) for thermal energy storage.[144-146] Nevertheless, no current passive cooling technologies used in buildings possess ideal characteristics such as high cooling efficiency under a variety of weather conditions, high durability including resistance to thermal cycling and UV irradiation, and low cost. For example, PCMs are less effective under high solar intensity fluctuations due to their low latent heat (~hundreds of kJ/kg). More efficient and durable cooling materials and systems are needed for sustainable building cooling.

In nature, plants and animals are autonomously adaptive to increases in environmental temperature through transpiration and perspiration of water, which has one of the highest latent heats among fluids. Inspired by such passive biological cooling processes, several self-adaptive technologies involving bio-inspired artificial skins have been reported.[147-151] One of the more promising materials is based on superabsorbent

polymers, or hydrogels, which can contain more than ~90 wt% water in their fully swollen state.[152-153] These swollen hydrogels can be applied to the roofs of buildings,[154] acting as artificial 'skins' to provide cooling. By applying hydrogel coatings, heat dissipation is enhanced through the evaporation of water inside the hydrogel, enabling surface temperature reductions of 10-30°C in various objects, such as skin,[155-156] handheld electronics,[157-159] Li-ion battery packages,[160-161] and buildings. This remarkable autonomous cooling capability makes hydrogels an attractive candidate for energy-efficient building cooling.

Importantly, hydrogels previously investigated for cooling applications have not yet demonstrated one key feature required to truly mimic biological skins: durability and reusability for repeatable cooling. Only limited regeneration capability tests have been performed on hydrogels for cooling applications.[160-162] The maximum cycling number demonstrated so far is about six, which is far below the amount needed for practical cooling applications. Hydrogels utilized for bio-inspired cooling so far are often brittle, as measured by low fracture energies (~10 J/m^2),[163] which is orders of magnitude lower than that of human skin (~1,800 J/m^2).[164] These poor mechanical properties (low stretchability and toughness) severely limit the scope of cooling applications for hydrogels, where reusable and regenerable cooling is important for both long-term performance and cost-effectiveness. For example, embedding hydrogels inside roofing[162] makes it unfeasible to replace the gels after only a few cycles. Furthermore, degradation and aging of hydrogels *via* UV radiation hinders outdoor applications,[165-167] such as for coating windows or building facades.

In this work, we report, for the first time, the application of a highly stretchable and tough double network hydrogel (DN-Gel)[168-169] as a regenerable 'sweating skin' for cooling buildings. Compared with single network hydrogels (SN-Gels) used in previous cooling studies,[155-158, 161-162] DN-Gels have significantly higher fracture energy (~9,000 J/m^2),[170] comparable to that of animal skin.[171-172] While the toughness of DN-Gels is well established, their suitability for cyclic cooling or heating has not been studied. During the cooling process, the internal morphology (e.g., porosity) could change upon swelling/deswelling cycles, or the material may degrade after exposure to heat and UV radiation. Herein, we show that DN-Gels exhibit excellent evaporative cooling performance as well as extraordinary toughness and cyclability, as demonstrated by continual cooling performance over more than 50 cycles.

4.2 Materials preparation

4.2.1 Reagents and materials

The DN-Gel monomers, alginate (AG) and acrylamide (AAm) (99$^+$% electrophoresis grade) were purchased from FMC BioPolymer and Alfa Aesar, respectively. A crosslinker, N,N'-methylenebis (acrylamide) (MBAA) (> 98.0%) and calcium sulfate dehydrate (> 99%), crosslinking accelerator, N,N,N',N'-tetramethylethylenediamine (TEMED) (99%), and photoinitiator, ammonium persulfate (AP) (> 98.0%), were purchased from Sigma-Aldrich. The SN-Gel monomers, acrylic acid (AAc) (99.5%), and photoinitiator, 2,2-dimethoxy-2-phenylacetophenone (DMPA) (99%), were purchased from Alfa Aesar and Acros, respectively. All chemicals were used as received without any purification.

Table 4.1. Reagents for DN-Gel and SN-Gel synthesis.

Reagent	DN-Gel	SN-Gel
Monomer	alginate (AG) / acrylamide (AAm)	acrylic acid (AAc) / acrylamide (AAm)
Crosslinker	N,N'-methylenebis (acrylamide) (MBAA) / calcium sulfate	N,N'-methylenebis (acrylamide) (MBAA)
Crosslinking accelerator	N,N,N',N'-tetramethylethylenediamine (TEMED)	-
Photoinitiator	ammonium persulfate (AP)	2,2-dimethoxy-2-phenylacetophenone (DMPA)

4.2.2 Hydrogel preparation

To prepare DN-Gels, AG and AAm were dissolved in DI water with weight ratios of 2%, 12%, and 86%.[35] We then added 0.06 wt% MBAA, as a cross-linker to AAm, and 0.17 wt% AP, as a photoinitiator for AAm, to the solution. After degassing the solution in a vacuum chamber, we added 0.25 wt% TEMED, as a cross-linking accelerator to AAm, and 13 wt% calcium sulphate slurry, as an ionic cross-linker to AG, for homogeneous mixing using a syringe technique. The solution was poured into a plastic petri dish, cured with UV light (λ = 254 nm) for 1 hour at 50°C, and then left in a humid box for 24 hours to stabilize the reaction.

For SN-Gels, a photoinitiator solution was prepared from 0.1923 g of DMPA in 10.0 mL of DMSO.[173] The solution was sonicated until all the DMPA was dissolved, then covered and kept in the dark. A pre-polymer solution contained the monomers and cross-linking agent in a pH buffer solution with a molar ratio 7:3 of AAc to AAm and a 0.128 mol% crosslink density to the total monomer. The photoinitiator solution and the pre-polymer solution were homogeneously mixed *via* sonication for 1 hour. The solution was

then poured into a petri dish and polymerization was initiated by exposure to a UV lamp (λ = 365 nm) at room temperature for 10 minutes.

4.3 Experimental

4.3.1 Cooling experiments

To investigate the cooling performance and cyclability of tough DN-Gels, we conducted cooling experiments on miniaturized model houses under simulated solar irradiation (QL 1500 Series lamp) with a maximum power density of 1000 W/m^2. Two identical model houses made of oak wood (with thermal conductivity of 0.17 W/m·K, density of 740 kg/m^3, and thickness of 0.025 m), each with a roof surface area of 64 cm^2 (Figure 4.1((a)), were built to compare the cooling effectiveness of the DN-Gels and SN-Gels. Thermocouples were attached to the top and bottom surfaces of the roof panel on both model houses to monitor the temperature rise induced by simulated solar irradiation. To directly compare cooling performance, both types of hydrogel layers were soaked in deionized (DI) water for ~8 hours prior to attaching them to the model house roofs. An acrylic adhesive was used to ensure good thermal contact between the hydrogel layer and roof. A solar simulator was used to apply a normal incident irradiance of ~800 W/m^2 to both roofs. Similar experiments were conducted to test the cyclability of the DN-Gels and SN-Gels after reducing soaking and drying time to ~5 hours, and varying incident irradiance power (700 W/m^2 and 800 W/m^2). The thickness of the tough DN-Gel mats synthesized here is initially 1 cm but can reversibly expand up to 2 cm in the swollen state after storing up to 90 wt% water.[169-170, 173] We also synthesized a 0.8 cm thick SN-Gel (Poly (AAm-AAc)) according to a reported recipe.[173]

4.3.2 Mechanical test

Dog-bone shaped specimens were laser cut according to the ASTM D-412 standard for the freshly prepared and cycled DN-Gels (after 50 cycles) in both the dehydrated and swollen states. The tensile test was conducted using an Instron 5965 universal testing instrument with a strain rate of 0.02 s^{-1}. Nominal stress was defined as the ratio between the applied force and the initial cross-sectional area of the specimen, and stretch was defined as the ratio of the current and initial length of the specimen.

4.3.3 Swelling ratio test

Cubes of dry gels with sides measuring 0.5 cm were immersed in DI water at a relative humidity of ~50% at room temperature. The gels were continuously retrieved from the water and, after removing excess water from the cube surface, weighed, until the gels reached fully saturated states, indicated by no additional weight gain over 3 more weighing cycles. The Swelling Ratio (SR) was defined as the ratio of the gained weight of water inside the hydrogel to that of the initial dehydrated gel.[174-175]

4.4 Effective and regenerable cooling performance of DN-Gels

The house models covered with hydrogel layers, as shown in Figure 4.1(a), were built and subjected to simulated solar irradiation ranging from 700 to 800 W/m^2. Following Sun *et al*.,[170] DN-Gels were synthesized, with the chemical formula of the gel shown in Figure 4.1(b), which have two types of polymer networks, ionic Ca^{2+} crosslinks (red ellipse) in the alginate gel and covalent N,N-methylenebisacrylamide (MBAA) crosslinks (blue circles) in the polyacrylamide gel, intertwined and joined by covalent crosslinks (green squares) between amine groups on the polyacrylamide chains and carboxyl groups

on the alginate chains.[168] For comparison, SN-Gels,[173] abbreviated as poly (AAm-AAc) hereafter, were also synthesized.

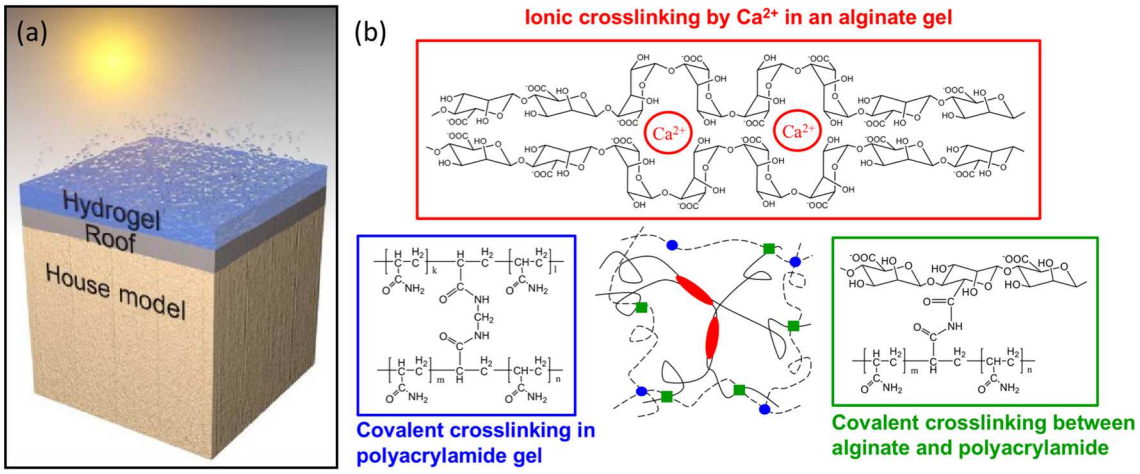

Figure 4.1. (a) Schematic of the experimental setup. Miniaturized house models were covered with a hydrogel layer and subjected to simulated solar irradiation to test the effectiveness and regenerability of cooling. (b) Chemical fomula of the alginate-polyacrylamide hybrid based DN-Gel. Two types of polymer networks, ionic Ca^{2+} crosslinks (red ellipse) in the alginate gel and covalent N,N-methylenebisacrylamide (MBAA) crosslinks (blue circles) in the polyacrylamide gel, intertwined and joined by covalent crosslinks (green squares) between amine groups on the polyacrylamide chains and carboxyl groups on the alginate chains.

4.4.1 Cooling effectiveness of DN-Gels

Figure 4.2 shows the results of the cooling experiments on the house models coated with the DN-Gel, SN-Gel, and without any gel, which were subjected to simulated solar irradiation of 800 W/m^2. As shown in Figure 4.2(a), both types of hydrogels exhibited similar cooling capability during the first three hours of solar irradiation. In comparison to the model without an applied hydrogel coating, water evaporation from the hydrogel coated models lowered the top temperature of the roof by as much as 30°C. However, the roof temperature of the SN-Gel coated model increased gradually after the first three hours and

reached the final equilibrium temperature after four hours, which is about 30°C and 8°C higher than the temperature of the top and bottom surfaces of the DN-Gel coated roof, respectively. Additionally, the DN-Gel enabled a significantly longer cooling duration and continuously maintained the bottom surface of the model roof at 49°C for up to seven hours, as shown in Figure 4.2(a). The longer cooling duration of the DN-Gel is also evident from the net heat flux entering the house models. The net heat input, as shown in Figure 4.2(b), was calculated from Fourier's law, $q = -\kappa \frac{dT}{dx}$, where the thermal conductivity (κ = 0.17 W/m·K) and thickness (0.025 m) of the roof is known and the temperature difference between the top and bottom roof surfaces was measured. Before solar irradiation, both DN-Gel and SN-Gel model houses were at room temperature. During the initial ~30 minutes upon solar irradiation, the temperature at the top and bottom surfaces of the house model were both increasing due to the transient heat transfer behavior (Figure 4.2(a)). As a result, the net heat flux entering the house models, which was calcuated based on the temperature difference between the top and bottom surfaces, also increased with time. This temperature rise resulted in higher water evaporation rate from the hydrogels, leading to decreasing net input heat flux in both the DN-Gel and SN-Gel cases from ~30 minutes to ~3 hours. After ~3 hours, the DN-Gel house reached the steady state, whereas the house covered with the SN-Gel, which contained a smaller amount of water, experienced increasing temperature and heat flux because the stored water was exhausted. With the DN-Gel layer, a much lower net heat input (~50 W/m^2) with constant cooling is observed compared to that of the SN-Gel layer (~250 W/m^2) after four hours, which shows that the DN-Gel effectively rejects about 93% of the incident solar irradiance. As we shall see later, the longer cooling duration of the DN-Gel layers is a result of the larger amount of absorbed water during the

soaking period (~8 hours) and a slightly larger thickness while in the dehydrated state (1.0 cm vs. 0.8 cm), compared to that of the SN-Gel.

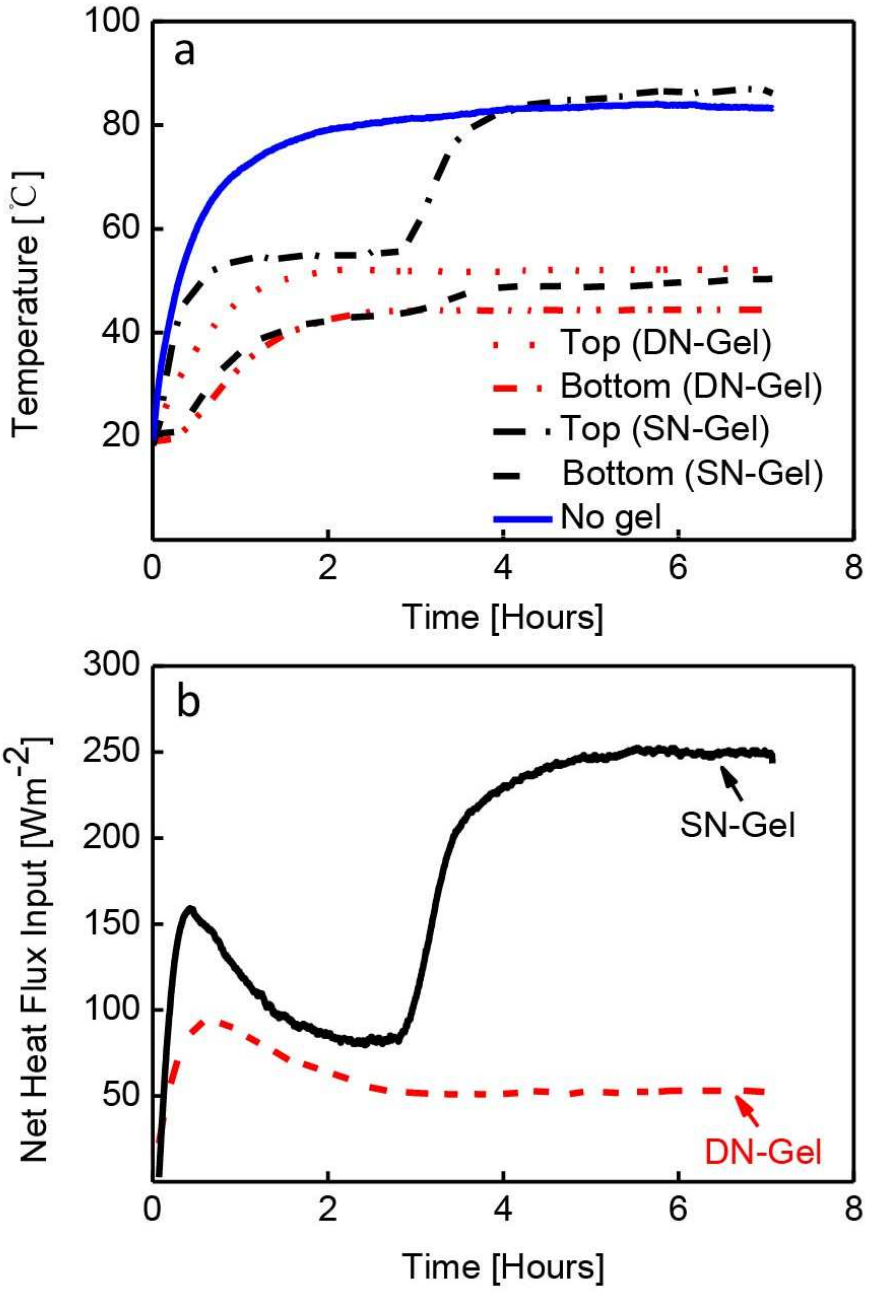

Figure 4.2. (a) Comparison of the cooling effectiveness of the DN-Gel and SN-Gel. (b) Net input heat flux entering the model houses coated with DN-Gel and SN-Gel layers. The DN-Gel provides a longer cooling duration with a lower net heat flux entering the structure, compared to that of the SN-Gel.

4.4.2 Cooling cyclability of DN-Gels

Two model houses, each covered with a DN-Gel and SN-Gel, respectively, were subjected to repeated cycles of drying for cooling (subjected to simulated solar irradiation) and replenishing by hydration charging (soaking in water). The model house with the DN-Gel was subjected to a total of 50 cycles, with 24 cycles of 700 W/m^2 (cloudy days) and 26 cycles of 800 W/m^2 (sunny days) solar irradiation, at a relative humidity of ~50% (ambient temperature). The DN-Gel effectively lowered the bottom surface temperature of the house roof to 43°C (Figure 4.3(a)) and 49°C (Figure 4.3(b)) for the 700 W/m^2 and 800 W/m^2 solar irradiation cases, respectively. The slight variation in roof temperatures was likely caused by ambient temperature/humidity changes. The cycling experiment clearly shows that the cooling power and water storage capacity of the DN-Gel layer does not degrade after 50 cycles, demonstrating the regenerability of the cooling performance offered by the DN-Gel. As shown in Figure 4.3(d), after 50 cycles, the DN-Gel network still maintains integrity upon repeated volume expansion and UV irradiation, further demonstrating its durability. This degree of cyclability has not been observed in any of the previously studied artificial hydrogel skins based on SN-Gels. Furthermore, the SN-Gel layer only exhibited sustained cooling capability during the first two cycles, maintaining the bottom temperature of the roof at 43°C (Figure 4.3(c)) for the 700 W/m^2 solar irradiation case. During the third cycle, the SN-Gel layer failed to cool the roof, and the bottom temperature increased to 50°C due to collapse of the SN-Gel network (Figure 4.3(d)).

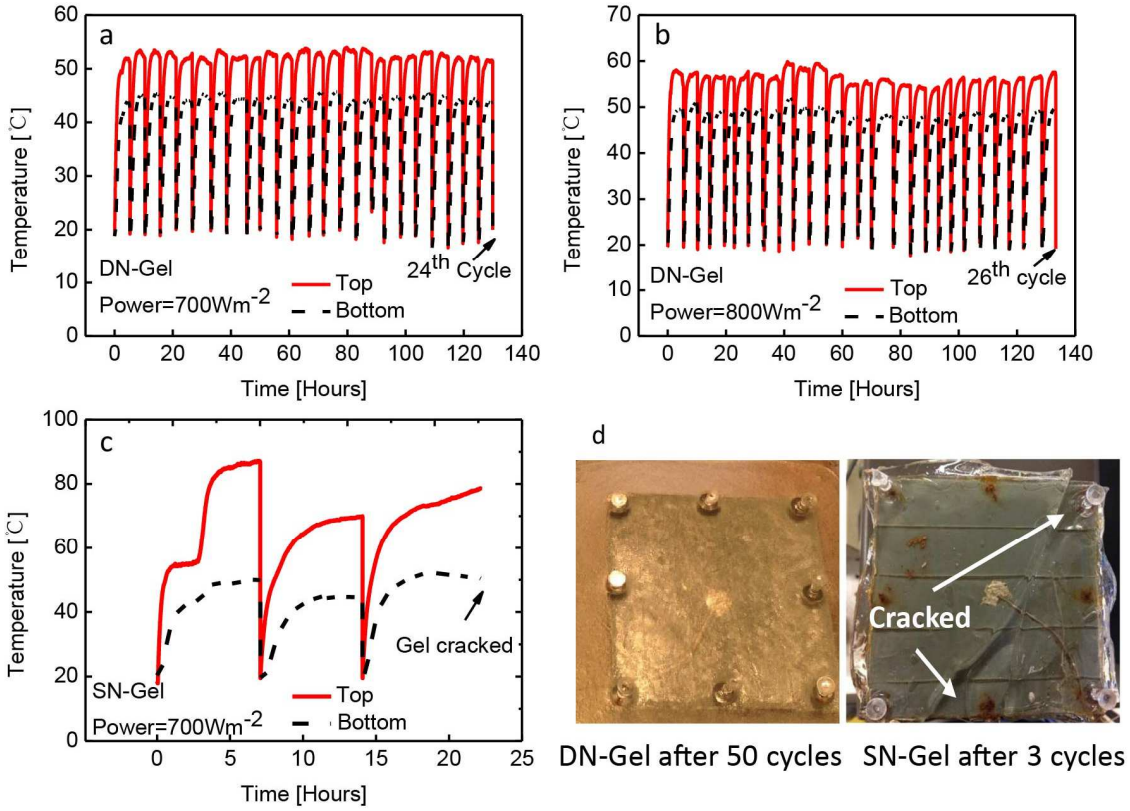

Figure 4.3. Cooling cyclability test of the DN-Gel and SN-Gel. Roof temperatures for: (a) DN-Gel coating for 24 cycles (cloudy days), (b) DN-Gel coating for 26 cycles (sunny days), and (c) SN-Gel coating for 3 cycles (cloudy days). (d) DN-Gel surface (intact after the 50th cycle) and SN-Gel surface (cracked after the 3rd cycle).

4.5 Sustainable mechanical performance of DN-Gels after cycling

In order to better understand the enhanced cooling cyclability and its correlation with the mechanical properties of the DN-Gel, tensile tests on fresh and cycled DN-Gels (after the aforementioned 50 swelling-deswelling cycles) were performed. Figure 4.4(a) shows that the cycled DN-Gels possess comparable stress-stretch curves to those of fresh gels, in both the swollen and dehydrated states, indicating little mechanical degradation due to cycling. The figure also shows that the DN-Gels in the dehydrated state are less stretchable than those in the fully swollen state for both fresh and cycled gels, as one would

expect. The sustainable high stretchability of the swollen DN-Gel after cycling is also demonstrated by the insets in Figure 4.4(a) for the cycled gel before and during the tensile test.

Besides the sustainable mechanical properties of the DN-Gel, the hydration (swelling) characteristics of the cycled DN-Gel layers are also comparable to the fresh ones. The cooling duration is dictated by the amount of water stored in the gel, which is characterized by the swelling ratio (SR). Figure 4.4(b) shows the SRs of the DN-Gels as a function of soaking time, demonstrating similar swelling behavior between the cycled and fresh samples. In both types of samples, the swelling process is initially fast and gradually slows down before reaching a maximum SR of approximately 40 after 50 hours. Figure 4.3(a) and (b) and Figure 4.4(b) show that the performance of the DN-Gel is not degraded during both the drying and replenishing processes, illustrating the regenerability of the hydrogels, which is important for building cooling applications.

The inset in Figure 4.4(b) also shows that the maximum SR is only ~4 for the SN-Gel. This observation is consistent with a previous study on the SR of the same SN-Gel, namely Poly (AAm-AAc).[176] Compared to DN-Gels, the charging capacity of the SN-Gel is 4 to 5 times lower within the 8-hour soaking time for the cooling effectiveness test. This explains the shorter cooling performance of the SN-Gel exhibited in Figure 4.2. It should be noted that this SR behavior is specific to the SN-Gel used in this study, i.e. Poly (AAm-AAc) with an AAc : AAm ratio of 7:3, in DI water at a relative humidity of ~50% and room temperature. Other compositions of AAc and AAm of Poly (AAm-AAc) in a different PH-buffer[173, 176] or other types of SN-Gels have shown larger SRs.[177-178]

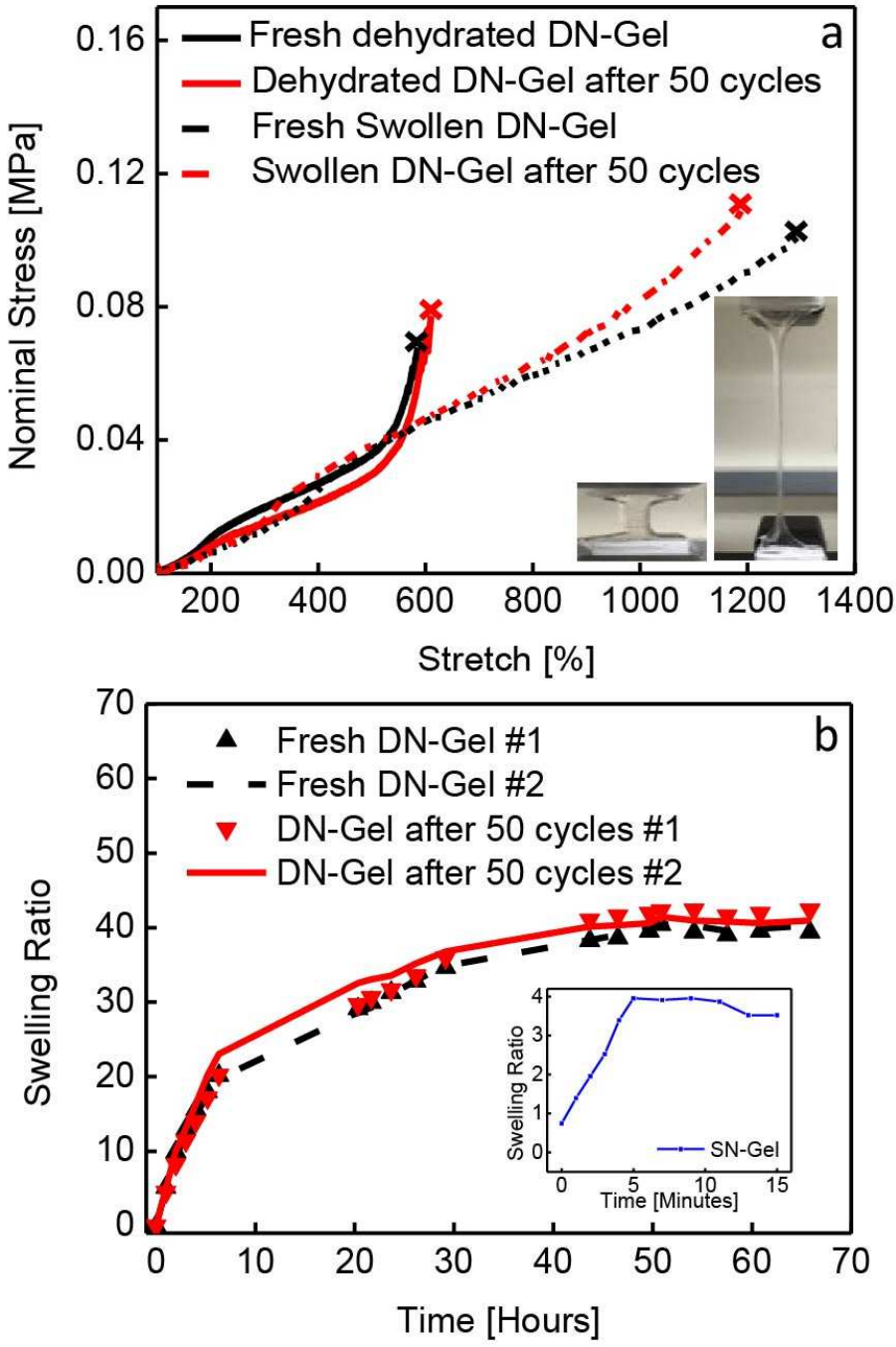

Figure 4.4. (a) Sustainable mechanical properties of the DN-Gels after 50 cycles compared to fresh DN-Gels in both swollen and dehydrated states, as measured by the nominal stress vs. stretch curves. Crosses indicate mechanical breakage of the specimens. Insets are the swollen DN-Gel after 50 cycles before and during the tensile test. (b) Comparable swelling ratio (SR) of the cycled and fresh DN-Gels. Insets shows the lower SR of the specific SN-Gel studied in this work, which explains its shorter cooling duration observed in Figure 4.2.

The fractured fresh and cycled (after 50 cycles) DN-Gels were dried via critical point drying (CPD) and the sample surfaces were examined with a scanning electron microscope (SEM). The surfaces, which fractured due to stress from the swollen state, reveal a porous structure (Figure 4.5(a) and (b)) compared with those of the dehydrated DN-Gels (Figure 4.5(c) and (d)). The fractured surface in the swollen state of the cycled DN-Gel (Figure 4.5(b)) is more porous than that of the fresh one (Figure 4.5(a)), leading to its slightly higher SR (Figure 4.4(b)). The porous structure in the swollen state also leads to a rougher surface of the cycled specimen in the dehydrated state (Figure 4.5(d)) after undergoing many cooling cycles. This observation is consistent with our initial hypothesis that the DN-Gels still maintain their mechanical integrity as well as the drying and replenishing performance, even after undergoing minor structural changes associated with the cycling.

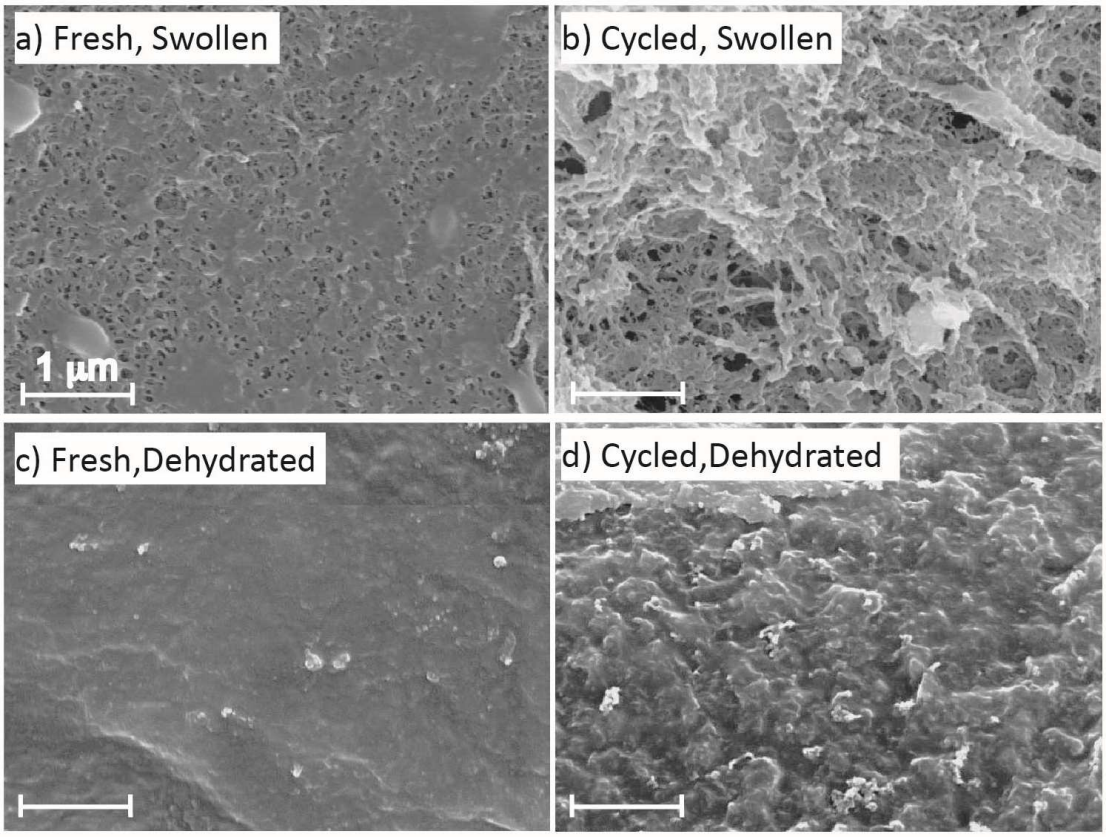

Figure 4.5. Surface characteristics of the DN-Gel in the (a) fresh and (b) cycled swollen state, and (c) fresh and (d) cycled dehydrated state. DN-Gels after 50 cycles show more porous and rougher surfaces in swollen and dehydrated states, respectively. Scale bars = 1 µm.

4.6 High transparency of DN-Gel

DN-Gel coatings are advantageous over other coating materials due to their high transparency when applied on building windows. To demonstrate the effectiveness for window cooling applications, DN-Gels were placed on a transparent glass sheet under simulated solar irradiation of 800 W/m^2. As shown in Figure 4.6, the temperature of the glass sheet covered with the DN-Gel layer is about 10°C lower than that of the control glass sample without a hydrogel layer over a period of 3 hours. The transparency of the DN-Gels is shown in the photographs taken before and after the cooling experiments, Figure 4.6(b)

and (c), respectively. Before the cooling test, the fresh DN-Gel contains over 95 wt% water. Images underneath the hydrogel layer and glass sheet are clearly visible (Figure 4.6(b)). As the temperature increases, the DN-Gel undergoes a phase transition from a hydrated swollen state to a dehydrated state, resulting in water release. The transparency of the DN-Gels decreases with reduced water content during cooling, as revealed by the blurry images under the DN-Gel and glass sheet in Figure 4.6(b). In order to adapt to different climates, the transparency of the DN-Gel can be set according to specific requirements by controlling the water content as well as evaporative cooling duration.

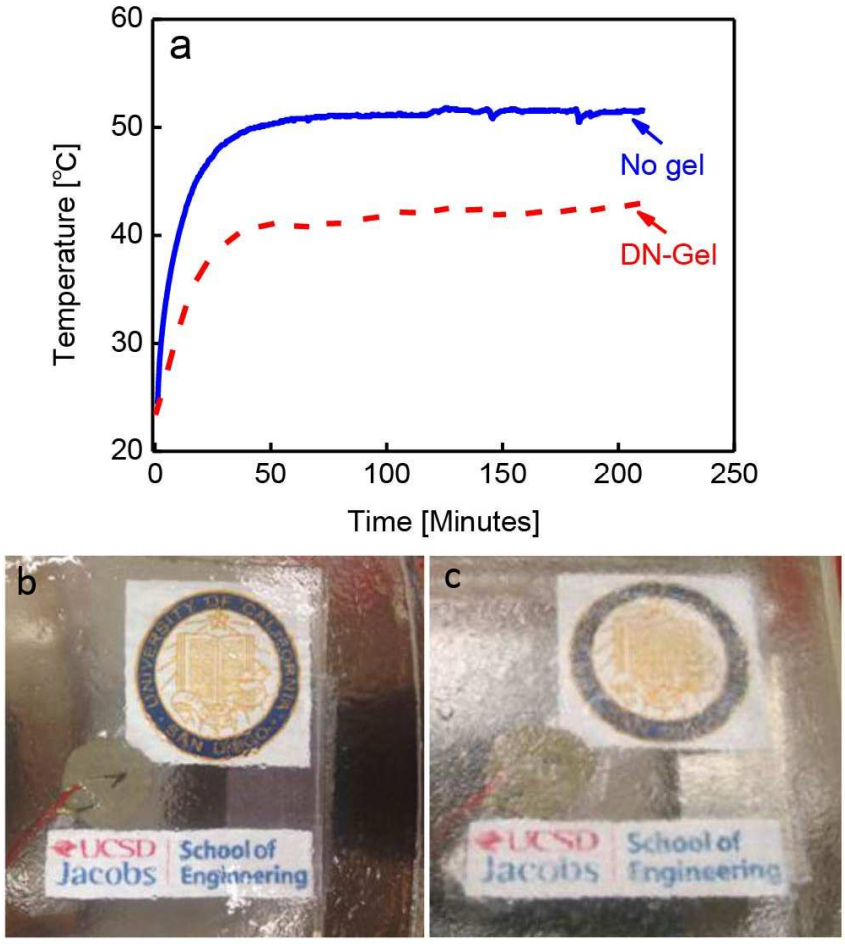

Figure 4.6. (a) Cooling effectiveness of the DN-Gel on transparent glass. Transparency before (b) and after (c) cooling performance tests.

4.7 Energy and economic analysis

4.7.1 Energy saving performance

The heat balance on the roof surface is: $\alpha I = L_0 + h_r(T_{roof} - T_{air}) + h_c(T_{roof} - T_{air})$,[179] where α is the solar absorptance (~50% for a silver-colored roof), I is the solar insolation (maximum ~1 kW/m^2), L_0 is the thermal radiative cooling rate varying from 50 $-$100 W/m^2 as demonstrated in Ref. [180], h_r is the radiative heat transfer coefficient ($h_r = 4\varepsilon\sigma T_{air}^3$, $\varepsilon = 0.9$ and $\sigma = 5.67$ W/m^2·K^4), and h_c is the convective heat transfer coefficient (~ 6.6 W/m^2·K, estimated in Ref. [181] for T_{roof} - T_{air} = 30 K). Therefore, the temperature difference is T_{roof} - T_{air} = (αI $-$L$_o$) / (h_r + h_c). Electrical energy savings and associated carbon dioxide (CO_2) emission reductions are estimated for a mid-sized house with and without the DN-Gel coating on the roof located in Southern California, shown in Table 4.2. In order to sustain an interior temperature of 20°C, an air conditioner will consume ~ 600 kWh of electrical power per year for a house with a silver-colored roof. With a DN-Gel coating on the roof, the electricity cost and CO_2 emissions are reduced by 47% for the same house. The hydration charging of DN-Gels can be accomplished by several ways, such as utilizing recycled water and collecting raining water. Based on the reduction in heat uptake (31 MJ per day) and the latent heat of water, the amount of water for hydration charging is estimated to be less than 1.4 m^3 per year for a roof area of 100 m^2.

We can further compare DN-Gel cooling technology to another emerging cooling technology, PCMs. PCMs are also a promising material for building thermal regulation but their main disadvantages are high material cost and low latent heat. For instance, paraffin,

one of the most common PCMs, has a cost of \$1692－1800 m^{-3} and a latent heat of 147 kJ/kg.[182] Hydrogel could be more advantageous due to its low cost (\$370 m^{-3}) and the associated high latent heat of water.

Table 4.2. Energy savings and CO_2 emission reduction with DN-Gel coating roof.

	$T_{outside}$ [°C] [a]	T_{inside} [°C]	Heat uptake /day [MJ] [b]	Electricity cost/year [\$] [c]	CO_2 emission/ year [kg] [d]
Bare roof (no gel)	67	20	~65	~90	~340
DN-Gel coating roof	45[e]	20	~34	~47	~180

[a] Calculated by assuming T_{air} = 35°C in hot summer. [b] Calculated as $(T_{outside} - T_{inside})UA_{house}t$ with $t = 6$ h and an overall heat transfer coefficient of roof U = 0.637 W/m^2·K.[183] A_{house}=100 m^2 is the irradiated surface area. [c] Assuming 100 hot days per year, electricity cost = \$0.15 / kWh, COP of an air conditioner = 3. [d] 0.563 kg CO_2 emission per kWh.[184] [e] h_r is 4-5 times higher when hydrogel coating is applied.[158]

4.7.2 Manufacturing scalability and application feasibility

Tough hydrogels can be manufactured at scale with low cost. The reagents, such as acrylic acid (AAc) and its sodium or potassium salts, and acrylamide (AAm), are already being used in large volume in hydrogel manufacturing,[185] e.g., baby diapers. Major equipment[186-187] involved in production, e.g. alginator and mixer, heater, and UV light for curing, are standard industrial equipment being employed in industrial polymer production.[188] Table 4.3 summarizes the estimated cost of the raw materials for manufacturing tough hydrogels. The total cost is approximately \$3.7 for a hydrogel sheet of 1 m^2 area and 1 cm thickness. Also, the high toughness enables the application of the DN-Gels directly on the surface for cooling with acrylic adhesive. Additionally, DN-Gels

can be encapsulated in the outermost layer of roofs, windows or walls with porous covers. After evaporative cooling, the hydration charging for DN-Gels can be achieved, for instance, via automatically irrigation systems.

Table 4.3. Raw reagents and their price for tough hydrogel synthesis.

Reagents	**Market Price ($)**	**Price($)/ kilogram**	**DN-Gel material(kg)/ piece***	**DN-Gel price($)/ piece**
Alginate (AG)	3000/ton	3	0.25	0.75
Acrylamide (AAm)	1900/ton	1.9	1.5	2.85
N,N'-methylenebis (acrylamide) (MBAA)	50/kg	50	0.001	0.05
Calcium Sulfate	500/ton	0.5	0.033	0.0165
N,N,N',N'-Tetramethylethylenediamine (TEMED)	5/kg	5	0.0037	0.0185
Ammonium Persulfate (AP)	700/ton	0.7	0.0025	0.00175
Total				$3.7

* 1 piece of tough hydrogel with dimension of 1 m ×1 m ×1 cm.

4.8 Conclusions

In summary, we have demonstrated the high cooling performance and remarkably regenerable cooling capability of tough DN-Gels for building cooling applications. The DN-Gels exhibit outstanding cooling performance by reducing the surface temperature of wood roofs and glass windows by 25－30°C and 10－15°C, respectively. Compared to SN-Gels, the cooling power and water absorption capacity of the DN-Gels are preserved for more than 50 cooling cycles. Compared to white roofs,[189-190] hydrogels have the additional feature of high transparency,[191] rendering them attractive for building window applications. Therefore, we envision that the remarkable mechanical and thermal properties

of these tough DN-Gels, especially the significantly improved cyclability, will offer a novel bio-inspired energy-efficient cooling approach for buildings. Our materials could also be applied for energy-efficient thermal management of other devices and systems, such as electronics, occupational clothing, and batteries.

Chapter 4, is a reprint of the material as it appears in Applied Energy, 2016. Shuang Cui, Chihyung Ahn, David Leung, Matthew C. Wingert, Shengqiang Cai, and Renkun Chen. The dissertation author was the first author of this paper.

5 Chapter 5 Super-absorbing porous thermo-responsive hydrogel composite (TRHC) desiccant with low regeneration temperature

5.1 Introduction

Desiccants are hygroscopic materials with high affinity to water vapor. They generally have lower partial vapor pressure than surrounding air at the same temperature, thus absorbing or adsorbing moisture from air when brought into contact. Desiccants are of great importance in humidity control and have numerous applications, including dehumidification in food and medicine,[192] desiccant assisted cooling in building heating, ventilating, and air conditioning (HVAC) systems,[61, 193] water harvesting in drought areas,[194-196] and natural gas dehydration in oilfields.[197-198] Desiccants are typically classified into two categories based on their physical states: liquid desiccants and solid desiccants. Liquid desiccants, such as LiCl and $CaCl_2$ salts, usually have a high absorption capacity. They form crystalline hydrates through chemical reaction with water molecular during the absorption, and then dissolve into the absorbed water, finally result in aqueous salt solution.[199] This deliquescence of liquid desiccants limits their applications in many scenarios. For instance, it is difficult to handle aqueous solution in dehumidification of food and medicine. Additionally, the salt solution is corrosive to certain metals if it leaks into the system (so called the 'droplet carryover' problem).[200] Therefore, solid desiccants are more preferred due to their ease and versatility of operation, and chemical inertness.[51, 201] Typical solid desiccants, such as silica gels, zeolites, and natural clays, achieve physical adsorption of the vapor molecular onto their surface via hydrogen bonding and retain the

moisture because of the difference of vapor pressure in the pores of the desiccants and in the surrounding air. However, solid desiccants have relatively low adsorption capacity and kinetics compared to liquid desiccants because the adsorption process occurs on the surface and water molecules cannot penetrate into the interior of the material. For silica gels, even with high surface area of 650－900 m^2/g enabled by nanometer-scale pore size ranging from 2－3 nm (type A) to about 0.7 nm (type B),[202] they still have a relatively low adsorption capacity (0.37 g/g, or 0.37 gram of absorbed moisture per gram of desiccant) and a slow adsorption rate with diffusivity of ~3.41×10^{-11} m^2/s at room temperature and 76% relative humidity (RH).[203] Recently, composite desiccants such as the 'salt in matrix' (SIM) structures have been considered as a promising approach to improve the adsorption capacity of solid desiccants.[204-205] By impregnating hygroscopic salts inside the traditional solid desiccants, such as silica gels, zeolites and natural clays, the adsorption capacity of the composite desiccants can be enhanced by 3 to 5 times.[206] The adsorption properties of composite desiccants can be further tailored through varying the host matrix material and structure, salt chemical nature and content, and synthesis conditions.[207-209] For example, superabsorbent polymers, such as polyacrylamide and polyacrylate, have been chosen as the matrix due to their high water retention capability.[210-211] Superabsorbent hydrogel composite (SHC) desiccants made of superabsorbent polymer matrix can achieve a high absorption capacity of 2.43 g/g (90% RH and 30°C, 80 wt% $CaCl_2$ in polyacrylamide matrix)[212] and 2.76 g/g (99% RH and 25°C, 87 wt% LiCl in polyacrylate matrix),[213] respectively.

Though numerous ongoing studies have been directed at the fabrication of advanced desiccants with improved water sorption capacity, less attention is paid to

improve the adsorbate transport and regeneration ability of desiccants, which is of great significance for applications such as desiccant assisted air conditioning. The ideal desiccant should have fast sorption and desorption kinetics, especially easily desorbs the moisture at a relative low temperature for high energy efficiency since the regeneration process is usually realized by heating, which is typically energy intensive. To fully utilize low-grade thermal energy, it is desirable to limit the regeneration temperature to be less than 80°C because over 50% of waste heat resources lie in the temperature range of 32－82°C[214] and a lower temperature typically means less heat loss. However, it is difficult for solid desiccants to simultaneously possess both high adsorption capacity and low regeneration temperature because a strong affinity to water for high adsorption capacity means high thermal energy required to break the adsorbent-adsorbate bonds during the regeneration.[205] The state-of-the-art composite desiccants with $CaCl_2$ in silica gel matrix have regeneration temperature of 80－100°C, low adsorption capacity ranging from 0.3－0.76 g/g. Although no regeneration data was reported for SHC desiccants, an even higher regeneration temperature is expected because the superabsorbent polymers have a stronger water affinity (hydrophilic), the very reason why they have a super-high absorption capacity. Thus, developing a novel desiccant with high adsorption capacity as well as fast desorption at a low regeneration temperature is significant for a variety of energy efficient applications involving desiccants.

Here, we proposed and demonstrated a porous thermo-responsive hydrogel composite (TRHC) desiccant with high adsorption capability (~2.3 ± 0.1 g/g in 3 hours at 97% RH and RT) and fast desorption at a low regeneration temperature (over 60% water removal during desorption in 50 minutes at 50°C) for the first time, by impregnating

hygroscopic agents into a thermo-responsive hydrogel matrix via a sol-gel method. The resultant solid desiccant has similar behavior to liquid desiccant and possesses type-III isotherm[215] based on the classification of IUPAC (International Union of Pure and Applied Chemistry) due to its hygroscopic nature offered by the salt ($CaCl_2$). TRHC desiccant utilizes the salt on the surface of the porous hydrogel matrix to achieve high-capacity and fast adsorption as in liquid desiccants, and yet the hydrogel matrix serves as the water storage medium to prevent the leakage of the liquid salt (i.e., solution carryover), thus effectively converting the liquid salt into a solid desiccant. Meanwhile, the unique thermo-responsiveness of the hydrogel matrix facilitates the fast desorption at a relative low regeneration temperature since the matrix, mainly made of N-Isopropylacrylamide (NIPAAm), becomes hydrophobic above its lower critical solution temperature (LCST, ~32°C)[158, 216] and results in polymer shrinkage for facile water release.

5.2 Material preparation

5.2.1 Reagents and materials

The monomers of N-Isopropylacrylamide (NIPAAm) and sodium alginate were purchased from Sigma-Aldrich, ≥ 99% reaction grade. N,N'-Methylenebis(acrylamide) (MBAA, 99%) and aluminum chloride hexahydrate ($AlCl_3 \cdot 6H2O$, 99%) as cross-linker, α-ketoglutaric acid (≥ 98.5%) as initiator, and anhydrous calcium chloride (≥ 97%) as hygroscopic agents were also purchased from Sigma Aldrich.

5.2.2 Thermo-responsive hydrogel synthesis

Thermo-responsive hydrogels were synthesized in a two-step method as shown in Figure 5.1, by following our previous synthesis of tough hydrogels.[210, 217] In the first step, NIPAAm, sodium alginate, α-ketoglutaric acid, and MBAA were dissolved in deionized (DI) water to obtain a homogeneous solution. This solution was transferred into a mold and irradiated by UV light (λ=365 nm) for 12 hours. After UV exposure, the NIPAAm monomers were polymerized, resulting in a Na-alginate/PNIPAAm hydrogel. In the second step, the Na-alginate/PNIPAAm hydrogel was immersed in an $AlCl_3$ aqueous solution, resulting in the transparent Al-alginate/PNIPAAm hydrogel by replacing the Na^+ cations with Al^{3+} cations.

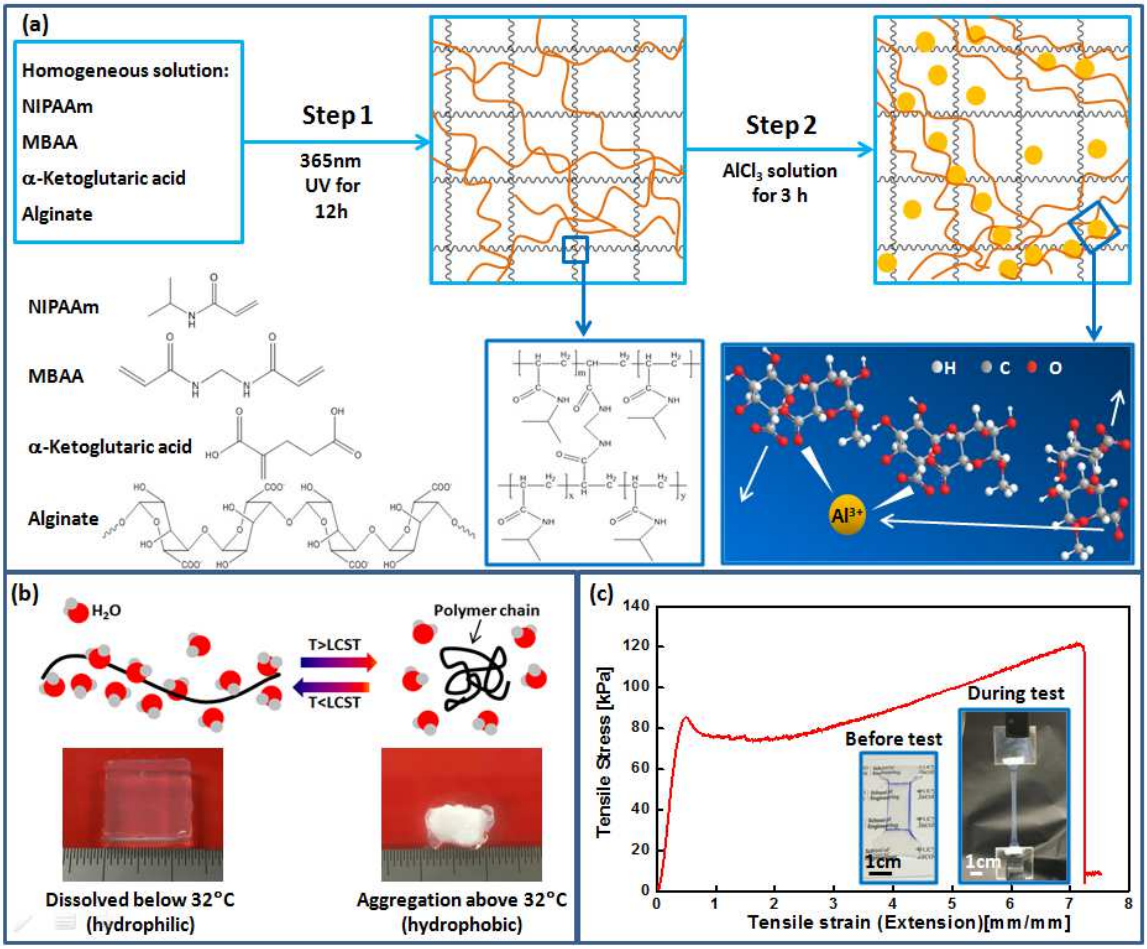

Figure 5.1. (a) Two-step method used to create TRHC desiccant's thermo-responsive polymer matrix—double network Al-alginate/PNIPAAm hydrogel—through free radical polymerization. (b) Schematic demonstrating thermo-responsive behavior of Al-alginate/PNIPAAm hydrogel with reversible dramatic volume change when temperature is higher or lower than the LCST. (c) Tough and highly stretchable Al-alginate/PNIPAAm hydrogel (stretched up to 7 times) with inset pictures of dog-bone shaped specimen before and during tensile test.

5.2.3 Porous thermo-responsive hydrogel (TRHC) desiccant synthesis

TRHC desiccants were synthesized with a two-step freeze drying method by impregnating inorganic salt (anhydrous calcium chloride) into porous thermo-responsive and tough hydrogel matrix, as shown in Figure 5.2(a-d). Thermo-responsive and tough hydrogels were first immersed in DI water until a fully swollen state was reached. Then

the hydrogels were cut into 1.3 cm^2 squares (Figure 5.2(a)), packed in ice in a freezer, and freeze dried for the first time to form porous hydrogel matrix with a mass of M_1 (Figure 5.2(b)). We then soaked the hydrogel matrix in a $CaCl_2$ solution, froze the salt-solution swollen samples with liquid nitrogen, and freeze dried it again to remove excess water with a mass of M_2. Thus, TRHC desiccants were obtained, as shown in Figure 5.2(d), with a salt loading mass (M_2-M_1) and hydrogel polymer matrix mass of M_1.

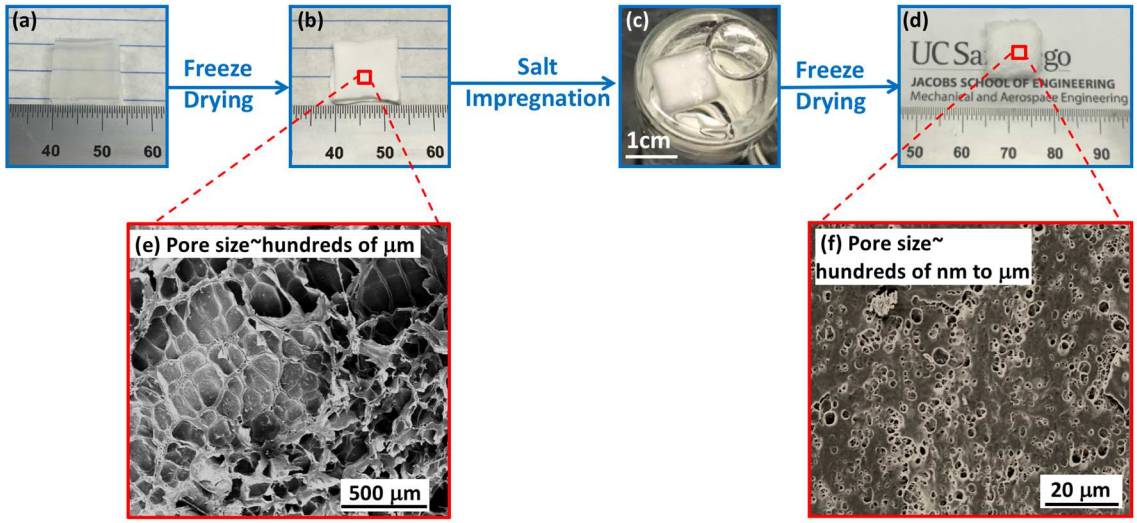

Figure 5.2. (a-d) Porous TRHC desiccant synthesized using salt solution soaking and freeze drying method. (e) SEM of porous Al-alginate/PNIPAAm hydrogel matrix top surface with hundreds of µm pore size after freeze drying. (f) Hygroscopic shell surface with hundreds of nm to a few µm pore size.

5.3 Material characterization

5.3.1 Surface morphology

For surface and cross-sectional morphology analysis, SEM was used. The samples were packed in ice in a freezer (10 hours) or liquid nitrogen (30 minutes) before freeze drying. Ten measurements from the SEM images of at least 3 different positions were used to provide the average pore size. Electron Diffraction Spectroscopy (EDS) was additionally

employed to investigate the constituent of a TRHC desiccant based on three measurements at three different positions.

5.3.2 Hydrogel swelling/deswelling kinetic study

For the immersion swelling kinetic study, two identical freeze dried gels (13 × 13 × 2 mm) were immersed in a 500-ml DI water bath at room temperature (RT). The gels were retrieved from the water and weighed at certain intervals until an equilibrium weight was achieved. The swelling ratio (R_s) was defined as $R_s = (W_t\text{-}W_d)/W_d$,[218] where W_t is the gel weight at time t, and W_d is the dehydrated weight of the gel. For immersion de-swelling kinetics, fully swollen samples (13 × 13 × 2 mm) at RT were transferred to a 500 ml and 50°C water bath, retrieved from the water, and weighed at certain time intervals. The de-swelling ratio (R_{ds}) of the gel was calculated using the equation, $R_{ds} = (W_s - W_t)/(W_s - W_d)$,[219] where W_s is the fully swollen gel weight at RT. The dehydrated weight (W_d) of the gels for swelling ratio test was measured after freeze drying for 24 hours and that for the de-swelling ratio test was measured after 24-hr drying in a 90°C oven.

5.3.3 Toughness of thermo-responsive hydrogels

For tensile tests, a universal testing instrument (Instron 5965) was used with a strain rate of 0.02 s^{-1}. Dog-bone shaped specimens were cut according to the ASTM D-412 standard with the size of tensile part of 20 × 10 × 2 mm (Figure 5.1(c)). Nominal tensile stress was defined as the ratio between the applied force and the initial cross-sectional area of the specimen, and stretch was defined as the ratio of the current and initial lengths of the specimen from at least 3 replicate tests.

5.3.4 Water vapor adsorption equilibrium and dynamics study

The water vapor equilibrium and dynamics of the desiccants during the adsorption and desorption processes were performed by uptake measurement under isothermal conditions.[208] A system to measure the instantaneous weight increase or loss of samples in a humid environment was built using a climate chamber to provide air with controlled humidity and temperature (ZH-8-1-1-H/AC, Cincinnati Sub-Zero, US, measurement range of 20%－99% RH and -73－177°C), shown in Figure 5.3. A sample holder (swing), which is made of Teflon to avoid condensation, was suspended on an analytical balance (SI-114, Denver Instrument, US, measuring range of 0－110 g and accuracy of ± 0.1 mg). The sample's dynamic mass change (Δm) was recorded via a RS232 connection to a computer at an interval of 30 s using a data logging software. A humidity and temperature sensor (SHTC1, Sensirion, Switzerland, measurement range of 0－100% RH and -30－100°C, accuracy of ± 3% RH and ± 0.3°C) was located near the swing to simultaneously monitor the temperature and humidity. The gravimetric measurement was first calibrated with a standard weight (1 g), revealing a resolution of ± 5 mg as shown in Figure 5.4(a), by subtracting the total mass (swing plus standard weight) from the swing mass only. Before the tests, the incubator was conditioned at the targeted temperature and humidity, and its stability in the specified humidity and temperature during adsorption (RT and 97% RH) and desorption (50°C and 30% RH) are shown in Figure 5.4(b) and (c).

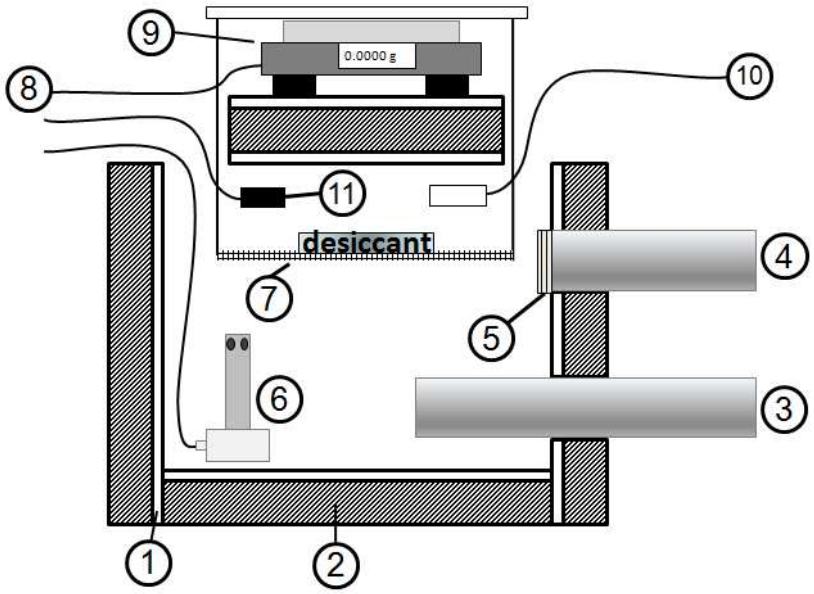

Figure 5.3. Diagram of the custom-built chamber used to test adsorption and regeneration behavior of TRHC desiccant. 1. ¼" acrylic sheet 2. Fiberglass insulation 3. Air return channel to environmental chamber 4. Air outlet from environmental chamber 5. Fan 6. Relative humidity sensor, output to environmental chamber 7. Teflon mesh sample holder, supported by stainless steel wire to plastic bar placed on digital balance 8. RS232 connector 9. Digital balance, output recorded by PC 10. Temperature sensor, output to environmental chamber 11. Temperature and humidity sensor, output to PC.

For the adsorption/desorption test, TRHC desiccant was placed on the sample holder after stabilization of the conditions in the test chamber for 2 hours. Vapor adsorption/desorption quantity was calculated as change in mass ($\Delta m = m_t - m_{dry}$ or $\Delta m = m_w - m_t$) over the dehydrated or wetted mass (m_{dry} or m_{w}) of desiccant, where m_{dry} is the pre-freezing dried desiccant mass for 24 hours to remove moisture residue, m_{w} is the wetted mass after equilibrium moisture content uptake (EMC), and m_{t} is the desiccant mass at time t. For the EMC uptake experiment, mass gain (Δm) of the desiccant was monitored and recorded continually at each RH level until it reached steady state ($\Delta m < \pm 5\%$) at room temperature, then transferred to the next RH condition.

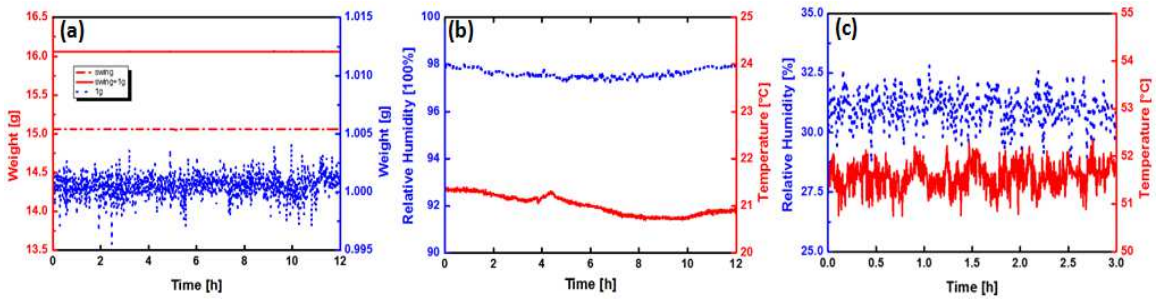

Figure 5.4. Moisture uptake measurement calibration. (a) Mass calibration of a standardized one gram weight with ± 5 mg resolution over 12 hours by subtracting the swing weight from the total weight. (b, c) Temperature and humidity calibration for adsorption (12 hours) and desorption (3 hours) testing conditions with ± 0.3°C and ± 3% RH uncertainty.

5.4 Adsorption/Desorption Mechanism

We synthesized the TRHC desiccants via sol-gel method as described in the experimental section. The schematic of the TRHC desiccant is shown in Figure 5.5, with a hygroscopic agent coated outside the porous polymer matrix. The adsorption/desorption mechanism is explained in Figure 5.5. The process of moisture transport and adsorption takes place in the following sequence[220]: (i) external diffusion of vapor from the phase boundary into the pore space; (ii) internal diffusion of vapor through the pore space; (iii) solid sorption resulting in the formation of salt crystalline hydrates; and (iv) finally, liquid absorption resulting in the salt solution, which then diffuses into the porous hydrogel matrix and results in swelling matrix as shown in Figure 5.5(a). The absorption process continues until the TRHC desiccant reaches its equilibrium moisture content, indicating equilibrium vapor pressure between TRHC desiccant and the surrounding air. The LCST behavior of NIPAAm in the hydrogel enables it to be regenerated at a relatively low temperature for water removal. During desorption at 50°C, which is higher than the LCST of NIPAAm

(~32°C), the hydrogel matrix shrinks and squeezes the water to the matrix surface of the TRHC desiccant (Figure 5.5(b)). The desorption process continues by evaporating the released water until almost all the adsorbed moisture is removed.

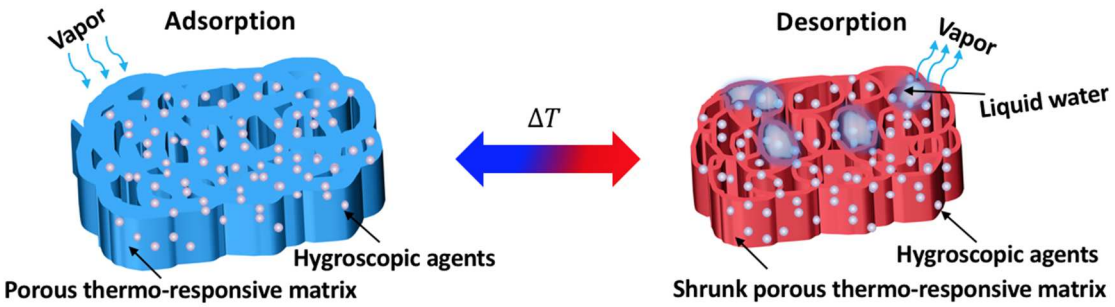

Figure 5.5. Schematic of superabsorbent solid thermo-responsive hydrogel composite (TRHC) desiccant created by impregnating hygroscopic agents into porous thermo-responsive polymer matrix. (a) Adsorption of TRHC desiccant: vapor is absorbed by hygroscopic salt on the surface, transported and stored into interior porous polymer matrix. (b) Desorption of TRHC desiccant: LCST behavior promoted water transport from inner polymer matrix shrinkage (thicker to thinner polymer thickness) to matrix surface, and water then evaporates out on the surface.

We used a composite structure with $CaCl_2$ salt impregnated inside the thermo-responsive Poly(N-Isopropylacrylamide) (PNIPAAm) hydrogel as other composite desiccants with SIM structures.[221] The PNIAAm hydrogel was synthesized via free-radical polymerization following a two-step method, as described in the experimental section. As shown in Figure 5.1(a), the NIPAAm monomers were first polymerized and cross-linked through chemical bonding by N, N'-Methylenebis(acrylamide) (MBAA), resulting in a Na-alginate/PNIPAAm hydrogel. Na^+ cations were later replaced by Al^{3+} ions in the second step through diffusion when immersing Na-alginate/PNIPAAm hydrogel into an $AlCl_3$ aqueous solution, resulting in a physically cross-linked alginate polymer through the electrostatic interaction between the Al^{3+} cations. The obtained transparent double network

hydrogel (Figure 5.1(b) and Figure 5.6(a)), is hydrophilic and superabsorbent when the temperature below its LCST. Al-alginate/PNIPAAm hydrogel is capable of storing nearly 30 times of its own weight in water at room temperature (below LCST) (Figure 5.6(c)). The absorption capability is mainly due to the hydrophilic amide group (－CONH－) in NIPAAm forming hydrogen bond with water molecules and the osmotic pressure from Al-alginate, as described by the Flory theory.[211] During the swelling process, the water penetrates into polymer networks and produces a 3D-molecular network by expanding the molecular chain between the cross-linked points, thus decreasing the configuration enthalpy value. Meanwhile, the molecular network has an elastic contractive force that contracts the networks. The hydrogel reaches the maximum swelling ratio when these opposing expansion and contraction forces reach equilibrium (Figure 5.6(c)). This superabsorbent property makes hydrogels highly suitable for adsorbate storage during adsorption, similar to other superabsorbent polymers used in SHC desiccants.[212-213]

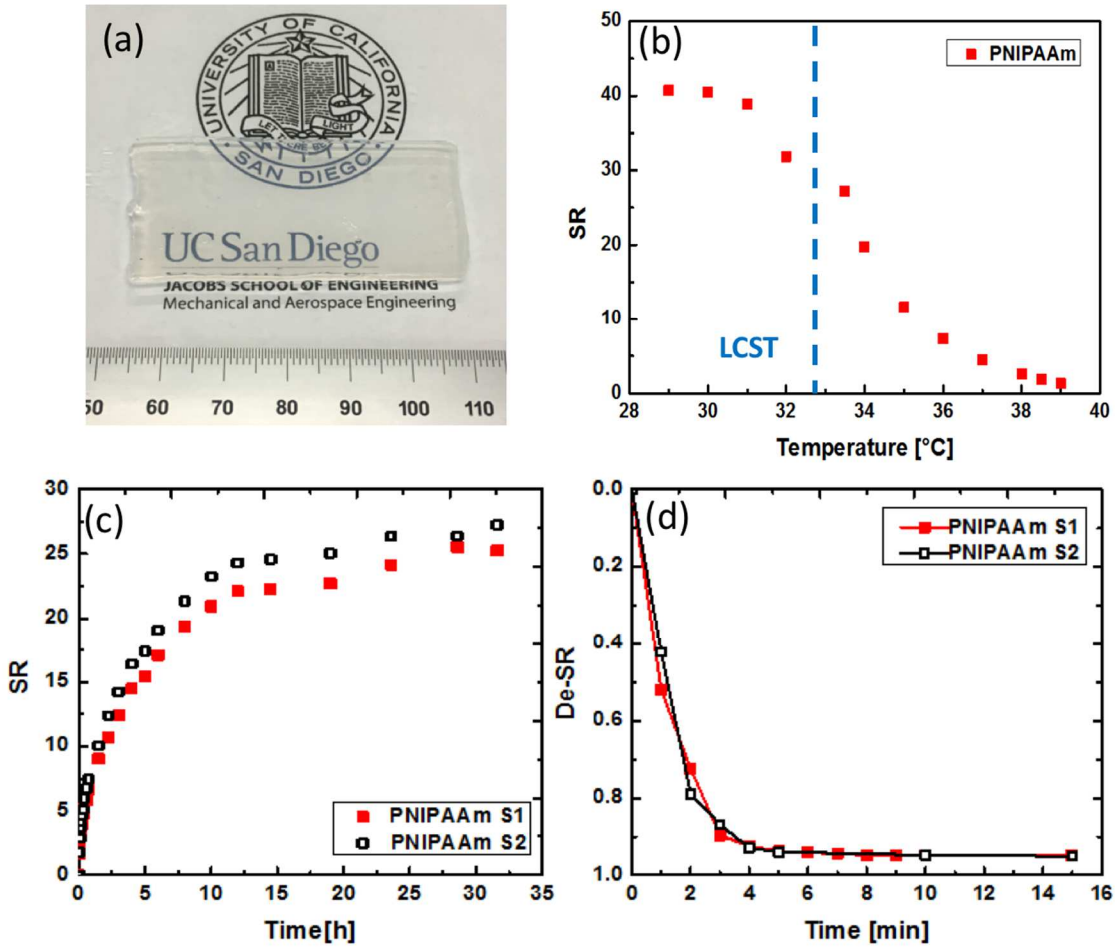

Figure 5.6. Swelling and de-swelling of Al-alginate/PNIPAAm hydrogel. (a) As synthesized transparent double network Al-alginate/PNIPAAm hydrogel. (b) LCST of Al-alginate/PNIPAAm hydrogel. (c, d) DI-water immersion swelling ratio and de-swelling ratio of Al-alginate/PNIPAAm hydrogel of two repilca samples with 13 × 13 × 2 mm size.

When exposed to the temperature higher than LCST, the hydrogel undergoes the phase transition from the transparent to the opaque state due to the change of hydrophilicity to hydrophobicity, resulting in a release of ~90% of the swollen water in the gel within 5 minutes by gel shrinkage (Figure 5.1(b) and Figure 5.6(d)). The LCST of the Al-alginate/PNIPAAm hydrogel is ~32°C with a decreased swelling ratio observation of the gel when exposed to the water in the temperature range of 28－39°C, shown in Figure 5.6(b). To effectively serve as water withholding medium, as shown in Figure 5.1(c), the

hydrogel could be stretched up to 7 times under 120 kPa tensile stress without failure, tough enough to prevent the collapse of porous structure from expansion/shrinkage in adsorption/desorption processes. This extraordinary toughness of the gel originates from coexisting of both chemical (MBAA) and physical cross-links (electrostatic interaction between Al^{3+} and carboxylic groups (COO^{-}) in alginate polymer chains),[170, 217] which enhances the toughness of the matrix compared to silica gels and superabsorbent polymers.

5.5 Pore size and salt loading quantity effect

Following the two-step freeze drying process, porous TRHC desiccant was created by soaking the porous dehydrated PNIPAAm gel in a $CaCl_2$ solution (Figure 5.2(a-d)). The porous polymer matrix made from the freeze drying by ice sublimation of the fully swollen PNIPAAm gel (Figure 5.2(a)) is shown in Figure 5.2(b). We utilized different freezing temperatures to control the pore size of the porous matrix by controlling the morphology of the ice crystals.[222-223] $CaCl_2$ salts were embedded inside the porous matrix through diffusion by soaking the polymer in the salt solution in Figure 5.2(c). Further water removal through freeze drying resulted in TRHC desiccant with a hundreds of nm to a few μm thick porous salt layer, as shown in the SEM image (Figure 5.2(f)) onto porous PNIPAAm matrix with hundreds of μm pore size (Figure 5.2(e)). The average pore size is also calculated based on BET surface area, which shows an averaged ~120 μm pore size for porous PNIPAAm matrix and ~2 μm pore size for TRHC desiccant in Table 5.1. The presence of uniform $CaCl_2$ coating on the top surface of the TRHC desiccant was confirmed through EDS by Ca element and the large Cl element peak in Figure 5.7(b). Meanwhile, no Ca element was detected through EDS in the freeze dried as-synthesized polymer matrix

(before salt soaking) in Figure 5.7(a). While other elements, such as C and O, are from the polymer monomers, Al and a small amount of Cl are from physical cross-linkers, and Ir is from the coating layer during sample preparation for SEM and EDS.

Table 5.1. Average pore size of dehydrated gel and TRHC desiccant.

Sample	Density (mg/cm^3)	BET surface area (m^2/g)	d_{avg} (μm)
Dehydrated Gel	3.3	7.6	~120
TRHC Desiccant	74	10.9	~2

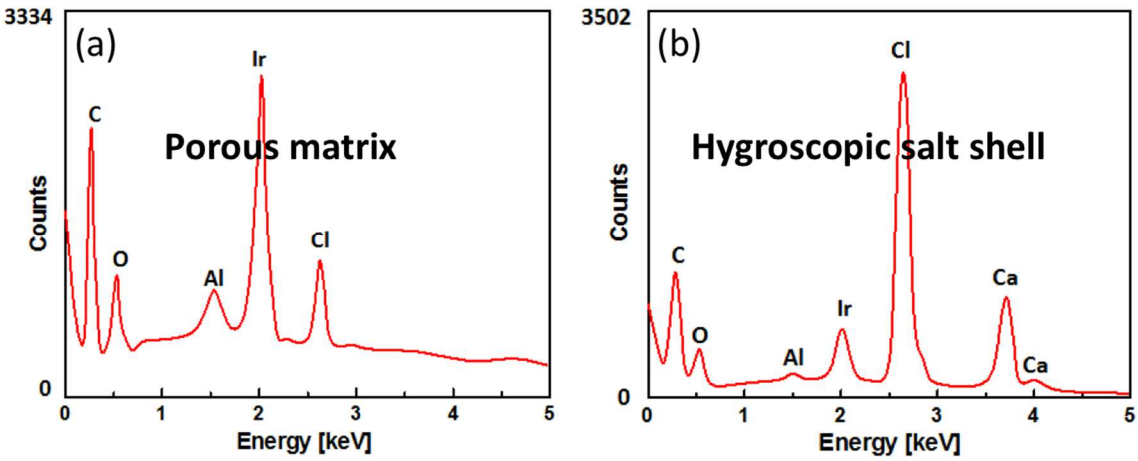

Figure 5.7. (a) EDS of Al-alginate/PNIPAAm hydrogel matrix. Elements of C, O, Al, and partial Cl are from polymer matrix, Ir is from sample preparation for SEM. (b) EDS of TRHC desiccant top surface shows hygroscopic inclusions ($CaCl_2$) embedded inside polymer matrix with elements of Ca and a huge peak of Cl detected.

In order to identify which TRHC desiccant synthesis method resulted in the best-performing material, different drying methods and freezing temperatures were systematically studied to maximize the adsorption kinetics and capacities. As shown in Figure 5.8(a), the TRHC desiccant created by freeze drying has a 50% higher 24-hr

adsorption capacity compared to those created by oven drying at 90% RH and RT. This increase in vapor transport kinetics is due to the porous structure retained after freeze drying of liquid nitrogen (LN_2) frozen gel matrix. The higher adsorption capacity benefits from more salts diffusion into the porous TRHC desiccant within the same salt solution soaking period. Further optimization of pore sizes for faster vapor transport was also investigated. It was found that the uniform pore size of as-prepared gel is 20 μm when frozen by ice[224] (Figure 5.8(c)). As-prepared gels that were frozen by liquid nitrogen (LN_2) in the first freezing step exhibited a closed-pore structure (Figure 5.8(e)). Larger pore size was achieved by freeze drying fully swollen gel following either by freezing in ice (200 μm pore size in Figure 5.8(d) or freezing in liquid nitrogen (20 μm pore size in Figure 5.8(f)). Different combinations of the two different freezing steps were studied to achieve fast vapor transport and high salt holding capacity as shown in Figure 5.8(b). Samples fabricated with a combination of two-step freezing in ice followed by liquid nitrogen (Ice-LN_2) provide the highest 12-hr adsorption capacity, due to a higher amount of inorganic salts captured inside the porous structure by opening large pores first with ice freezing and then closing the pores with liquid nitrogen freezing. The Ice-Ice samples showed similar adsorption characteristics to the Ice-LN_2 samples, with a slightly faster absorption rate in the first 4 hour and slightly lower equilibrium absorption capacity, presumably due to the larger pore sizes created by the second ice freezing step.

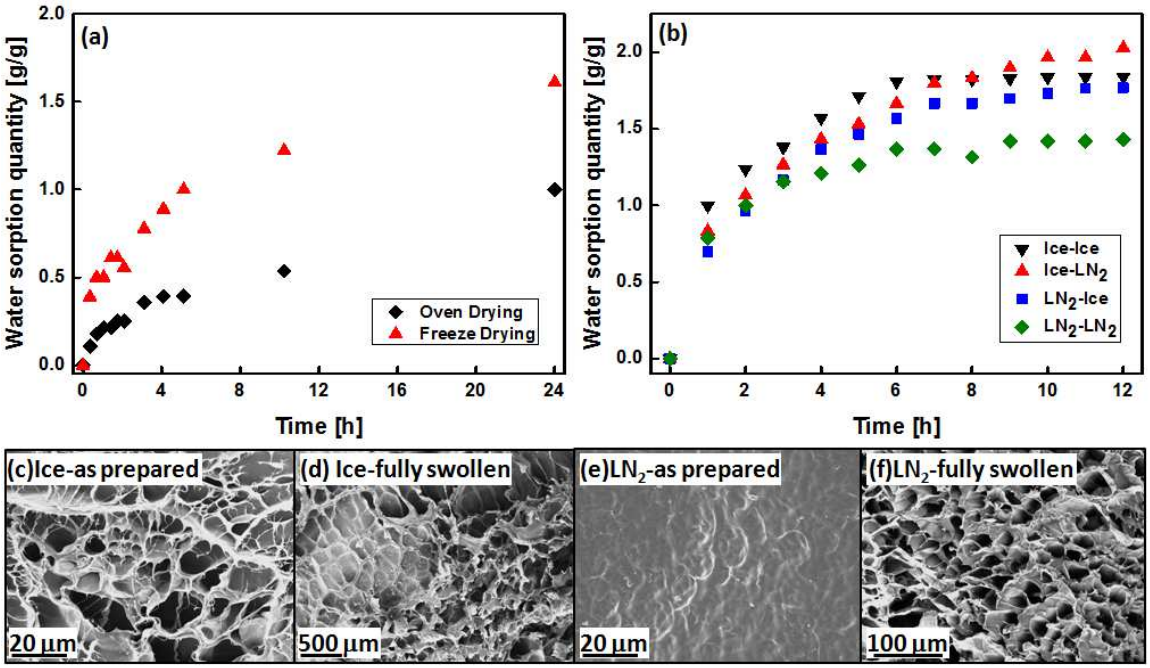

Figure 5.8. (a) Comparison of water adsorption quantity of TRHC desiccant prepared by oven drying and freeze drying. (b) Comparison of water adsorption quantity of TRHC desiccant with different combination of frozen methods (ice and liquid nitrogen). (c, d) Ice-frozen gel freeze-dried as synthesized (pore size ~tens of µm) and after swelling in DI water (pore size ~hundreds of µm), respectively. (e, f) LN_2-frozen gel freeze-dried as synthesized (no pores) and after swelling in DI water (pore size ~tens of µm), respectively.

5.6 High adsorption capacity

We then systematically test the adsorption behavior on Ice-LN_2 samples. We first carried out the isothermal adsorption test by measuring the samples in varying RH values of 30 to 97% at RT, following the protocol described in the section 5.3.4 using a home-built setup (shown in Figure 5.3 and calibrated in Figure 5.4). As shown in Figure 5.9(a), as expected, the adsorption rate and capacity increase with RH due to the larger vapor pressure gradient for mass transfer. For instance, the desiccant reached an adsorption capacity of 3.8 ± 0.2 g/g within 10 hours at 97% RH and yielded ~0.45 g/g adsorption capacity within ~1 hour at 30% RH. The adsorption capacity of the TRHC desiccant is

characterized by its equilibrium moisture uptake (EMC), which is the saturated moisture adsorption under the isothermal condition (RT) with various RH levels (Figure 5.9(a)). EMC of the TRHC desiccant extracted from Figure 5.9(a) is displaced in Figure 5.9(b), and is compared to other solid desiccants ranging from 30% to 90% RH at RT. The adsorption capacity of TRHC desiccant is ~5× higher than that of silica gel at low RH (< 70%). Even compared to other composite desiccant ($CaCl_2$ impregnated silica gel),[225] TRHC desiccant reveals ~30% to 70% improvement in adsorption capacity below 70% RH.[221, 226] The adsorption capacity of TRHC shows 10× higher than silica gel and 100% improvement compared to composite desiccant at 90% RH. This intensive enhancement in adsorption might originate from the better water withholding capability of superabsorbent PNIPAAm gel. As shown in Figure 5.10, TRHC desiccant has outstanding superabsorbent capacity (3.9 ± 0.2 g/g at RT) at 97% RH. Interestingly, the isotherm EMC of the TRHC desiccant is similar to that of the $CaCl_2$ liquid desiccant because the vast majority of moisture uptake was contributed by the salt as confirmed by the low EMC (~0.3 g/g) in a reference dehydrated hydrogel matrix without salt loading (star symbol in Figure 5.10). Unlike the adsorption kinetics, the EMC is contributed by all the salts impregnated in the matrix, regardless of their locations (surface v.s. volume), because the salts will eventually make contacts with water given sufficiently long time and contribute to the adsorption capacity. This result suggests that we can fabricate a solid desiccant with same performance similar to that of liquid desiccant. This is enabled by the unique water storage mechanism offered by the hydrogel matrix, which behaves as liquid water but still preserves its solid state.

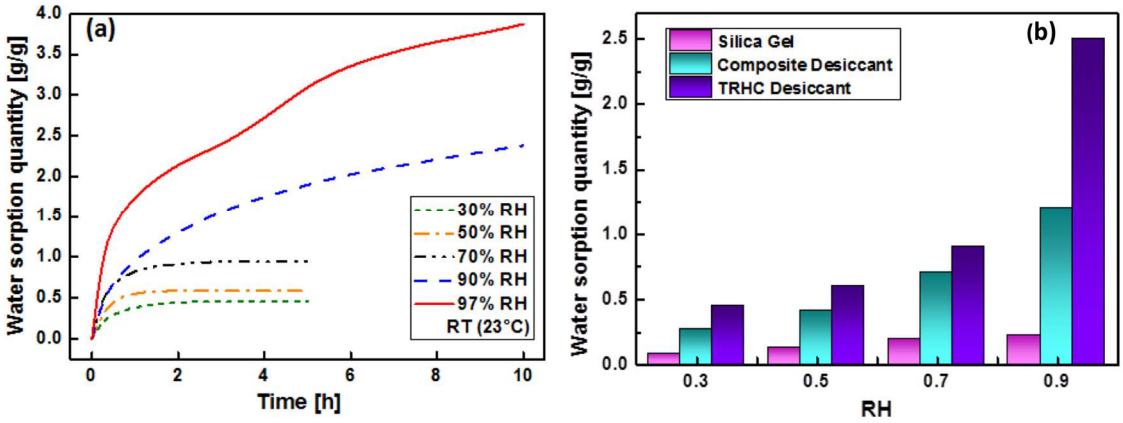

Figure 5.9. (a) Water adsorption quantity of TRHC desiccant at different relative humidity (RH). (b)Water sorption capacity of TRHC desiccant (at RT) and its comparison with silica gel[225] and composite desiccant[221, 226].

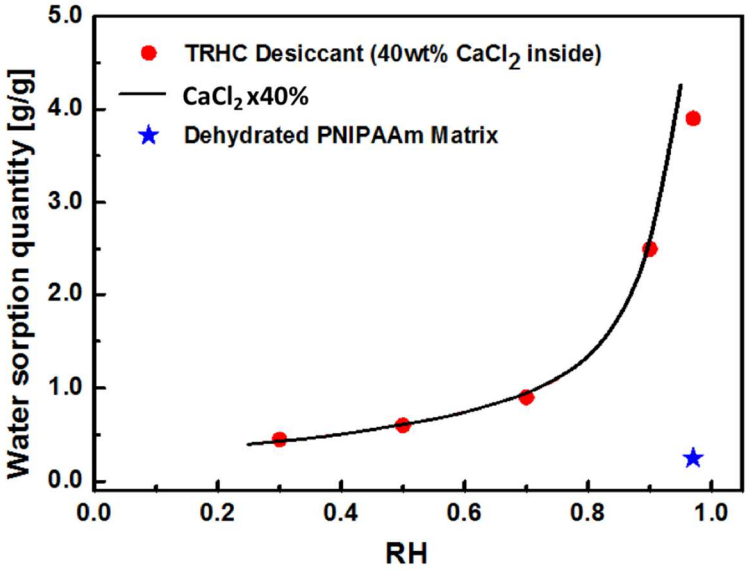

Figure 5.10. Isotherm of TRHC desiccant (at RT) and its comparison with a liquid desiccant (100 wt% $CaCl_2$ × 40%, black line). Blue star represents the dehydrated PNIAAm hydrogel matrix (without salt loading).

5.7 Adsorption Kinetics

Fick's law is examined to establish the mathematical model to describe the diffusion process in which the flux moves from the high concentration to low concentration. One dimensional Fick's 2nd law is represented by Equation 5.1.

$$\frac{\partial C}{\partial t} = D\frac{\partial^2 C}{\partial x^2} \quad (5.1)$$

Where, C is the concentration of moisture, t is time, D is the diffusivity, and x is the direction of moisture transfer. The TRHC desiccant is approximated as a plane sheet with a thickness δsince the thickness is much smaller than the sample size. Assuming a constant concentration on the surface of the TRHC desiccant throughout the adsorption, the initial and boundary conditions are:

i) $C = C_0$ at $x = 0$, $t > 0$

ii) $C = 0$ at $t = 0$,

iii) $\frac{\partial C}{\partial x} = 0$ at $x = \delta$

The solution is expressed as infinite series in Equation 5.2.

$$\frac{\Delta M(t)}{\Delta M_\infty} = 1 - \sum_{n=0}^{\infty} \frac{8}{(2n+1)^2\pi^2} exp\left[-D\left(n+\frac{1}{2}\right)^2 \frac{\pi^2}{\delta^2} t\right] \quad (5.2)$$

Where M(t) is the sample mass at time t, and M_∞ is the sample mass at infinite time. Thus, the diffusivity of TRHC desiccant during adsorption process can be modeled with the experimental results accordingly.

As shown in Figure 5.11, the absolute mass increase during adsorption for a TRHC desiccant with δ = 2 mm is plotted vs. time at RT and 80% RH. The mass increas is calculated with Equation 5.2 with n = 5 as shown in Figure 5.11. The yield effective diffusivity is 0.95×10^{-11} m^2/s as shown in Figure 5.12, which is higher than 6×10^{-11} m^2/s of the polymeric desiccant in Ref. [228] at 30°C and 80% RH and 3.41×10^{-11} m^2/s of silica

gel with particle size of 2 mm at 22°C and 76%RH in Ref. [203]. We attribute this slightly faster adsorption rate in our TRHC desiccant to its porous structure of sub-micron porous salt layer in Figure 5.2(f) and microporous PNIPAAm matrix in Figure 5.2(e), as well as better water affinity contributed by hygroscopic salt and hydrophilic polymer matrix.

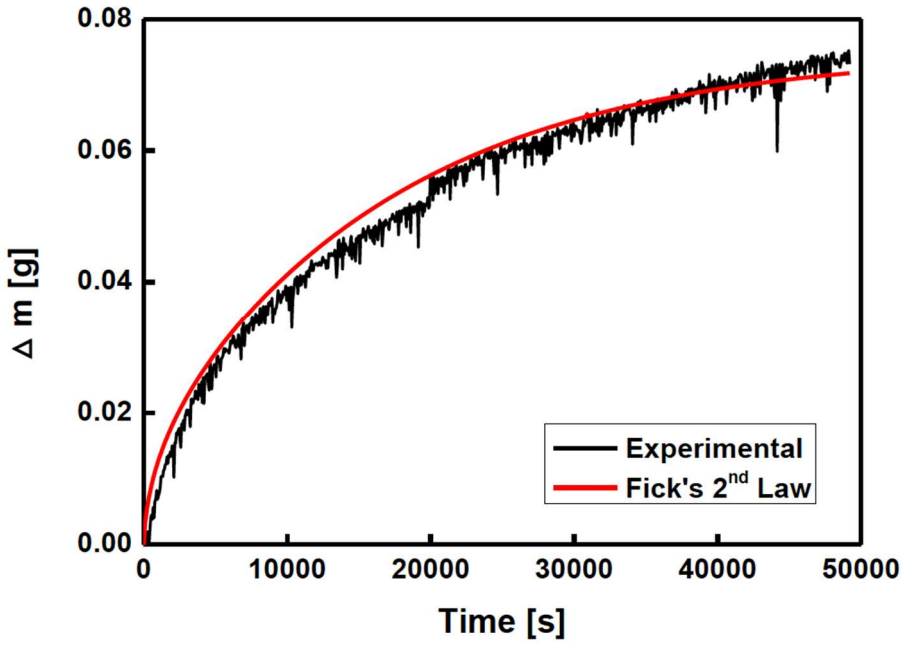

Figure 5.11. Mass increasement of TRHC desiccant (experimental vs. Fick's 2nd law) at RT and 80%RH.

As is well known, water vapor can diffuse through a porous medium by either ordinary diffusion or Knudsen diffusion, or sometimes, combinations of them.[227] The mean free path of water molecules is on the order of tens to hundreds of nanometers, which is much smaller than the mean pore diameter of TRHC desiccants (a few to hundreds of microns), and thus, ordinary diffusion is dominant in the TRHC desiccants. However, mean free path of water molecules is much greater than the mean pore diameter of silica gel (0.7 －3nm as shown earlier),[202] it means that collisions between a water molecule and the pore

wall are much more frequent than the collisions between the molecules (ordinary diffusion), and thus, Knudsen diffusion is the dominant diffusion at atmospheric pressure.

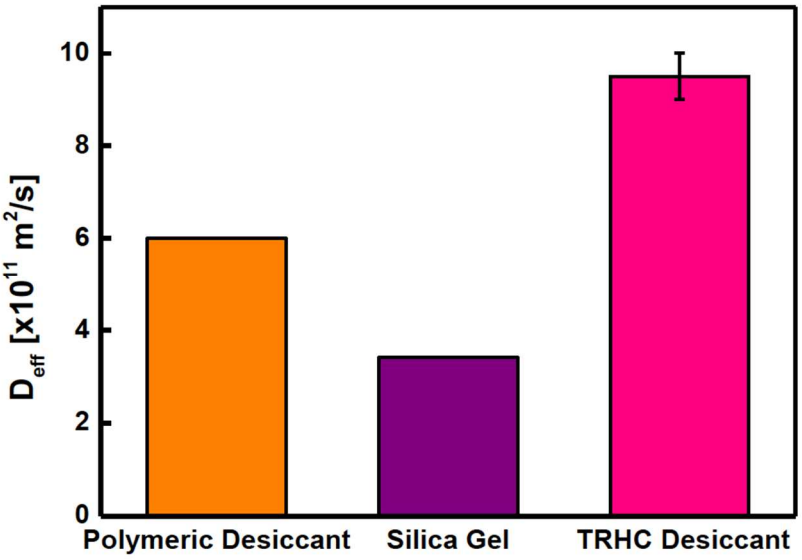

Figure 5.12. Comparison of diffusivity of TRHC desiccant, silica gel and polymeric desiccant.

5.8 Fast desorption at low regeneration temperature

Contrary to all the traditional solid desiccants that show a tradeoff between absorption and desorption, the superabsorbent TRHC desiccant offers a unique opportunity to facile moisture desorption through its hydrophilic-hydrophobic LCST phase transition. We tested the moisture desorption behavior at 50°C (above the LCST of ~32°C) and at RT (below the LCST), compared to a non-temperature responsive desiccant, for understanding the LCST contribution during desorption. After the room-temperature EMC uptake test at the highest humidity (97% RH, Figure 5.9(a)), the swollen TRHC samples were transferred to a 50°C environmental chamber with a controlled humidity (30% RH). The moisture desorption ratio results are shown in Figure 5.13. The non-temperature responsive were

synthesized following the same process shown in Figure 5.2 by replacing the thermo-responsive polymer matrix with non-temperature responsive ones (synthesized in Chapter 4). Below the LCST, the water desorption ratio at each time interval is similar to both TRHC desiccant and non-temperature responsive one. Above LCST, the water desorption ratio is similar within the first 20 minutes. However, the water desorption ratio of TRHC desiccant is higher compared to that of non-temperature responsive ones, which results in a 20% more water desorbed in TRHC desiccant compared to non-temperature responsive one in a 50-min desorption process. The water evaporation rates below/above LCST are calculated and shown in Figure 5.14 for both thermo-responsive and non-temperature responsive desiccant. When the temperature is below LCST, the evaporation rate of water is similar for both thermo-responsive and non-temperature responsive desiccant during the stage I because of the evaporation of water on the surface of porous matrix as shown in Figure 5.15. The rate is also similar to water evaporation rate both measured in Figure 5.15(a) and calculated (7.6×10^{-6} kg/s·m^2) at the same temperature and humidity. The calculated evaporation rate is based on the empirical evaporation of water from a water surface, like swimming pool. The amount of evaporated water can be expressed as

$$g_s = \frac{\Theta(x_s - x)}{3600} \quad (5.3)$$

where g_s = amount of evaporated water per second per area (kg/s·m^2), $\Theta = 25 + 19v$ = evaporation coefficient (kg/m^2·h), v = velocity of air above the water surface (m/s), x_s = maximum humidity ratio of saturated air at the same temperature as the water surface (kg/kg) (kg H_2O in kg dry air), x = humidity ratio air (kg/kg) (kg H_2O in kg dry Air).

Then the evaporation rate is slower down because of the liquid water transportation from stored inside the matrix to the porous matrix surface in Figure 5.15.

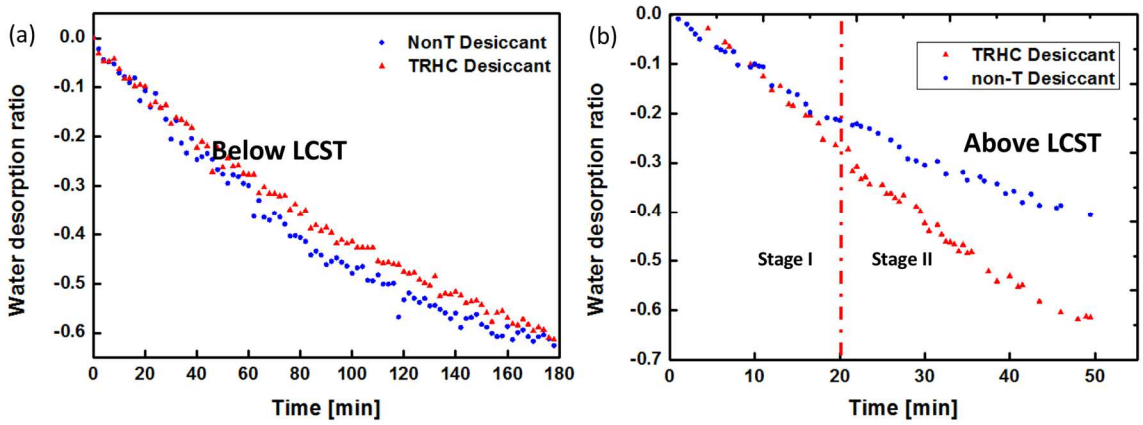

Figure 5.13. Water desorption ratio in TRHC desiccant and non-temperature responsive desiccant at 30% RH. (a) Below LCST; (b) Above LCST.

When the temperature is above LCST, the water evaporates at the similar rate in stage I for both desiccants with ~20% water removal. The calculated water evaporation rate based on empirical equation is 23.2×10^{-6} kg/s·m^2. The water evaporation rate in stage II keeps the same as in stage I for TRHC desiccant while the water evaporation rate continuously drops in stage II compared to that in stage I for non-temperature responsive desiccant. This faster evaporation rate of TRHC desiccant compared to that of non-temperature responsive ones during stage II results in ~20% more water removal as shown in Figure 5.13(b), contributing from the LCST behavior of thermo-responsive PNIPAAm matrix in Figure 5.15(b). The evaporation rate of the TRHC desiccant starts to drop after stage II also because the liquid water transportation as discussed in Figure 5.13(a).

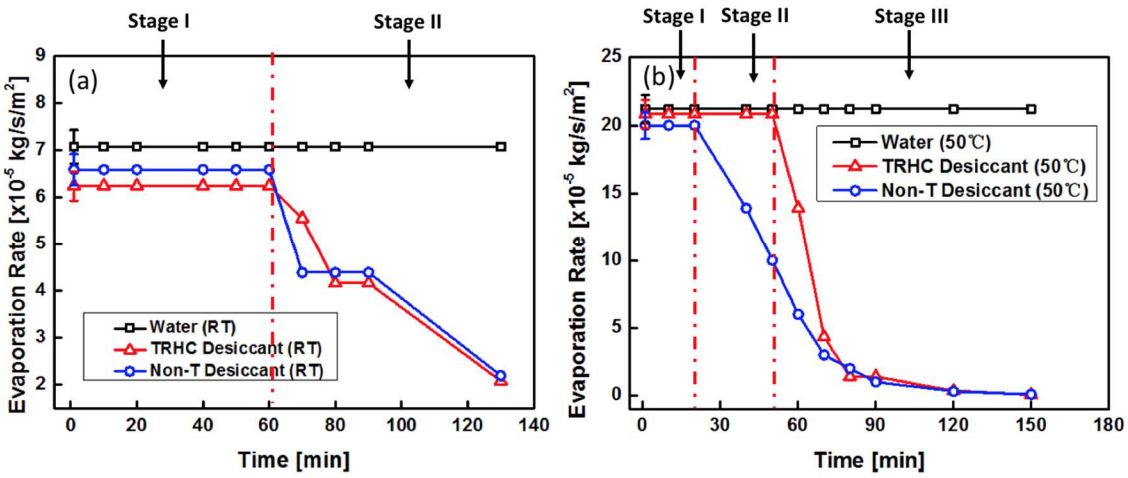

Figure 5.14. Evaporation rate of water in TRHC desiccant and non-temperature responsive desiccant at 30% RH. (a) Below LCST. (b) Above LCST.

This faster evaporation of water above LCST from TRHC desiccant, compared to non-temperature responsive one in stage II, originates from the hydrophobicity of thermo-responsive PNIPAAm matrix after the LCST phase transition. PNIPAAm hydrogel has two parts: hydrophilic amide group (－CONH－) and hydrophobic part (－R－). As the temperature reaches the LCST of NIPAAm during the desorption, the interaction among the hydrophobic part will be stronger, while the hydrogen bonds between the hydrophilic part and moisture become weaker, thus shrinking the polymer due to inter-polymer chain association. The absorbed water was then squeezed out to the porous matrix surface during the desorption process, which can be easily evaporated at a relatively low regeneration temperature (Figure 5.13(b) and Figure 5.14(b)).

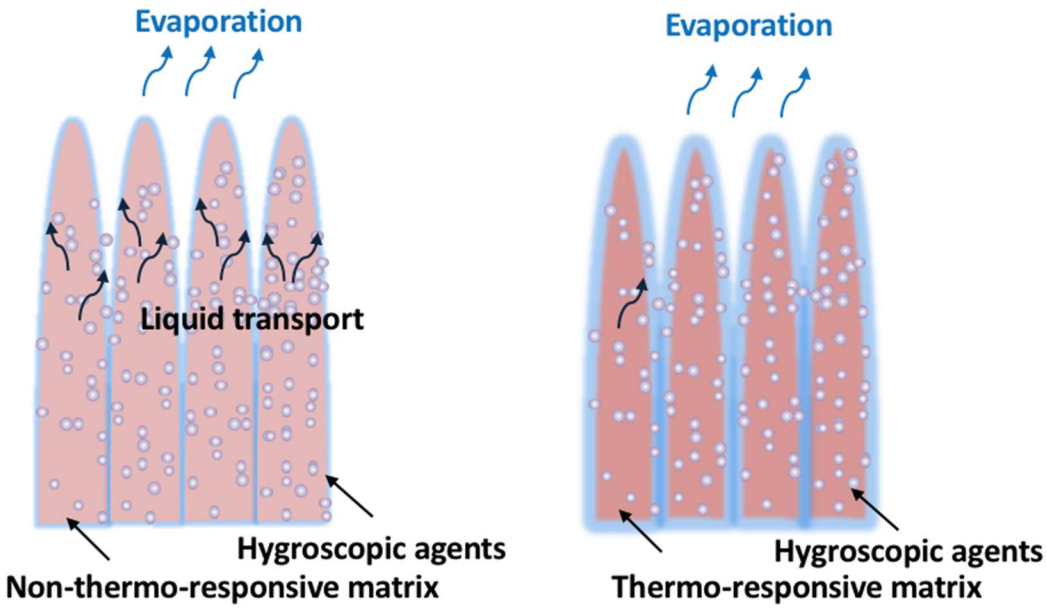

Figure 5.15. Evaporation rate of water in TRHC desiccant and non-temperature responsive desiccant at 30% RH and 50°C.

A comparison of water adsorption quantity and regeneration temperature of the state-of-the-art solid desiccants is summarized in Figure 5.16. It can be seen that composite desiccants have improved water sorption capacity with the support of SIM structure, i.e., silica gel based composite desiccant with adsorption capacity of 0.76 g/g. In addition, metal-organic framework were proven to have high sorption capability (~1.7 g/g).[229] However, the existing state-of-art desiccants have a higher regeneration temperature (>80°C, higher than over 50% of industrial waste heat), to match their high adsorption capacities because of the fixed affinity to water. TRHC desiccant synthesized here possesses both high absorption capacity and low regeneration temperature for the first time. This new class of material has the potential to greatly improve the performance of the dehumidification system, enabling clean and economical air conditioning which can result in significant savings in electric power consumption by utilizing waste heat and solar

energy, and avoiding pollution by chlorofluorocarbons used in vapor-compression air conditioning systems.

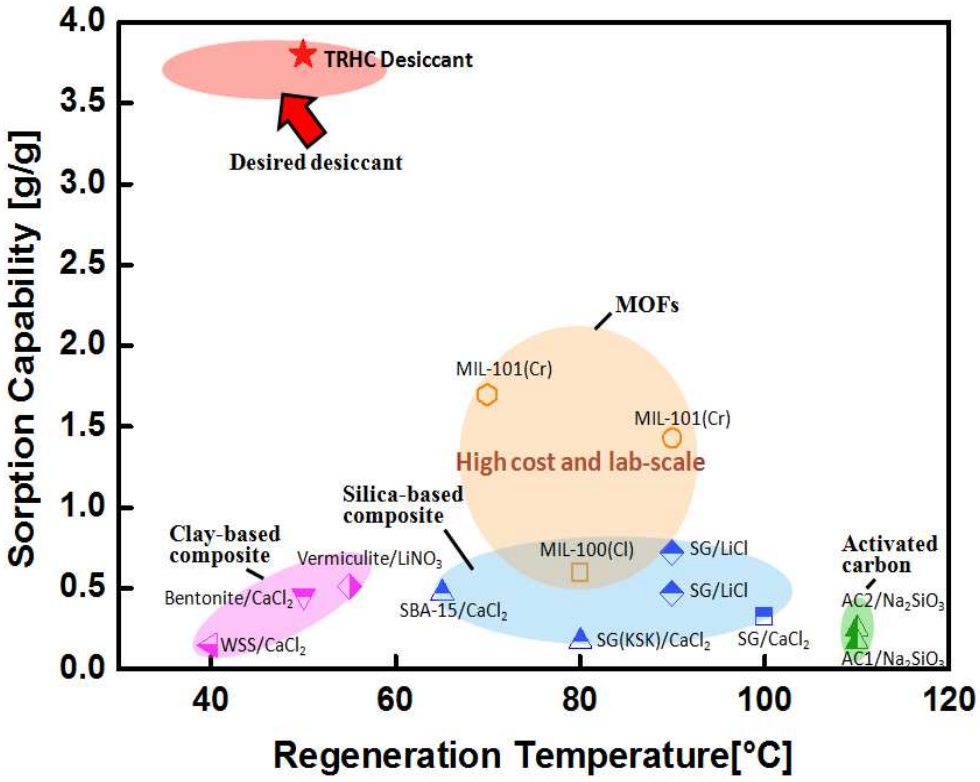

Figure 5.16. Water sorption capability and regeneration temperature of state-of-art solid desiccants.[51] TRHC desiccant shows both high adsorption capacity and low regeneration temperature for the first time as desired for desired desiccants.

5.9 Thermodynamic model of desiccant assisted air conditioning with TRHC desiccant

A thermodynamic modeling in Figure 5.17 is built up to study feasibility of using TRHC desiccant for high coefficient of performance (COP) of SDC systems.[230] The SDC system is composed of desiccant wheel, energy conservation wheel (ECW), direct evaporative cooling (DEC) and heat source. As the schematic diagram shown in Figure 5.17(a), the mixture of the outdoor air and return air flows through the dehumidifier,

transferring latent heat to sensible heat, and is cooled by an ECW and DEC before supplying to the conditioned room in thermal conditions to the human thermal comfort (process 0-1-2-3-4 in Figure 5.17(a)). Its psychrometric process is shown in Figure 5.17(b). The reactivation air stream is also composed by a mixture of outdoor and return air. After passing through DEC and ECW, it is instantly heated by a heat source, e.g., industrial waste heat or solar energy, and flows through the dehumidifier for desiccant regeneration by removing moisture (reactivation process 5－6－7－8－9). The operational parameters of modeling are described in Ref. [230]. By applying TRHC desiccant (regeneration temperature ~55°C) to dehumidifier of SDC systems, the COP is 6.03 as shown in Figure 5.17(c), which is 10 times higher than that of using silica gel (COP is 0.55[230] with regeneration temperature of 115°C). The COP is also improved for nearly 5 times by TRHC desiccant compared to other SIM desiccants and even liquid desiccants.[50] This high COP by utilization of TRHC desiccant is comparable with that of commercial VC systems ranging from 2.8 to 4.8. The bulky SDC system thus can be reduced and feasible for application. Meanwhile, with the extremely low regeneration temperature, lots of low grade thermal energy can be used as heat source, which saves lots of electric power consumption and avoids CFCs pollution.

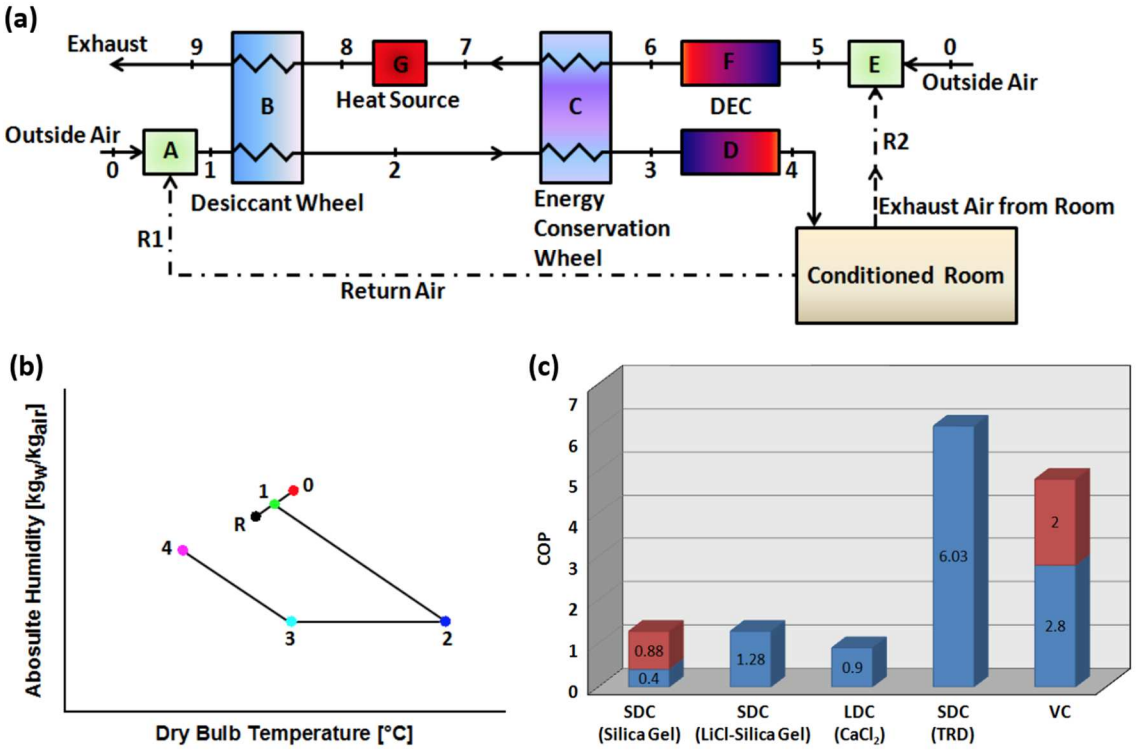

Figure 5.17. (a) Schematic modeling diagram of desiccant cooling system (A: mixer and fan of the process air; B: desiccant dehumidifier type rotary wheel; C: energy conservation wheel; D: direct evaporative cooler; E: mixer and fan of the reactivation air; F: direct evaporative cooler; G: source of reactivation energy). (b) Psychometric chart representation for a typical operation. (c) Comparison of COP between solid desiccant cooling (silica gel, composite desiccant and TRHC desiccant), liquid desiccant cooling and vapor compression cooling.

5.10 Conclusions

In summary, we developed a solid desiccant based on porous thermo-responsive PNIPAAm hydrogel matrix that uniquely possesses both high-capacity adsorption and fast low-temperature desorption. The solid thermo-responsive hydrogel composite (TRHC) has a high adsorption capacity owing to the large surface area offered by the porous hydrogel matrix for more hygroscopic salt loading. The adsorption behavior is similar to that of a liquid desiccant, but the desiccant still maintains the solid-like form due to the water-holding capacity of the superabsorbent hydrogel matrix. Meanwhile, low regeneration

temperature (~50°C) is achieved, thanks to the unique phase transition from hydrophilicity to hydrophobocity of the thermo-responsive PNIPAAm matrix undergoing its lower critical solution temperature (LCST ~32°C). This novel desiccant can find potential applications in a variety of fields, such as oilfields,[231] HVAC industries,[232] and water harvesting.[233]

Chapter 5, in part, is in a manuscript in preparation, 2018. Shuang Cui, Jian Zeng, Patrick Charles, Evan Muller, and Renkun Chen. The dissertation author was the first author of this paper.

Chapter 6 Conclusions and Future work

6.1 Conclusions

The development of new source of sustainable and clean energy, as well as novel technologies with less energy consumption are both required facing the energy crisis. This dissertation presented the thermal transport and transformation in tungsten (W), a plasma facing material in nuclear fusion reactor as well as superabsorbent polymeric material for energy-efficient building cooling.

To study the near-surface regime of W under fusion relevant conditions, an improved 3ω technique with higher measurement sensitivity was developed to study the thermal conductivity of W with the extremely thin (~ a few tens of nm thick) thickness by He-plasma irradiation, less damage level (10^{-3} or 10^{-2} dpa) by Cu ion irradiation and high temperature Cu/W ion irradiation.

We investigated the dosage and irradiation temperature dependence on thermal conductivity (κ) of W under fusion-relevant radiation conditions by using an improved 3ω technique. Our results show a significant reduction in κ for W irradiated at room temperature with energetic (MeV) heavy ions. The damage, quantified by displacement per atom (dpa), spanned from 10^{-3} to 0.6 dpa for Cu ions and 0.2 dpa for W ions. With increasing Cu ion damage level, κ decreased and reached a minimum of 52 ± 13.6 W/m·K at 0.6 dpa, ~30% of κ for pristine W. When the ion irradiation was performed at 1000 K, which is a temperature that is sufficiently high to induce significant dynamic annealing in W, κ was largely recovered to around 80% of the pristine value. We attribute this κ recovery to the thermal annealing and annihilation of the irradiation induced defects, i.e., through

vacancy/self-interstitial atom (SIA) recombination. This finding is consistent with our prior observation of defect recovery probed by deuterium retention.

The thermal conductivity of W surface layers damaged by He plasma in PISCES at UCSD were also investigated. We studied the damage effect on both bulk, and thin film, W. We observed that the surface morphology of both bulk and thin film was altered after exposure to He plasma with the fluence of 1×10^{26} m^{-2} (bulk) and 2×10^{24} m^{-2} (thin film). Transmission electron microscopy (TEM) analysis reveals that the depth of the irradiation damaged layer was approximately 20 nm on the bulk W exposed to He plasma at 773 K for 2000 s. For the damaged W thin film sample, we measured the reduction in electrical conductivity and used the Wiedemann-Franz (W-F) law to extract the thermal conductivity. Results from both measurements show that thermal conductivity in the damaged layers was reduced by at least ~80% compared to that of undamaged W. This large reduction in thermal conductivity can be attributed to the scattering of electrons, the dominant heat carriers in W, caused by defects introduced by He-plasma irradiation.

The near-surface region of plasma facing material (PFM) plays an important role in thermal management of fusion reactors. Therefore, studying the effects of radiation damage on tungsten (W), a primary candidate material for plasma facing components (PFCs), is of great significance in the thermal management of future fusion reactors. Our investigation of W under ion irradiation and He-plasma irradiation offers insights in selecting operational conditions in future fusion reactor designs.

Meanwhile, we report, for the first time, the application of highly stretchable and tough double network hydrogels (DN-Gels) as durable and reusable ‘sweating skins’ for cooling buildings. These DN-Gels demonstrate outstanding cooling performance, reducing

the top roof surface temperature of wooden house models by 25－30°C for up to 7 hours after only a single water hydration charge. More importantly, compared with single network hydrogels (SN-Gels) previously studied for cooling applications, these DN-Gels exhibit extraordinary toughness and cyclability due to their interpenetrated ionically and covalently cross-linked networks, as demonstrated by constant cooling performance over more than 50 cycles. This excellent cyclability is further demonstrated by the unaltered mechanical properties and charging capability of the hydrogels after many cycles, compared to fresh ones. By coating a 100 m^2 roof of a single house with tough DN-Gels, it is estimated that the annual electricity consumption needed for air conditioning can be reduced by ~290 kWh with associated CO_2 emission reductions of 160 kg. Our results suggest that bio-inspired sweat cooling, specifically using tough DN-Gel coatings, represents a promising energy-efficient technology for cooling buildings as well as other devices and systems.

A thermo-responsive hydrogel composite (TRHC) desiccant with drastically different affinities to water upon phase transition is also developed, unlike typical solid desiccant with a tradeoff between its adsorption and desorption kinetics due to its fixed affinity to adsorbates, achieving high adsorption capacity and fast desorption at low regeneration temperature. The solid TRHC desiccant is synthesized by impregnating hygroscopic salt ($CaCl_2$) into porous Poly(N-isopropylacrylamide) (PNIPAAm) hydrogel matrix serving as water withholding medium. It shows high adsorption capacity of ~3.8 g/g (room temperature and 97% relative humidity (RH)), originating from the hydrophilicity and the high porosity of the PNIPAAm matrix to hold more salts as hygroscopic agents. Moreover, TRHC desiccant exhibits fast desorption kinetics with

~60% of water removal within 50 minutes (50°C and 30% RH). This fast desorption benefits from the thermo-responsiveness of the PNIPAAm matrix which becomes hydrophobic above its lower critical solution temperature (LCST, ~32°C) and results in polymer shrinkage for facile water release for evaporation. The unique high adsorption capacity and superfast desorption at a low regeneration temperature makes the TRHC desiccant attractive for a variety of applications, such as desiccant cooling and adsorption heat pump.

6.2 Future work

For studying thermal conductivity reduction and recovery in heavy ion irradiated W, it would be interesting to study the thermal conductivity of a series of ion irradiated W under different temperature implantation because the different types of defects format and change at different temperature. The recovery behavior of displacement damage, such as dislocation loops, and other defect structures (self-interstitial atoms (SIAs), vacancy clusters and voids), were well discussed in Ref. [66] with transmission electron microscopy (TEM) analysis under different post and in-situ annealing temperature. The dynamic annealing experiment at 1000 K here belongs to stage IV (773－1173K) recovery as five stages of annealing common to BCC metals identified by Tompson,[234] generally attributing to vacancy-self interstitial complexes.[235]

The obvious increase in average loop size with increasing temperature particularly happens between 1073 K and 1223 K.[66] Besides, the vacancies produced by ion irradiation was presumed to be in the form of vacancy clusters which could not be reliably sized using TEM (< 1 nm diameter).[236] Although the void became visible at 1073 K, no obvious change

in size appears until 1373 K. Considering the dynamic annealing temperature (1000 K) and short annealing time (< 50 min), less contribution from larger defect size is expected and more annihilation of defects is expected as discussed in Ref. [85] with a decreased deuterium retention by both thermal desorption spectroscopy (TDS) and nuclear reaction analysis (NRA). But it would be of significance to study the effect of higher ion implantation temperature (> 1000 K) on the thermal conductivity of the damaged W because the W armors are supposed to experience the temperature of 373 K to 1273 K in ITER.[85]

The recyclability of TRHC desiccant is one of the main concern in the application of desiccant assisted air conditioning because the possible leakage of excess liquid desiccant. One approach to solve this issue is to substitute the inorganic hygroscopic liquid desiccant with organic hygroscopic salt, for example, sodium polyacrylate. Large concentration of organic salt is needed for high adsorption capacity of TRHC desiccant. However, it might also change the LCST of thermo-responsive hydrogel outside of the favorable window of 30—40℃ because increasing the mixing enthalpy. The LCST usually is increased because the additive hygroscopic polymer is usually hydrophilic. Increasing the number of hydrophilic side chain increases the change of mixing enthalpy (ΔH_{mix}), due to larger number of hydrogen-bonding, and thus increases LCST. In order to bring the LCST back to this window, the intrinsic LCST of the TRHC desiccant with organic salt should be modified. One method is to increase the number of hydrophobic side chain to increase the change of mixing entropy (ΔS_{mix}), and thus decreases LCST. Besides the application of desiccant assisted cooling, TRHC desiccant with better cyclability would also be a good candidate for water harvesting from moist air due to its strong affinity to

water and low thermal energy requirement for direct water release without condensation, benefiting from LCST behavior, which is of great importance for alleviating water scarcity problem.

References

1. Dovì, V. G.; Friedler, F.; Huisingh, D.; Klemeš, J. J., Cleaner energy for sustainable future. *Journal of Cleaner Production* **2009,** *17* (10), 889-895.

2. Diedrich, A.; Upham, P.; Levidow, L.; van den Hove, S., Framing environmental sustainability challenges for research and innovation in European policy agendas. *Environmental Science & Policy* **2011,** *14* (8), 935-939.

3. Van Vuuren, D.; Nakicenovic, N.; Riahi, K.; Brew-Hammond, A.; Kammen, D.; Modi, V.; Nilsson, M.; Smith, K., An energy vision: the transformation towards sustainability—interconnected challenges and solutions. *Current Opinion in Environmental Sustainability* **2012,** *4* (1), 18-34.

4. Swan, L. G.; Ugursal, V. I., Modeling of end-use energy consumption in the residential sector: A review of modeling techniques. *Renewable and sustainable energy reviews* **2009,** *13* (8), 1819-1835.

5. Santoyo-Castelazo, E.; Azapagic, A., Sustainability assessment of energy systems: integrating environmental, economic and social aspects. *Journal of Cleaner Production* **2014,** *80*, 119-138.

6. Cao, X.; Dai, X.; Liu, J., Building energy-consumption status worldwide and the state-of-the-art technologies for zero-energy buildings during the past decade. *Energy and buildings* **2016,** *128*, 198-213.

7. Knaster, J.; Moeslang, A.; Muroga, T., Materials research for fusion. *Nature Physics* **2016,** *12* (5), 424.

8. Wigner, E., Theoretical physics in the metallurgical laboratory of Chicago. *Journal of Applied Physics* **1946,** *17* (11), 857-863.

9. Robinson, M. T., Basic physics of radiation damage production. *Journal of nuclear materials* **1994,** *216*, 1-28.

10. Zinkle, S., 1.03-Radiation-Induced effects on microstructure. *Comprehensive nuclear materials* **2012,** *1*, 65-98.

11. Nordlund, K.; Zinkle, S.; Suzudo, T.; Averback, R.; Meinander, A.; Granberg, F.; Malerba, L.; Stoller, R.; Banhart, F.; Weber, B., Primary radiation damage in materials: review of current understanding and proposed new standard displacement damage model to incorporate in-cascade mixing and defect production efficiency effects. *Report No. NEA-NSC-DOC-2015-9* **2015**.

12. Lindhard, J.; Winther, A., *Stopping power of electron gas and equipartition rule*. Munksgaard: 1964.

13. Ziegler, J.; Littmark, U.; Biersack, J., Calculation using the stopping and range of ions in matter (SRIM) code. 2008.

14. Parkin, D. M.; Coulter, C. A., Displacement cascades in polyatomic materials. *Journal of Nuclear Materials* **1983,** *117*, 340-344.

15. Muroga, T.; Kitajima, K.; Ishino, S., The effect of recoil energy spectrum on cascade structures and defect production efficiencies. *Journal of nuclear materials* **1985,** *133*, 378-382.

16. Rieth, M.; Dudarev, S.; De Vicente, S. G.; Aktaa, J.; Ahlgren, T.; Antusch, S.; Armstrong, D.; Balden, M.; Baluc, N.; Barthe, M.-F., Recent progress in research on tungsten materials for nuclear fusion applications in Europe. *Journal of Nuclear Materials* **2013,** *432* (1-3), 482-500.

17. Loewenhoff, T.; Bürger, A.; Linke, J.; Pintsuk, G.; Schmidt, A.; Singheiser, L.; Thomser, C., Evolution of tungsten degradation under combined high cycle edge-localized mode and steady-state heat loads. *Physica Scripta* **2011,** *2011* (T145), 014057.

18. Makhlaj, V.; Garkusha, I.; Malykhin, S.; Pugachov, A.; Landman, I.; Linke, J.; Pestchanyi, S.; Chebotarev, V.; Tereshin, V., Residual stresses in tungsten under exposures with ITER ELM-like plasma loads. *Physica scripta* **2009,** *2009* (T138), 014060.

19. Hirai, T.; Pintsuk, G.; Linke, J.; Batilliot, M., Cracking failure study of ITER-reference tungsten grade under single pulse thermal shock loads at elevated temperatures. *Journal of Nuclear Materials* **2009,** *390*, 751-754.

20. Oya, Y.; Shimada, M.; Kobayashi, M.; Oda, T.; Hara, M.; Watanabe, H.; Hatano, Y.; Calderoni, P.; Okuno, K., Comparison of deuterium retention for ion-irradiated and neutron-irradiated tungsten. *Physica Scripta* **2011,** *2011* (T145), 014050.

21. Linke, J. M.; Hirai, T.; Rödig, M.; Singheiser, L. A., Performance of plasma-facing materials under intense thermal loads in tokamaks and stellarators. *Fusion science and technology* **2004,** *46* (1), 142-151.

22. Hirai, T.; Ezato, K.; Majerus, P., ITER relevant high heat flux testing on plasma facing surfaces. *Materials Transactions* **2005,** *46* (3), 412-424.

23. Bergman, T. L.; Incropera, F. P.; DeWitt, D. P.; Lavine, A. S., *Fundamentals of heat and mass transfer*. John Wiley & Sons: 2011.

24. Dechaumphai, E.; Barton, J. L.; Tesmer, J. R.; Moon, J.; Wang, Y.; Tynan, G. R.; Doerner, R. P.; Chen, R., Near-surface thermal characterization of plasma facing components using the 3-omega method. *Journal of Nuclear Materials* **2014,** *455* (1-3), 56-60.

25. Fujitsuka, M.; Tsuchiya, B.; Mutoh, I.; Tanabe, T.; Shikama, T., Effect of neutron irradiation on thermal diffusivity of tungsten–rhenium alloys. *Journal of nuclear materials* **2000,** *283*, 1148-1151.

26. Roedig, M.; Kuehnlein, W.; Linke, J.; Pitzer, D.; Merola, M.; Rigal, E.; Schedler, B.; Visca, E., Post irradiation testing of samples from the irradiation experiments PARIDE 3 and PARIDE 4. *Journal of nuclear materials* **2004,** *329*, 766-770.

27. Peacock, A.; Barabash, V.; Dänner, W.; Rödig, M.; Lorenzetto, P.; Marmy, P.; Merola, M.; Singh, B.; Tähtinen, S.; Van Der Laan, J., Overview of recent European materials R&D activities related to ITER. *Journal of nuclear materials* **2004,** *329*, 173-177.

28. Tanno, T.; Hasegawa, A.; He, J.; Fujiwara, M.; Satou, M.; Nogami, S.; Abe, K.; Shishido, T., Effects of transmutation elements on the microstructural evolution and electrical resistivity of neutron-irradiated tungsten. *Journal of Nuclear Materials* **2009,** *386*, 218-221.

29. Khafizov, M.; Yablinsky, C.; Allen, T. R.; Hurley, D. H., Measurement of thermal conductivity in proton irradiated silicon. *Nuclear Instruments and Methods in Physics Research Section B: Beam Interactions with Materials and Atoms* **2014,** *325*, 11-14.

30. Pakarinen, J.; Khafizov, M.; He, L.; Wetteland, C.; Gan, J.; Nelson, A. T.; Hurley, D. H.; El-Azab, A.; Allen, T. R., Microstructure changes and thermal conductivity reduction in UO 2 following 3.9 MeV He 2+ ion irradiation. *Journal of Nuclear Materials* **2014,** *454* (1), 283-289.

31. Eichler, H. J.; Günter, P.; Pohl, D. W., *Laser-induced dynamic gratings*. Springer: 2013; Vol. 50.

32. Hofmann, F.; Mason, D. R.; Eliason, J. K.; Maznev, A. A.; Nelson, K. A.; Dudarev, S. L., Non-contact measurement of thermal diffusivity in ion-implanted nuclear materials. *Scientific reports* **2015,** *5*, 16042.

33. Rosencwaig, A.; Opsal, J.; Smith, W. L.; Willenborg, D., Detection of thermal waves through optical reflectance. *Applied Physics Letters* **1985,** *46* (11), 1013-1015.

34. Qu, S.; Li, Y.; Wang, Z.; Jia, Y.; Li, C.; Xu, B.; Chen, W.; Bai, S.; Huang, Z.; Tang, Z., Thermal conductivity measurement of the He-ion implanted layer of W using transient thermoreflectance technique. *Journal of Nuclear Materials* **2017,** *484*, 382-385.

35. Käding, O.; Skurk, H.; Maznev, A.; Matthias, E., Transient thermal gratings at surfaces for thermal characterization of bulk materials and thin films. *Applied Physics A* **1995,** *61* (3), 253-261.

36. Hofmann, F.; Nguyen-Manh, D.; Gilbert, M.; Beck, C.; Eliason, J.; Maznev, A.; Liu, W.; Armstrong, D.; Nelson, K.; Dudarev, S., Lattice swelling and modulus change in

a helium-implanted tungsten alloy: X-ray micro-diffraction, surface acoustic wave measurements, and multiscale modelling. *Acta Materialia* **2015,** *89*, 352-363.

37. Cahill, D. G., Thermal conductivity measurement from 30 to 750 K: the 3ω method. *Review of scientific instruments* **1990,** *61* (2), 802-808.

38. Kim, J. H.; Feldman, A.; Novotny, D., Application of the three omega thermal conductivity measurement method to a film on a substrate of finite thickness. *Journal of applied physics* **1999,** *86* (7), 3959-3963.

39. Cappelli, L.; Guallart, V., *Self sufficient city: envisioning the habitat of the future, 3rd. Advanced Architecture Contest*. Institute for Advanced Architecture of Catalonia Hewlett-Packard Company: 2010.

40. Rafique, M. M.; Gandhidasan, P.; Rehman, S.; Al-Hadhrami, L. M., A review on desiccant based evaporative cooling systems. *Renewable and Sustainable Energy Reviews* **2015,** *45*, 145-159.

41. Davanagere, B.; Sherif, S.; Goswami, D., A feasibility study of a solar desiccant air‐conditioning system−Part II: Transient simulation and economics. *International Journal of Energy Research* **1999,** *23* (2), 103-116.

42. Alvarado, J. L.; Terrell Jr, W.; Johnson, M. D., Passive cooling systems for cement-based roofs. *Building and Environment* **2009,** *44* (9), 1869-1875.

43. Cheikh, H. B.; Bouchair, A., Passive cooling by evapo-reflective roof for hot dry climates. *Renewable Energy* **2004,** *29* (11), 1877-1886.

44. Chan, H.-Y.; Riffat, S. B.; Zhu, J., Review of passive solar heating and cooling technologies. *Renewable and Sustainable Energy Reviews* **2010,** *14* (2), 781-789.

45. Meng, Q.; Hu, W., Roof cooling effect with humid porous medium. *Energy and Buildings* **2005,** *37* (1), 1-9.

46. Artmann, N.; Manz, H.; Heiselberg, P., Climatic potential for passive cooling of buildings by night-time ventilation in Europe. *Applied energy* **2007,** *84* (2), 187-201.

47. Zhou, G.; Yang, Y.; Wang, X.; Zhou, S., Numerical analysis of effect of shape-stabilized phase change material plates in a building combined with night ventilation. *Applied Energy* **2009,** *86* (1), 52-59.

48. Synnefa, A.; Santamouris, M.; Akbari, H., Estimating the effect of using cool coatings on energy loads and thermal comfort in residential buildings in various climatic conditions. *Energy and Buildings* **2007,** *39* (11), 1167-1174.

49. Joudi, A.; Svedung, H.; Cehlin, M.; Rönnelid, M., Reflective coatings for interior and exterior of buildings and improving thermal performance. *Applied energy* **2013,** *103*, 562-570.

50. Jia, C.; Dai, Y.; Wu, J.; Wang, R., Use of compound desiccant to develop high performance desiccant cooling system. *International Journal of Refrigeration* **2007,** *30* (2), 345-353.

51. Zheng, X.; Ge, T.; Wang, R., Recent progress on desiccant materials for solid desiccant cooling systems. *Energy* **2014,** *74*, 280-294.

52. Ge, T.; Dai, Y.; Wang, R., Review on solar powered rotary desiccant wheel cooling system. *Renewable and Sustainable Energy Reviews* **2014,** *39*, 476-497.

53. Buker, M. S.; Riffat, S. B., Recent developments in solar assisted liquid desiccant evaporative cooling technology—a review. *Energy and Buildings* **2015,** *96*, 95-108.

54. Zhang, J.; Ge, T.; Dai, Y.; Zhao, Y.; Wang, R., Experimental investigation on solar powered desiccant coated heat exchanger humidification air conditioning system in winter. *Energy* **2017**.

55. Ahmed, M.; Kattab, N.; Fouad, M., Evaluation and optimization of solar desiccant wheel performance. *Renewable Energy* **2005,** *30* (3), 305-325.

56. Collier Jr, R., Desiccant properties and their effect on cooling system performance. *ASHRAE transactions* **1989,** *95*, 823-827.

57. Cuce, P. M., Thermal performance assessment of a novel liquid desiccant-based evaporative cooling system: An experimental investigation. *Energy and Buildings* **2017,** *138*, 88-95.

58. She, X.; Yin, Y.; Zhang, X., Thermodynamic analysis of a novel energy-efficient refrigeration system subcooled by liquid desiccant dehumidification and evaporation. *Energy conversion and management* **2014,** *78*, 286-296.

59. Panaras, G.; Mathioulakis, E.; Belessiotis, V., Solid desiccant air-conditioning systems–design parameters. *Energy* **2011,** *36* (5), 2399-2406.

60. Nóbrega, C. E. L.; Brum, N. C. L., An introduction to solid desiccant cooling technology. In *Desiccant-Assisted Cooling*, Springer: 2014; pp 1-23.

61. Daou, K.; Wang, R.; Xia, Z., Desiccant cooling air conditioning: a review. *Renewable and Sustainable Energy Reviews* **2006,** *10* (2), 55-77.

62. Pitts, R.; Carpentier, S.; Escourbiac, F.; Hirai, T.; Komarov, V.; Lisgo, S.; Kukushkin, A.; Loarte, A.; Merola, M.; Naik, A. S., A full tungsten divertor for ITER: Physics issues and design status. *Journal of Nuclear Materials* **2013,** *438*, S48-S56.

63. Philipps, V., Tungsten as material for plasma-facing components in fusion devices. *Journal of nuclear materials* **2011,** *415* (1), S2-S9.

64. Hirai, T.; Escourbiac, F.; Carpentier-Chouchana, S.; Fedosov, A.; Ferrand, L.; Jokinen, T.; Komarov, V.; Kukushkin, A.; Merola, M.; Mitteau, R., ITER tungsten divertor design development and qualification program. *Fusion Engineering and Design* **2013,** *88* (9-10), 1798-1801.

65. Barabash, V.; Federici, G.; Linke, J.; Wu, C., Material/plasma surface interaction issues following neutron damage. *Journal of Nuclear Materials* **2003,** *313*, 42-51.

66. Ferroni, F.; Yi, X.; Arakawa, K.; Fitzgerald, S. P.; Edmondson, P. D.; Roberts, S. G., High temperature annealing of ion irradiated tungsten. *Acta Materialia* **2015,** *90*, 380-393.

67. Zinkle, S. J.; Was, G., Materials challenges in nuclear energy. *Acta Materialia* **2013,** *61* (3), 735-758.

68. Khafizov, M.; Chauhan, V.; Wang, Y.; Riyad, F.; Hang, N.; Hurley, D., Investigation of thermal transport in composites and ion beam irradiated materials for nuclear energy applications. *Journal of Materials Research* **2017,** *32* (1), 204-216.

69. Cheaito, R.; Gorham, C. S.; Misra, A.; Hattar, K.; Hopkins, P. E., Thermal conductivity measurements via time-domain thermoreflectance for the characterization of radiation induced damage. *Journal of Materials Research* **2015,** *30* (9), 1403-1412.

70. Armstrong, D.; Hardie, C.; Gibson, J.; Bushby, A.; Edmondson, P.; Roberts, S., Small-scale characterisation of irradiated nuclear materials: Part II nanoindentation and micro-cantilever testing of ion irradiated nuclear materials. *Journal of Nuclear Materials* **2015,** *462*, 374-381.

71. Nelson, R.; Mazey, D.; Hudson, J., The use of ion accelerators to simulate fast neutron-induced voidage in metals. *Journal of Nuclear Materials* **1970,** *37* (1), 1-12.

72. Toloczko, M. B.; Garner, F.; Voyevodin, V.; Bryk, V.; Borodin, O.; Mel'Nychenko, V.; Kalchenko, A., Ion-induced swelling of ODS ferritic alloy MA957 tubing to 500dpa. *Journal of Nuclear Materials* **2014,** *453* (1), 323-333.

73. Was Gary, S., Fundamentals of Radiation Materials Science. Berlin Heidelberg: Springer: 2007.

74. Yi, X.; Jenkins, M. L.; Kirk, M. A.; Zhou, Z.; Roberts, S. G., In-situ TEM studies of 150 keV W+ ion irradiated W and W-alloys: Damage production and microstructural evolution. *Acta Materialia* **2016,** *112*, 105-120.

75. Ogorodnikova, O.; Płociński, T.; Andrzejczuk, M.; Rasiński, M.; Mayer, M.; Kurzydłowski, K., TEM observations of radiation damage in tungsten irradiated by 20 MeV W ions. *Nuclear Instruments and Methods in Physics Research Section B: Beam Interactions with Materials and Atoms* **2013,** *317*, 159-164.

76. Dutta, N.; Buzarbaruah, N.; Mohanty, S., Damage studies on tungsten due to helium ion irradiation. *Journal of Nuclear Materials* **2014,** *452* (1-3), 51-56.

77. Tyburska-Püschel, B.; Ertl, K.; Mayer, M.; Rapp, J.; Kleyn, A.; van Emmichoven, P. Z., Saturation of deuterium retention in self-damaged tungsten exposed to high-flux plasmas. *Nuclear Fusion* **2012,** *52* (2), 023008.

78. Alimov, V. K.; Hatano, Y.; Tyburska-Püschel, B.; Sugiyama, K.; Takagi, I.; Furuta, Y.; Dorner, J.; Fußeder, M.; Isobe, K.; Yamanishi, T., Deuterium retention in tungsten damaged with W ions to various damage levels. *Journal of Nuclear Materials* **2013,** *441* (1-3), 280-285.

79. Abernethy, R., Predicting the performance of tungsten in a fusion environment: a literature review. *Materials Science and Technology* **2017,** *33* (4), 388-399.

80. Jensen, C.; Chirtoc, M.; Horny, N.; Antoniow, J.; Pron, H.; Ban, H., Thermal conductivity profile determination in proton-irradiated ZrC by spatial and frequency scanning thermal wave methods. *Journal of Applied Physics* **2013,** *114* (13), 133509.

81. Tynan, G. R.; Doerner, R. P.; Barton, J.; Chen, R.; Cui, S.; Simmonds, M.; Wang, Y.; Weaver, J.; Mara, N.; Pathak, S., Deuterium retention and thermal conductivity in ion-beam displacement-damaged tungsten. *Nuclear Materials and Energy* **2017,** *12*, 164-168.

82. Bolt, H.; Barabash, V.; Federici, G.; Linke, J.; Loarte, A.; Roth, J.; Sato, K., Plasma facing and high heat flux materials–needs for ITER and beyond. *Journal of Nuclear Materials* **2002,** *307*, 43-52.

83. Ogorodnikova, O.; Gasparyan, Y.; Efimov, V.; Grzonka, J., Annealing of radiation-induced damage in tungsten under and after irradiation with 20 MeV self-ions. *Journal of Nuclear Materials* **2014,** *451* (1-3), 379-386.

84. Markina, E.; Mayer, M.; Manhard, A.; Schwarz-Selinger, T., Recovery temperatures of defects in tungsten created by self-implantation. *Journal of Nuclear Materials* **2015,** *463*, 329-332.

85. Simmonds, M.; Wang, Y.; Barton, J.; Baldwin, M.; Yu, J.; Doerner, R.; Tynan, G., Reduced deuterium retention in simultaneously damaged and annealed tungsten. *Journal of Nuclear Materials* **2017,** *494*, 67-71.

86. Stoller, R. E.; Toloczko, M. B.; Was, G. S.; Certain, A. G.; Dwaraknath, S.; Garner, F. A., On the use of SRIM for computing radiation damage exposure. *Nuclear instruments and methods in physics research section B: beam interactions with materials and atoms* **2013,** *310*, 75-80.

87. Simonen, E.; Ghoniem, N.; Packan, N., Pulsed flux effects on radiation damage. *Journal of Nuclear Materials* **1984,** *122* (1-3), 391-401.

88. ASTM E521-16. Standard practice for investigating the effects of neutron raidation damage using charged-particle irradiation. *West Conshohocken (PA): ASTM International* **2016**.

89. Zinkle, S.; Snead, L., Opportunities and limitations for ion beams in radiation effects studies: Bridging critical gaps between charged particle and neutron irradiations. *Scripta Materialia* **2018,** *143*, 154-160.

90. Lee, E.; Packan, N.; Mansur, L., Effects of pulsed dual-ion irradiation on phase transformations and microstructure in Ti-modified austenitic alloy. *Journal of Nuclear Materials* **1983,** *117*, 123-133.

91. Trinkaus, H.; Ullmaier, H., Conditions for effects of radiation pulsing. *Journal of nuclear materials* **2002,** *307*, 1705-1709.

92. Cui, S.; Simmonds, M.; Qin, W.; Ren, F.; Tynan, G. R.; Doerner, R. P.; Chen, R., Thermal conductivity reduction of tungsten plasma facing material due to helium plasma irradiation in PISCES using the improved 3-omega method. *Journal of Nuclear Materials* **2017,** *486*, 267-273.

93. Thedsakhulwong, A.; Thowladda, W., Removal of carbon contamination on silicon wafer surfaces by microwave oxygen plasma. *Journal of Metals, Materials and Minerals* **2008,** *18* (2), 137-141.

94. Feser, J. P., *Scalable routes to efficient thermoelectric materials*. University of California, Berkeley: 2010.

95. Borca-Tasciuc, T.; Kumar, A.; Chen, G., Data reduction in 3ω method for thin-film thermal conductivity determination. *Review of scientific instruments* **2001,** *72* (4), 2139-2147.

96. Powell, R.; Ho, C. Y.; Liley, P. E., Thermal conductivity of selected materials. **1966**.

97. Kwon, S.; Zheng, J.; Wingert, M. C.; Cui, S.; Chen, R., Unusually high and anisotropic thermal conductivity in amorphous silicon nanostructures. *ACS nano* **2017,** *11* (3), 2470-2476.

98. Cappella, A.; Battaglia, J. L.; Schick, V.; Kusiak, A.; Lamperti, A.; Wiemer, C.; Hay, B., High temperature thermal conductivity of amorphous Al2O3 thin films grown by low temperature ALD. *Advanced Engineering Materials* **2013,** *15* (11), 1046-1050.

99. El-Atwani, O.; Esquivel, E.; Efe, M.; Aydogan, E.; Wang, Y.; Martinez, E.; Maloy, S., Loop and void damage during heavy ion irradiation on nanocrystalline and coarse grained tungsten: Microstructure, effect of dpa rate, temperature, and grain size. *Acta Materialia* **2018**.

100. Oh, D.-W.; Ravichandran, J.; Liang, C.-W.; Siemons, W.; Jalan, B.; Brooks, C. M.; Huijben, M.; Schlom, D. G.; Stemmer, S.; Martin, L. W., Thermal conductivity as a metric for the crystalline quality of SrTiO 3 epitaxial layers. *Applied physics letters* **2011,** *98* (22), 221904.

101. Scullin, M. L.; Ravichandran, J.; Yu, C.; Huijben, M.; Seidel, J.; Majumdar, A.; Ramesh, R., Pulsed laser deposition-induced reduction of SrTiO3 crystals. *Acta materialia* **2010,** *58* (2), 457-463.

102. Watanabe, H.; Futagami, N.; Naitou, S.; Yoshida, N., Microstructure and thermal desorption of deuterium in heavy-ion-irradiated pure tungsten. *Journal of Nuclear Materials* **2014,** *455* (1-3), 51-55.

103. t Hoen, M.; Tyburska-Pueschel, B.; Ertl, K.; Mayer, M.; Rapp, J.; Kleyn, A.; Zeijlmans van Emmichoven, P., Saturation of deuterium retention in self-damaged tungsten exposed to high-flux plasmas. *Nuclear Fusion* **2012,** *52*.

104. Zhang, Z.; Yabuuchi, K.; Kimura, A., Defect distribution in ion-irradiated pure tungsten at different temperatures. *Journal of Nuclear Materials* **2016,** *480*, 207-215.

105. Mason, D.; Yi, X.; Kirk, M.; Dudarev, S., Elastic trapping of dislocation loops in cascades in ion-irradiated tungsten foils. *Journal of Physics: Condensed Matter* **2014,** *26* (37), 375701.

106. El-Atwani, O.; Suslova, A.; Novakowski, T.; Hattar, K.; Efe, M.; Harilal, S.; Hassanein, A., In-situ TEM/heavy ion irradiation on ultrafine-and nanocrystalline-grained tungsten: Effect of 3MeV Si, Cu and W ions. *Materials Characterization* **2015,** *99*, 68-76.

107. Barton, J.; Wang, Y.; Dittmar, T.; Doerner, R.; Tynan, G., Deuterium retention in tungsten after heavy ion damage and hydrogen isotope exchange in PISCES. *Nuclear Instruments and Methods in Physics Research Section B: Beam Interactions with Materials and Atoms* **2014,** *332*, 275-279.

108. Hu, L.; Wirth, B. D.; Maroudas, D., Thermal conductivity of tungsten: Effects of plasma-related structural defects from molecular-dynamics simulations. *Applied Physics Letters* **2017,** *111* (8), 081902.

109. Amino, T.; Arakawa, K.; Mori, H., Activation energy for long-range migration of self-interstitial atoms in tungsten obtained by direct measurement of radiation-induced point-defect clusters. *Philosophical Magazine Letters* **2011,** *91* (2), 86-96.

110. Kittel, C.; McEuen, P.; McEuen, P., *Introduction to solid state physics*. Wiley New York: 1996; Vol. 8.

111. Maisonnier, D.; Campbell, D.; Cook, I.; Di Pace, L.; Giancarli, L.; Hayward, J.; Puma, A. L.; Medrano, M.; Norajitra, P.; Roccella, M., Power plant conceptual studies in Europe. *Nuclear Fusion* **2007,** *47* (11), 1524.

112. Asakura, N.; Shimizu, K.; Hoshino, K.; Tobita, K.; Tokunaga, S.; Takizuka, T., A simulation study of large power handling in the divertor for a Demo reactor. *Nuclear Fusion* **2013,** *53* (12), 123013.

113. Behrisch, R.; Scherzer, B., He wall bombardment and wall erosion in fusion devices. *Radiation Effects* **1983,** *78* (1-4), 393-403.

114. Tanabe, T., High-Z candidate plasma facing materials. *J. Nucl. Fusion* **1994,** *5*, 129-148.

115. Iwakiri, H.; Yasunaga, K.; Morishita, K.; Yoshida, N., Microstructure evolution in tungsten during low-energy helium ion irradiation. *Journal of nuclear materials* **2000,** *283*, 1134-1138.

116. Takamura, S.; Ohno, N.; Nishijima, D.; Kajita, S., Formation of nanostructured tungsten with arborescent shape due to helium plasma irradiation. *Plasma and fusion research* **2006,** *1*, 051-051.

117. Baldwin, M.; Doerner, R., Helium induced nanoscopic morphology on tungsten under fusion relevant plasma conditions. *Nuclear Fusion* **2008,** *48* (3), 035001.

118. Kajita, S.; Sakaguchi, W.; Ohno, N.; Yoshida, N.; Saeki, T., Formation process of tungsten nanostructure by the exposure to helium plasma under fusion relevant plasma conditions. *Nuclear Fusion* **2009,** *49* (9), 095005.

119. Ye, M.; Takamura, S.; Ohno, N., Study of hot tungsten emissive plate in high heat flux plasma on NAGDIS-I. *Journal of nuclear materials* **1997,** *241*, 1243-1247.

120. Nishijima, D.; Ye, M.; Ohno, N.; Takamura, S., Incident ion energy dependence of bubble formation on tungsten surface with low energy and high flux helium plasma irradiation. *Journal of nuclear materials* **2003,** *313*, 97-101.

121. Ye, M.; Kanehara, H.; Fukuta, S.; Ohno, N.; Takamura, S., Blister formation on tungsten surface under low energy and high flux hydrogen plasma irradiation in NAGDIS-I. *Journal of nuclear materials* **2003,** *313*, 72-76.

122. De Temmerman, G.; Bystrov, K.; Doerner, R.; Marot, L.; Wright, G.; Woller, K.; Whyte, D.; Zielinski, J., Helium effects on tungsten under fusion-relevant plasma loading conditions. *Journal of Nuclear Materials* **2013,** *438*, S78-S83.

123. Parish, C. M.; Hijazi, H.; Meyer, H.; Meyer, F. W., Effect of tungsten crystallographic orientation on He-ion-induced surface morphology changes. *Acta Materialia* **2014,** *62*, 173-181.

124. Efe, M.; El-Atwani, O.; Guo, Y.; Klenosky, D. R., Microstructure refinement of tungsten by surface deformation for irradiation damage resistance. *Scripta Materialia* **2014,** *70*, 31-34.

125. Sakaguchi, W.; Kajita, S.; Ohno, N.; Takagi, M., In situ reflectivity of tungsten mirrors under helium plasma exposure. *Journal of Nuclear Materials* **2009,** *390*, 1149-1152.

126. Kajita, S.; Takamura, S.; Ohno, N.; Nishijima, D.; Iwakiri, H.; Yoshida, N., Sub-ms laser pulse irradiation on tungsten target damaged by exposure to helium plasma. *Nuclear Fusion* **2007,** *47* (9), 1358.

127. Federici, G.; Loarte, A.; Strohmayer, G., Assessment of erosion of the ITER divertor targets during type I ELMs. *Plasma physics and controlled fusion* **2003,** *45* (9), 1523.

128. Dulac, J.; LaFrance, M.; Trudeau, N.; Yamada, H., Transition to Sustainable Buildings: Strategies and Oppourtunities to 2050. *International Energy Agency* **2013**.

129. Goebel, D.; Hirooka, Y.; Conn, R.; Leung, W.; Campbell, G.; Bohdansky, J.; Wilson, K.; Bauer, W.; Causey, R.; Pontau, A., Erosion and redeposition experiments in the pisces facility. *Journal of Nuclear Materials* **1987,** *145*, 61-70.

130. Choi, D.; Wang, B.; Chung, S.; Liu, X.; Darbal, A.; Wise, A.; Nuhfer, N. T.; Barmak, K.; Warren, A. P.; Coffey, K. R., Phase, grain structure, stress, and resistivity of sputter-deposited tungsten films. *Journal of Vacuum Science & Technology A* **2011,** *29* (5), 051512.

131. Taylor, K. J.; Yun, S.; Tynan, G. R., Control of plasma parameters by using noble gas admixtures. *Journal of Vacuum Science & Technology A* **2004,** *22* (5), 2131-2138.

132. Kajita, S.; Yoshida, N.; Yoshihara, R.; Ohno, N.; Yamagiwa, M., TEM observation of the growth process of helium nanobubbles on tungsten: Nanostructure formation mechanism. *Journal of Nuclear Materials* **2011,** *418* (1), 152-158.

133. Rossnagel, S.; Noyan, I.; Cabral Jr, C., Phase transformation of thin sputter-deposited tungsten films at room temperature. *Journal of Vacuum Science & Technology B* **2002,** *20* (5), 2047-2051.

134. van der PAUYV, L., A method of measuring specific resistivity and Hall effect of discs of arbitrary shape. *Philips Res. Rep.* **1958,** *13*, 1-9.

135. Pauw, L. J. v. d., A method of measuring the resistivity and hall coefficient on lamellae of arbitrary shape. *Philips Res. Rep.* **1959,** *20*.

136. Fu, B.; Lai, W.; Yuan, Y.; Xu, H.; Liu, W., Calculation and analysis of lattice thermal conductivity in tungsten by molecular dynamics. *Journal of Nuclear Materials* **2012,** *427* (1), 268-273.

137. Franz, R.; Wiedemann, G., Ueber die Wärme‐Leitungsfähigkeit der Metalle. *Annalen der Physik* **1853,** *165* (8), 497-531.

138. Powell, R.; Ho, C. Y.; Liley, P. E. *Thermal conductivity of selected materials*; DTIC Document: 1966.

139. Wang, J.; Zhai, Z. J.; Jing, Y.; Zhang, C., Particle swarm optimization for redundant building cooling heating and power system. *Applied Energy* **2010,** *87* (12), 3668-3679.

140. Schachschal, S.; Adler, H.-J.; Pich, A.; Wetzel, S.; Matura, A.; van Pee, K.-H., Encapsulation of enzymes in microgels by polymerization/cross-linking in aqueous droplets. *Colloid and Polymer Science* **2011,** *289* (5-6), 693-698.

141. Sadineni, S. B.; Madala, S.; Boehm, R. F., Passive building energy savings: A review of building envelope components. *Renewable and Sustainable Energy Reviews* **2011,** *15* (8), 3617-3631.

142. Eicker, U., Cooling strategies, summer comfort and energy performance of a rehabilitated passive standard office building. *Applied Energy* **2010,** *87* (6), 2031-2039.

143. Chowdhury, A. A.; Rasul, M.; Khan, M. M. K., Thermal-comfort analysis and simulation for various low-energy cooling-technologies applied to an office building in a subtropical climate. *Applied Energy* **2008,** *85* (6), 449-462.

144. Zhou, D.; Zhao, C.-Y.; Tian, Y., Review on thermal energy storage with phase change materials (PCMs) in building applications. *Applied energy* **2012,** *92*, 593-605.

145. Soares, N.; Costa, J.; Gaspar, A.; Santos, P., Review of passive PCM latent heat thermal energy storage systems towards buildings' energy efficiency. *Energy and buildings* **2013,** *59*, 82-103.

146. Kuznik, F.; Virgone, J., Experimental assessment of a phase change material for wall building use. *Applied Energy* **2009,** *86* (10), 2038-2046.

147. Liu, K.; Jiang, L., Bio-inspired design of multiscale structures for function integration. *Nano Today* **2011,** *6* (2), 155-175.

148. Singh, A. V.; Rahman, A.; Kumar, N. S.; Aditi, A.; Galluzzi, M.; Bovio, S.; Barozzi, S.; Montani, E.; Parazzoli, D., Bio-inspired approaches to design smart fabrics. *Materials & Design* **2012,** *36*, 829-839.

149. Someya, T.; Sekitani, T.; Iba, S.; Kato, Y.; Kawaguchi, H.; Sakurai, T., A large-area, flexible pressure sensor matrix with organic field-effect transistors for artificial skin applications. *Proceedings of the National Academy of Sciences of the United States of America* **2004,** *101* (27), 9966-9970.

150. Takei, K.; Takahashi, T.; Ho, J. C.; Ko, H.; Gillies, A. G.; Leu, P. W.; Fearing, R. S.; Javey, A., Nanowire active-matrix circuitry for low-voltage macroscale artificial skin. *Nature materials* **2010,** *9* (10), 821-826.

151. Boucard, N.; Viton, C.; Agay, D.; Mari, E.; Roger, T.; Chancerelle, Y.; Domard, A., The use of physical hydrogels of chitosan for skin regeneration following third-degree burns. *Biomaterials* **2007,** *28* (24), 3478-3488.

152. Gong, J. P.; Katsuyama, Y.; Kurokawa, T.; Osada, Y., Double‐Network Hydrogels with Extremely High Mechanical Strength. *Advanced Materials* **2003,** *15* (14), 1155-1158.

153. Tanaka, Y.; Gong, J. P.; Osada, Y., Novel hydrogels with excellent mechanical performance. *Progress in Polymer Science* **2005,** *30* (1), 1-9.

154. Rotzetter, A.; Schumacher, C.; Bubenhofer, S.; Grass, R.; Gerber, L.; Zeltner, M.; Stark, W., Thermoresponsive polymer induced sweating surfaces as an efficient way to passively cool buildings. *Advanced materials* **2012,** *24* (39), 5352-5356.

155. Takegami, Y.; Yokoyama, Y.; Norisugi, O.; Nagatsuma, M.; Takata, K.; Rehman, M. U.; Matsunaga, K.; Yokoi, H.; Fujiki, S.; Makino, T., Synthesis and characterization of high‐quality skin‐cooling sheets containing thermosensitive poly (N‐isopropylacrylamid). *Journal of Biomedical Materials Research Part B: Applied Biomaterials* **2011,** *98* (1), 110-113.

156. Ziemba, R., The role of hydrogel dressings in prophylactic sets used by soldiers involved in polish military contingents. *burns* **2013,** *1*, 2.

157. Huang, Z.; Zhang, X.; Zhou, M.; Xu, X.; Zhang, X.; Hu, X., Bio-inspired passive skin cooling for handheld microelectronics devices. *Journal of Electronic Packaging* **2012,** *134* (1), 014501.

158. Cui, S.; Hu, Y.; Huang, Z.; Ma, C.; Yu, L.; Hu, X., Cooling performance of bio-mimic perspiration by temperature-sensitive hydrogel. *International Journal of Thermal Sciences* **2014,** *79*, 276-282.

159. Hu, Y.; Zhang, X.; Cui, S.; Ren, W.; Yu, L.; Hu, X., Bio-mimic transpiration cooling using temperature-sensitive hydrogel *Journal of Chemical Industry and Engineering* **2012,** *63* (7), 2025-2032.

160. Zhang, S.; Zhao, R.; Liu, J.; Gu, J., Investigation on a hydrogel based passive thermal management system for lithium ion batteries. *Energy* **2014,** *68*, 854-861.

161. Zhao, R.; Zhang, S.; Gu, J.; Liu, J.; Carkner, S.; Lanoue, E., An experimental study of lithium ion battery thermal management using flexible hydrogel films. *Journal of Power Sources* **2014,** *255*, 29-36.

162. Rotzetter, A.; Schumacher, C.; Bubenhofer, S.; Grass, R.; Gerber, L.; Zeltner, M.; Stark, W. J., Thermoresponsive polymer induced sweating surfaces as an efficient way to passively cool buildings. *Advanced materials* **2012,** *24* (39), 5352-5356.

163. Lake, G.; Thomas, A. In *The strength of highly elastic materials*, Proceedings of the Royal Society of London A: Mathematical, Physical and Engineering Sciences, The Royal Society: 1967; pp 108-119.

164. Qin, Z.; Pugno, N. M.; Buehler, M. J., Mechanics of fragmentation of crocodile skin and other thin films. *Scientific reports* **2014,** *4*.

165. Gijsman, P.; Meijers, G.; Vitarelli, G., Comparison of the UV-degradation chemistry of polypropylene, polyethylene, polyamide 6 and polybutylene terephthalate. *Polymer Degradation and Stability* **1999,** *65* (3), 433-441.

166. Feldman, D., Polymer weathering: photo-oxidation. *Journal of Polymers and the Environment* **2002,** *10* (4), 163-173.

167. Chambon, S.; Rivaton, A.; Gardette, J. L.; Firon, M.; Lutsen, L., Aging of a donor conjugated polymer: Photochemical studies of the degradation of poly [2‐methoxy‐5‐(3′, 7′‐dimethyloctyloxy)‐1, 4‐phenylenevinylene]. *Journal of Polymer Science Part A: Polymer Chemistry* **2007,** *45* (2), 317-331.

168. Gong, J. P., Why are double network hydrogels so tough? *Soft Matter* **2010,** *6* (12), 2583-2590.

169. Gong, J. P., Materials both tough and soft. *Science* **2014,** *344* (6180), 161-162.

170. Sun, J.-Y.; Zhao, X.; Illeperuma, W. R.; Chaudhuri, O.; Oh, K. H.; Mooney, D. J.; Vlassak, J. J.; Suo, Z., Highly stretchable and tough hydrogels. *Nature* **2012,** *489* (7414), 133.

171. Yang, W.; Sherman, V. R.; Gludovatz, B.; Schaible, E.; Stewart, P.; Ritchie, R. O.; Meyers, M. A., On the tear resistance of skin. *Nature communications* **2015,** *6*.

172. Qin, Z.; Pugno, N. M.; Buehler, M. J., Mechanics of fragmentation of crocodile skin and other thin films. *Scientific reports* **2014,** *4*, 4966.

173. Fiumefreddo, A.; Utz, M., Bulk streaming potential in poly (acrylic acid)/poly (acrylamide) hydrogels. *Macromolecules* **2010,** *43* (13), 5814-5819.

174. Yanfeng, C.; Min, Y., Swelling kinetics and stimuli-responsiveness of poly (DMAEMA) hydrogels prepared by UV-irradiation. *Radiation Physics and Chemistry* **2001,** *61* (1), 65-68.

175. Kim, S. J.; Park, S. J.; Kim, S. I., Swelling behavior of interpenetrating polymer network hydrogels composed of poly (vinyl alcohol) and chitosan. *Reactive and Functional Polymers* **2003,** *55* (1), 53-59.

176. Duran, S.; Şolpan, D.; Güven, O., Synthesis and characterization of acrylamide–acrylic acid hydrogels and adsorption of some textile dyes. *Nuclear Instruments and*

Methods in Physics Research Section B: Beam Interactions with Materials and Atoms **1999,** *151* (1-4), 196-199.

177. Gupta, N. V.; Shivakumar, H., Investigation of Swelling Behavior and Mechanical Properties of a pH-Sensitive Superporous Hydrogel Composite. *Iranian journal of pharmaceutical research: IJPR* **2012,** *11* (2), 481.

178. Xia, L.-W.; Xie, R.; Ju, X.-J.; Wang, W.; Chen, Q.; Chu, L.-Y., Nano-structured smart hydrogels with rapid response and high elasticity. *Nature communications* **2013,** *4*.

179. Berdahl, P.; Bretz, S. E., Preliminary survey of the solar reflectance of cool roofing materials. *Energy and Buildings* **1997,** *25* (2), 149-158.

180. Martin, M.; Berdahl, P., Summary of results from the spectral and angular sky radiation measurement program. *Solar Energy* **1984,** *33* (3), 241-252.

181. Kreith, F.; Manglik, R.; Bohn, M., *Principles of heat transfer*. Cengage learning: 2010.

182. Kosny, J.; Shukla, N.; Fallahi, A., Cost Analysis of Simple Phase Change Material-Enhanced Building Envelopes in Southern US Climates. *US Department of Energy* **2013**.

183. Aktacir, M. A.; Büyükalaca, O.; Yılmaz, T., A case study for influence of building thermal insulation on cooling load and air-conditioning system in the hot and humid regions. *Applied Energy* **2010,** *87* (2), 599-607.

184. Levinson, R.; Akbari, H.; Reilly, J. C., Cooler tile-roofed buildings with near-infrared-reflective non-white coatings. *Building and Environment* **2007,** *42* (7), 2591-2605.

185. Ahmed, E. M., Hydrogel: preparation, characterization, and applications. *Journal of advanced research* **2013**.

186. Özkan, L.; Kothare, M. V.; Georgakis, C., Control of a solution copolymerization reactor using multi-model predictive control. *Chemical Engineering Science* **2003,** *58* (7), 1207-1221.

187. Park, M.-J.; Hur, S.-M.; Rhee, H.-K., Online estimation and control of polymer quality in a copolymerization reactor. *AIChE journal* **2002,** *48* (5), 1013-1021.

188. Alaei, J.; Boroojerdi, S. H.; Rabiei, Z., Application of hydrogels in drying operation. *Petroleum & Coal* **2005,** *47* (3), 32-37.

189. Gaffin, S.; Rosenzweig, C.; Parshall, L.; Beattie, D.; Berghage, R.; O'Keeffe, G.; Braman, D., Energy balance modeling applied to a comparison of white and green roof cooling efficiency. *Green Roofs in the New York Metropolitan Region Research Report* **2010**, 7.

190. Hildebrandt, E. W.; Bos, W.; Moore, R., Assessing the impacts of white roofs on building energy loads. *ASHRAE transactions* **1998,** *104*, 810.

191. Wang, M.; Gao, Y.; Cao, C.; Chen, K.; Wen, Y.; Fang, D.; Li, L.; Guo, X., Binary Solvent Colloids of Thermosensitive Poly (N-isopropylacrylamide) Microgel for Smart Windows. *Industrial & Engineering Chemistry Research* **2014,** *53* (48), 18462-18472.

192. Nagaya, K.; Li, Y.; Jin, Z.; Fukumuro, M.; Ando, Y.; Akaishi, A., Low-temperature desiccant-based food drying system with airflow and temperature control. *Journal of food engineering* **2006,** *75* (1), 71-77.

193. Thomann, F. S.; Hall, M. R.; Mokaya, R.; Stevens, L. A., Hygrothermal simulation-informed design of mesoporous desiccants for optimised energy efficiency of mixed mode air conditioning systems. *Journal of Materials Chemistry A* **2015,** *3* (33), 17290-17303.

194. Kim, H.; Yang, S.; Rao, S. R.; Narayanan, S.; Kapustin, E. A.; Furukawa, H.; Umans, A. S.; Yaghi, O. M.; Wang, E. N., Water harvesting from air with metal-organic frameworks powered by natural sunlight. *Science* **2017,** *356* (6336), 430-434.

195. Kim, H.; Rao, S. R.; Kapustin, E. A.; Zhao, L.; Yang, S.; Yaghi, O. M.; Wang, E. N., Adsorption-based atmospheric water harvesting device for arid climates. *Nature communications* **2018,** *9* (1), 1191.

196. Kalmutzki, M. J.; Diercks, C. S.; Yaghi, O. M., Metal–Organic Frameworks for Water Harvesting from Air. *Advanced Materials* **2018**, 1704304.

197. Gandhidasan, P.; Al-Farayedhi, A. A.; Al-Mubarak, A. A., Dehydration of natural gas using solid desiccants. *Energy* **2001,** *26* (9), 855-868.

198. Heym, F.; Haber, J.; Korth, W.; Etzold, B. J.; Jess, A., Vapor pressure of water in mixtures with hydrophilic ionic liquids–a contribution to the design of processes for drying of gases by absorption in ionic liquids. *Chemical Engineering & Technology* **2010,** *33* (10), 1625-1634.

199. Bouzenada, S.; Kaabi, A.; Frainkin, L.; Salmon, T.; Léonard, A., Experimental comparative study on lithium chloride and calcium chloride desiccants. *Procedia Computer Science* **2016,** *83*, 718-725.

200. Rafique, M. M.; Gandhidasan, P.; Bahaidarah, H. M., Liquid desiccant materials and dehumidifiers–A review. *Renewable and Sustainable Energy Reviews* **2016,** *56*, 179-195.

201. Sultan, M.; El-Sharkawy, I. I.; Miyazaki, T.; Saha, B. B.; Koyama, S., An overview of solid desiccant dehumidification and air conditioning systems. *Renewable and Sustainable Energy Reviews* **2015,** *46*, 16-29.

202. Srivastava, N.; Eames, I., A review of adsorbents and adsorbates in solid–vapour adsorption heat pump systems. *Applied thermal engineering* **1998,** *18* (9), 707-714.

203. Gurgel, J. M.; Filho, L.; Couto, P. P. S., Apparent diffusivity of water in silica gel and NaX zeolite pellets. *HIGH TEMPERATURES HIGH PRESSURES* **2001,** *33* (4), 435-440.

204. Gordeeva, L.; Aristov, Y. I., Composites 'salt inside porous matrix'for adsorption heat transformation: a current state-of-the-art and new trends. *International Journal of Low-Carbon Technologies* **2012,** *7* (4), 288-302.

205. Casey, S. P.; Elvins, J.; Riffat, S.; Robinson, A., Salt impregnated desiccant matrices for 'open'thermochemical energy storage—Selection, synthesis and characterisation of candidate materials. *Energy and buildings* **2014,** *84*, 412-425.

206. Gordeeva, L.; Grekova, A.; Krieger, T.; Aristov, Y., Composites "binary salts in porous matrix" for adsorption heat transformation. *Applied Thermal Engineering* **2013,** *50* (2), 1633-1638.

207. Bourikas, K.; Kordulis, C.; Lycourghiotis, A., The Role of the Liquid‐Solid Interface in the Preparation of Supported Catalysts. *Catalysis Reviews* **2006,** *48* (4), 363-444.

208. Gong, L.; Wang, R.; Xia, Z.; Chen, C., Adsorption equilibrium of water on a composite adsorbent employing lithium chloride in silica gel. *Journal of Chemical & Engineering Data* **2010,** *55* (8), 2920-2923.

209. Mrowiec-Białoń, J.; Jarzebski, A. B.; Lachowski, A. I.; Malinowski, J. J.; Aristov, Y. I., Effective inorganic hybrid adsorbents of water vapor by the sol− gel method. *Chemistry of materials* **1997,** *9* (11), 2486-2490.

210. Cui, S.; Ahn, C.; Wingert, M. C.; Leung, D.; Cai, S.; Chen, R., Bio-inspired effective and regenerable building cooling using tough hydrogels. *Applied Energy* **2016,** *168*, 332-339.

211. Laftah, W. A.; Hashim, S.; Ibrahim, A. N., Polymer hydrogels: A review. *Polymer-Plastics Technology and Engineering* **2011,** *50* (14), 1475-1486.

212. Xu, S.; Fan, L.; Zeng, M.; Wang, J.; Liu, Q., Swelling properties and kinetics of CaCl 2/polyacrylamide hygroscopic hybrid hydrogels. *Colloids and Surfaces A: Physicochemical and Engineering Aspects* **2010,** *371* (1), 59-63.

213. Yang, Y.; Rana, D.; Lan, C. Q., Development of solid super desiccants based on a polymeric superabsorbent hydrogel composite. *RSC Advances* **2015,** *5* (73), 59583-59590.

214. Johnson, I.; Choate, W. T.; Davidson, A. *Waste heat recovery. Technology and opportunities in US industry*; BCS, Inc., Laurel, MD (United States): 2008.

215. Ng, E.-P.; Mintova, S., Nanoporous materials with enhanced hydrophilicity and high water sorption capacity. *Microporous and Mesoporous Materials* **2008,** *114* (1), 1-26.

216. Perelman, L. A.; Moore, T.; Singelyn, J.; Sailor, M. J.; Segal, E., Preparation and Characterization of a pH‐and Thermally Responsive Poly (N‐isopropylacrylamide‐co‐acrylic acid)/Porous SiO2 Hybrid. *Advanced functional materials* **2010,** *20* (5), 826-833.

217. Zheng, W. J.; An, N.; Yang, J. H.; Zhou, J.; Chen, Y. M., Tough al-alginate/poly (n-isopropylacrylamide) hydrogel with tunable lcst for soft robotics. *ACS applied materials & interfaces* **2015,** *7* (3), 1758-1764.

218. Kim, J.; Cho, Y.; Kim, S.; Lee, J., 3D Cocontinuous Composites of Hydrophilic and Hydrophobic Soft Materials: High Modulus and Fast Actuation Time. *ACS Macro Letters* **2017,** *6* (10), 1119-1123.

219. Liu, J.; Li, Q.; Su, Y.; Yue, Q.; Gao, B., Characterization and swelling–deswelling properties of wheat straw cellulose based semi-IPNs hydrogel. *Carbohydrate polymers* **2014,** *107*, 232-240.

220. Zhang, X.; Sumathy, K.; Dai, Y.; Wang, R., Parametric study on the silica gel–calcium chloride composite desiccant rotary wheel employing fractal BET adsorption isotherm. *International journal of energy research* **2005,** *29* (1), 37-51.

221. Zhang, X.; Qiu, L., Moisture transport and adsorption on silica gel–calcium chloride composite adsorbents. *Energy Conversion and Management* **2007,** *48* (1), 320-326.

222. Lee, S.; Kim, H. J.; Chang, S. H.; Lee, J., Anisometric nanocomposite hydrogels with temperature responsive compartments. *Soft Matter* **2013,** *9* (2), 472-479.

223. Halake, K. S.; Lee, J., Superporous thermo-responsive hydrogels by combination of cellulose fibers and aligned micropores. *Carbohydrate polymers* **2014,** *105*, 184-192.

224. Sun, B.; Wang, Z.; He, Q.; Fan, W.; Cai, S., Porous double network gels with high toughness, high stretchability and fast solvent-absorption. *Soft matter* **2017,** *13* (38), 6852-6857.

225. Cevallos, O. R. Adsorption characteristics of water and silica gel system for desalination cycle. 2012.

226. Jia, C.; Dai, Y.; Wu, J.; Wang, R., Experimental comparison of two honeycombed desiccant wheels fabricated with silica gel and composite desiccant material. *Energy Conversion and Management* **2006,** *47* (15-16), 2523-2534.

227. Dawoud, B.; Aristov, Y., Experimental study on the kinetics of water vapor sorption on selective water sorbents, silica gel and alumina under typical operating conditions of sorption heat pumps. *International Journal of Heat and Mass Transfer* **2003,** *46* (2), 273-281.

228. Lee, J.; Lee, D.-Y., Sorption characteristics of a novel polymeric desiccant. *International journal of refrigeration* **2012,** *35* (7), 1940-1949.

229. Seo, Y. K.; Yoon, J. W.; Lee, J. S.; Hwang, Y. K.; Jun, C. H.; Chang, J. S.; Wuttke, S.; Bazin, P.; Vimont, A.; Daturi, M., Energy‐Efficient Dehumidification over Hierachically Porous Metal‐Organic Frameworks as Advanced Water Adsorbents. *Advanced Materials* **2012,** *24* (6), 806-810.

230. Camargo, J.; Godoy Jr, E.; Ebinuma, C., An evaporative and desiccant cooling system for air conditioning in humid climates. *Journal of the Brazilian society of mechanical sciences and engineering* **2005,** *27* (3), 243-247.

231. Farag, H. A.; Ezzat, M. M.; Amer, H.; Nashed, A. W., Natural gas dehydration by desiccant materials. *Alexandria Engineering Journal* **2011,** *50* (4), 431-439.

232. Comino, F.; de Adana, M. R.; Peci, F., Energy saving potential of a hybrid HVAC system with a desiccant wheel activated at low temperatures and an indirect evaporative cooler in handling air in buildings with high latent loads. *Applied Thermal Engineering* **2018,** *131*, 412-427.

233. Talaat, M.; Awad, M.; Zeidan, E.; Hamed, A., Solar-powered portable apparatus for extracting water from air using desiccant solution. *Renewable Energy* **2018,** *119*, 662-674.

234. Thompson, M., The damage and recovery of neutron irradiated tungsten. *Philosophical Magazine* **1960,** *5* (51), 278-296.

235. Zakharova, M.; Solov'ev, V.; Bykov, V., High-temperature stages of the annealing of radiation defects in refractory BCC metals. *Soviet Atomic Energy* **1975,** *38* (2), 101-104.

236. Jenkins, M. L.; Kirk, M. A., *Characterisation of radiation damage by transmission electron microscopy*. CRC Press: 2000.